Ringdown Spectroscopy in Optical Waveguides

by

NICHOLAS RONALD TREFIAK

A thesis submitted to the Department of Chemistry

in conformity with the requirements for

the degree of Master of Science

Queen's University

Kingston, Ontario, Canada

July, 2007

Copyright © Nicholas Ronald Trefiak, 2007

Abstract

Ringdown spectroscopy (RDS) is an absorption spectroscopic and detection technique that makes use of an optical cavity to realize a long effective pathlength through a sample and to render the measurement independent of intensity. These two features give RDS an advantage over traditional absorption techniques and allows its application in measuring concentrations of strongly absorbing analytes present in trace amounts, or in measuring weak absorptions for analytes in higher concentrations. The resonant optical cavities used here are created from optical fibre. This permits the easy construction of an inexpensive apparatus for RDS. The performance of various cavity geometries (linear, circular) in three ranges of the visible and near infrared spectrum (405, 800, and 1550 nm) was examined. Concurrent multiexponential decays arising from core modes, cladding modes, and amplified spontaneous emission were analyzed in the framework of an exponential decay model transformed into the frequency domain.

The small mode field diameter of light within a fibre is well suited to probing very small liquid volumes on the order of pico- or femtolitres. This uniquely positions optical waveguide-based RDS for application in absorption detection for separation techniques such as capillary electrophoresis (CE) and high performance liquid chromatography (HPLC) where high time resolution detection is required across narrow separation channels. The experimental and theoretical work presented here was preformed with an eye towards this purpose.

Acknowledgements

Special thanks and gratitude go to my thesis supervisor Dr. Hans-Peter Loock for his support and guidance during my course of study and for generously giving me the opportunity to participate in international conferences and collaborations. Your confidence, passion for science, and wealth of ideas gave me the motivation to keep going. Special thanks also to Dr. Jack Barnes for guidance in the lab and many useful discussions. Your knowledge and insight into almost every facet of chemistry and physics was of great help. Many thanks go to the individuals who gave assistance in performing some of the experiments presented here: Ian Adams, Richard Walford, Emily Gibb, Dan Courtney, Fiona Rask, Michael Gretton, and Sydney Dias. Thanks also to those who showed me my way around the lab: Theresa McCormick, Zhaoguo Tong, and Runkai Li. I would also like to thank all the other members of the Loock Laser Lab for their friendship and support: Scott Hopkins, Klaus Bescherer, Constantin Romanescu, Jun Zhang, and Albert Yang. Further gratitude to Albert and Scott is deserved for giving me a place to live while finishing this thesis. Finally, I wish to thank my parents who have given me nothing but love, guidance, support and confidence over my whole life.

Table of Contents

List of Tables

List of Figures

Chapter 1 Introduction

Electrophoresis provides a powerful means of separating complex chemical and biochemical mixtures, allowing the constituents to be identified and/or quantified. A recent trend is miniaturization and parallelization of the electrophoretic device, concurrent with integration of sample preparation and analyte detection apparatus, resulting in a so called lab-on-a-chip or micro-total-analysis system (μ-TAS). The benefits of this trend include reduction in sample volume, cost, and time, thereby accelerating the rate of research, discovery, and development. The predominant detection method in use on lab-on-a-chip devices is fluorescence sensing. While very sensitive, fluorescence sensing generally requires the analyte(s) to be tagged with a fluorescent dye. This labelling step can require both considerable time and effort and if not performed with care may result in errors being introduced in quantitative measurements. While not as sensitive, optical absorption detection is a general method applicable to almost all analytes and requires little or no sample preparation. The goal of this thesis is to refine and expand the scope of a general absorption sensor that may operate as an alternative to, or in conjunction with, fluorescence sensing in microfluidic applications. This work involves the design, characterization, and optimization of such a sensor.

The major challenge of developing such an absorption detector lies in probing the extremely small volumes encountered in lab-on-a-chip devices without compromising the resolution of the separation. An ideal candidate to meet this challenge is ringdown spectroscopy (RDS), where light is passed multiple times through the sample, resulting in

an effective pathlength tens or hundreds of times greater than the actual pathlength. This is accomplished by guiding the light in a "mirrored" cavity or loop of optical fibre, with the sample being introduced in the optical path by leaving a small gap in the cavity/loop. The fibre cavity/loop can be easily integrated into the lab-on-a-chip by means of microdrilled holes intersecting the microfluidic channels at right angles (Figure 1.1).

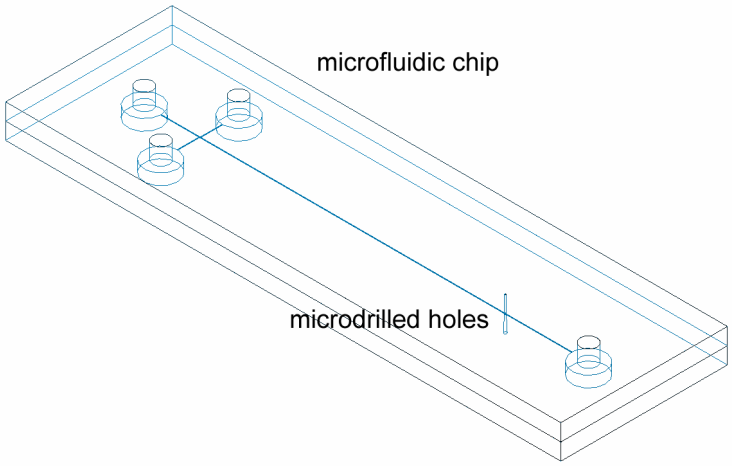

Figure 1.1: Microfluidic chip with microdrilled holes for integration with a fibre loop/cavity.

Ringdown sensing differs from conventional absorption sensing in that it measures not the absolute intensity of light passing through the sample, but the rate of intensity decay in the cavity/loop. This trait renders ringdown sensing independent of intensity fluctuations in the light source and detector. Upon rapidly switching off the light source the intensity in the cavity/loop decays exponentially to $1/e$ of its initial value at the characteristic time termed the ringdown time. The ringdown time can be determined in the time domain (TD) or the frequency domain (FD), and is inversely proportional to the absorption coefficient and concentration of the analyte(s), allowing for quantitative analysis.

This first chapter gives an introduction of absorption and ringdown spectroscopy, the characteristics and guiding properties of optical fibre, and a brief review of pertinent literature from the field of cavity ringdown spectroscopy. The second chapter provides a more in-depth look at the decay processes in a fibre cavity/loop and how they may be quantified both in the time and frequency domain. Reducing the optical loss in a ringdown system is of great importance for realizing the best sensitivity and detection limit – some methods towards achieving this are presenting in the third chapter. Chapters 4 to 7 present experimental results for ringdown systems constructed from both cavities and loops, using both single mode and multimode fibre, in three different wavelength ranges. Chapter 8 outlines methods for reducing the data acquisition time for calibration of the system in the frequency domain. The ninth chapter looks to the future of ringdown systems, suggesting improvements over the work presented here as well as novel apparatus and methods. Finally, Chapter 10 offers an overview of the preceding chapters and a summary of accomplishments.

1.1 Absorption spectroscopy

Conventional absorption spectroscopy measures the intensity of light transmitted through a sample, $I(d,\lambda)$, and compares it to the incident intensity, I_o. The light absorbed by the sample is thus

$$\Delta I = I_o - I\left(d,\lambda\right) \tag{1.1}$$

The transmitted light intensity is described by the Beer-Lambert law

$$I(d,\lambda) = I_o e^{-\varepsilon(\lambda)Cd} \qquad (1.2)$$

where $\varepsilon(\lambda)$ is the wavelength dependent absorption coefficient, C is the concentration of the absorbing species, and d is the path length through the sample.[1] Equation (1.1) demonstrates the fundamental limitation in the conventional means of performing absorption spectroscopy. For low concentrations, weak absorbers, or short path length, both I_o and $I(d,\lambda)$ are relatively large, so by taking the difference ΔI one is measuring a small intensity change on a large background. Thus conventional absorption measurements are highly dependent on the intensity stability of the light source and detector used, and for absolute absorptivity measurements need careful referencing against an empty sample cell.[2] We now contrast this with ringdown spectroscopy.

1.2 Ringdown sensing and spectroscopy

The main advantages of ringdown spectrometers and sensors are their multi-pass nature, which results in a long effective pathlength through the sample, and their insensitivity to fluctuations in the light source intensity, making measurement of absolute absorption coefficients and number densities possible.[3, 4] The technique has been reviewed several times in the past years,[2, 4-7] and only an overview will be presented here. A more detailed review of the literature pertaining to the application of CRD in absorption detection of liquids is given in Chapter 1.4.1.

In its original rendition, a gas-phase sample is placed into a high-finesse optical cavity that consists of two highly reflective confocal mirrors, aligned and situated roughly 1 m apart (Figure 1.2).[8] Many variations on this initial design have been reported including optical cavities that consist of three[9, 10] or four[11] mirrors, a folded monolithic resonator,[12] a fibre cavity or loop,[13, 14] and a microsphere resonator.[15] Light, usually from a laser, is coupled into the optical cavity through the back of one of the mirrors. This light will be reflected back and forth in the cavity (and through a sample) multiple times, with a small fraction of the light being lost each time it strikes one of the mirrors. A sensitive detector, usually a photomultiplier tube (PMT), is placed behind the mirror opposite the laser and measures the small amount of light transmitted from the cavity. After the light source is switched off, the detector records the decay of light intensity still present in the optical cavity due to the mirrors' high reflectivity. Here arises the aspect of ringdown sensing that makes it insensitive to intensity fluctuations: it measures the *rate* of intensity decay in the cavity, rather than the intensity itself. These advantages can result in lower detection limits and higher sensitivity than is achievable in conventional absorption sensing and spectroscopy.

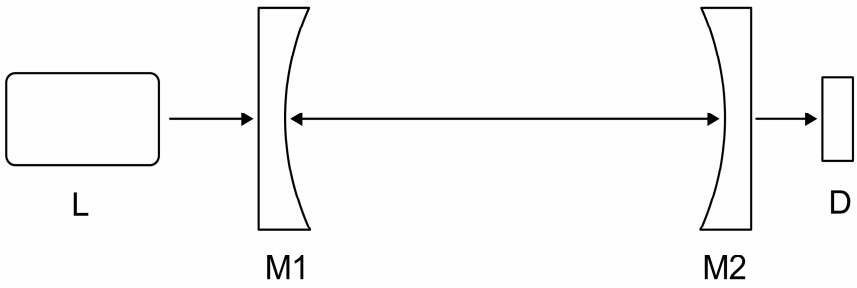

Figure 1.2: Schematic of a cavity ringdown apparatus.

Light from a laser (L) is coupled into the cavity through the rear of mirror M1, is reflected between M1 and M2, with a small fraction of light passing through M2 and reaching the detector (D).

The decay of intensity in the cavity generally follows an exponential trend with time, where the intensity (I) falls to $1/e$ of its initial value (I_o) at the characteristic time τ, termed the ringdown time. The expression relating the intensity to the characteristic time is referred to as the impulse response function, and may be written as

$$I(t) = I_o e^{-t/\tau} \tag{1.3}$$

This is the expression for a single exponential decay occurring in the optical cavity, which is not always the case. Multi-exponential decays will be discussed in detail later (Chapter 2) and for the discussion below a single exponential decay will be assumed.

The ringdown time of a cavity, such as the one shown in Figure 1.2, can be related to the round trip time t_r (the time for light to travel from one mirror to the other and back) and the sum of optical losses occurring in the cavity. The optical losses, Γ, can arise from the less than unity reflectivity of the mirrors, the absorption or scattering of light from any other optical components present in the cavity, and the absorption or scattering of light due to the sample. The ringdown time can thus be expressed as

$$\tau = \frac{t_r}{2\left(\Gamma_{mirrors} + \Gamma_{components} + \Gamma_{sample}\right)} \tag{1.4}$$

The round trip time may be written in terms of the length of the cavity L and the refractive index n of the cavity medium to read

$$t_r = \frac{2nL}{c_o} \tag{1.5}$$

(Note that for a fibre loop the round trip time is $t_r = nL/c_o$.) The loss of the mirrors is related to the reflectivity of the cavity R by $-\ln(R)$, which can be approximated as $1-R$ for $R \approx 1$. The loss due to components is included either as a length dependent term or an overall term. The loss of the sample is assumed to follow the Beer-Lambert law, as discussed above (Chapter 1.1). Equation (1.4) can now be rewritten in the more useful form

$$\tau = \frac{nL}{c_o\left(-\ln(R) + \Gamma_{components} + \varepsilon Cd\right)} \tag{1.6}$$

Thus the ringdown time can be directly related to the absorption coefficient or concentration of the sample. Note that the absorption coefficient in equation (1.6) is given with respect to base e whereas the absorption coefficient, ε', is typically quoted with respect to base 10 and $\varepsilon = \varepsilon' \ln 10$.

The multi-pass nature of ringdown spectrometers gives rise to an effective pathlength through the sample that is longer that the true pathlength since the light traverses the sample multiple times. The effective pathlength, d_{eff}, is defined as the product of the pathlength, d, and the number of times, N, the light passes through the

sample by the moment the ringdown time is reached. This effective absorption path depends on the cavity finesse and, when assuming that the mirror reflectivity losses are the most important loss process, it can be written in terms of the reflectivity as[4]

$$d_{eff} = \frac{d}{1-R} \tag{1.7}$$

Other quantities used to describe the cavity are the finesse and the Q-factor. The finesse, F, is related to the reflectivity by[2]

$$F = \frac{\pi\sqrt{R}}{1-R} \tag{1.8}$$

The Q-factor may be given in terms of the ringdown time as

$$Q = 2\pi\nu\tau \tag{1.9}$$

where ν is the optical frequency. The minimum detectable absorption loss (MDAL), α_{min}, is commonly given as a means to quantify instrument performance. It is defined as,[2]

$$\alpha_{\min} = \varepsilon C_{\min} = \frac{L\Delta\tau_{\min}}{cd\tau_0^2} \tag{1.10}$$

where $\Delta\tau_{\min}$ is the minimum detectable change in the ringdown time and τ_0 is the ringdown time of the empty cavity. We often state the MDAL as the product εC_{DL} where C_{DL} is concentration of the absorber at the detection limit, given as 3σ above the baseline.

In both CRDS and FLRDS consideration must be made regarding the fact that resonant longitudinal modes are present in the cavity. The resonant condition is met when an integer number of wavelengths matches the cavity length and constructive interference occurs. The cavity resonances will be spaced by a frequency, $\Delta\nu$, termed the free spectral range (FSR), expressed as

$$\Delta\nu = \frac{c_o}{2nL} \tag{1.11}$$

where c_o is the speed of light in vacuum, n is the refractive index of the cavity medium, and L is the cavity length. The linewidth of a resonance, $\Delta\nu_{1/2}$, is given by

$$\Delta\nu_{1/2} = \frac{\Delta\nu}{F} \tag{1.12}$$

(The Q-factor may also be written as $Q = \nu/\Delta\nu_{1/2}$.) The longitudinal mode spectrum for a 5 cm fibre cavity is shown in Figure 1.3.

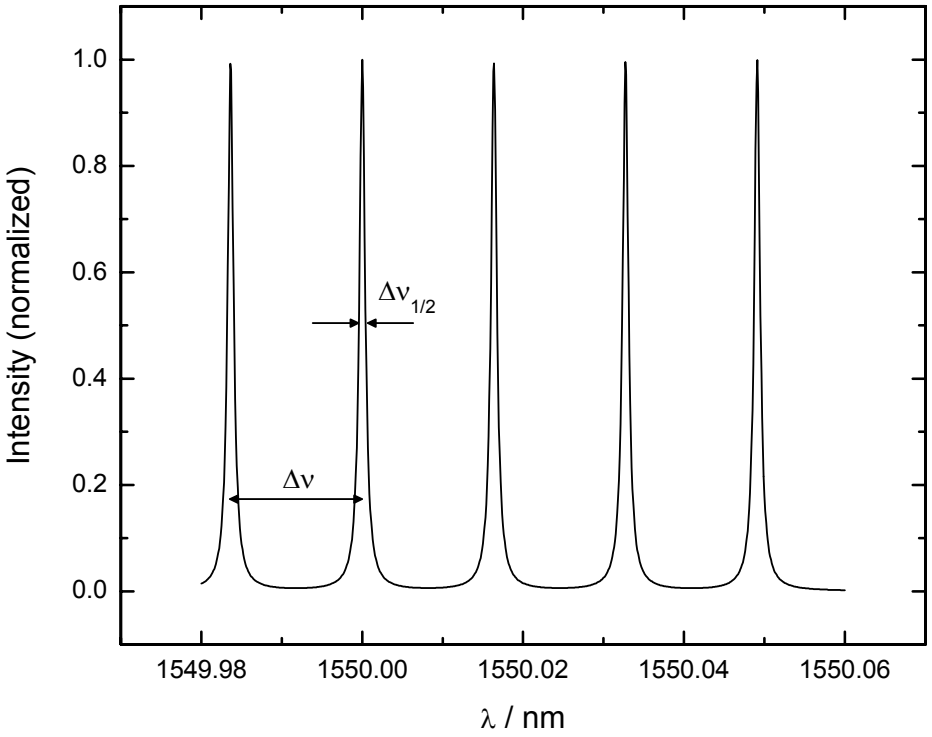

Figure 1.3: Longitudinal mode spectrum for a 5 cm fibre cavity with R = 0.85.

Here Δν = 16 pm and the linewidth is 0.8 pm.

If the laser is detuned from a resonant frequency, very little light will be coupled into the cavity since destructive interference from the superposition of incoming and reflected electromagnetic (EM) waves will take place.[16] Efficient coupling to the resonant modes is especially important when the cavity length is small and/or the cavity finesse is high.

In the experiments presented here, these concerns do not apply since for single mode fibres the cavities are both long and of relatively low finesse, and multimode fibres carry several hundred transverse modes that each have their own resonant frequency. This results in a pseudo-continuum of longitudinal modes being established in the cavity/loop due to a very small FSR and a large resonance linewidth, $\Delta\nu_{1/2}$. The laser linewidth is wider than the cavity FSR resulting in coupling to multiple longitudinal modes irrespective of wavelength. Hence, careful control of the cavity/loop length or the laser wavelength necessary in other experiments of this type is not required here.

1.3 Optical fibres

Standard optical fibre is composed of a silica core and cladding surrounded by a polymer coating. Light is guided in the core and cladding, while the coating adds strength and flexibility while protecting the silica from the outer environment. The fibre used in the following experiments is termed step index fibre since the refractive index profile of the fibre follows a step-like pattern. The refractive index of the core is slightly higher than that of the cladding (by < 1%) allowing the fibre to guide light (discussed below). Fibre is available with a wide variety of core and cladding diameters to suit different applications. Typical single-mode fibre (SMF) for telecom use has core/cladding diameters of 8.4/125 μm. Multi-mode fibre (MMF) has a larger core diameter, with typical dimensions being 100/140 μm.

Light propagating along a fibre can be described as a set of guided electromagnetic waves, termed modes. Core modes are guided in the core by total internal reflection occurring at the interface between the core and the cladding. The refractive indices, n_{co} and n_{cl}, of the core and cladding respectively, define the critical angle, ϕ_c, at and above which total internal reflection will occur. A ray incident on the interface with $\phi < \phi_c$ will be refracted into the cladding and may be guided in cladding modes or lost to the fibre coating or air. Rays that are coupled from free-space and guided by the fibre core must lie within what is called the acceptance cone of the fibre, the outer boundary of which is related to ϕ_c. This cone is usually described by the numerical aperture (NA) of the fibre

$$NA = n \sin \theta_c = n_{co} \sin\left(90° - \phi_c\right) = \sqrt{n_{co}^2 - n_{cl}^2} \tag{1.13}$$

where n is the refractive index of the medium outside the fibre and θ_c is the critical angle for light incident on the fibre face. Rays will emerge from a fibre with the same numerical aperture. These concepts are illustrated in Figure 1.4.

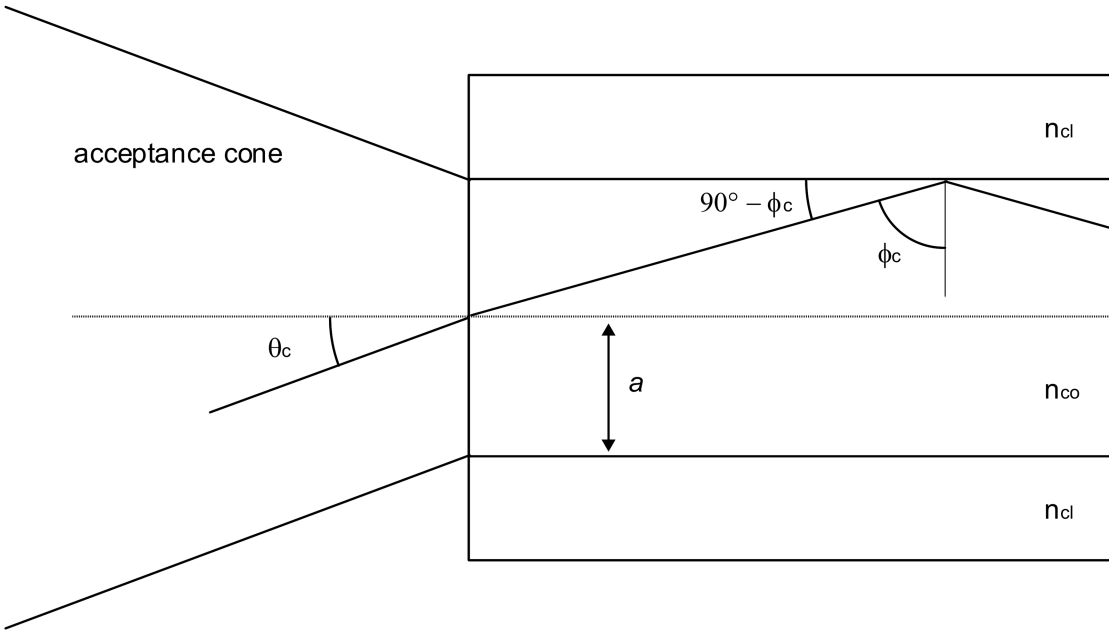

Figure 1.4: Illustration of light guided by total internal reflection in an optical fibre.

A ray incident on the fibre face at angle θ_c is refracted in the fibre core so that it is incident on the core/cladding interface at angle ϕ_c. The radius of the fibre is denoted *a*.

The exact solution of the set of guided modes in an optical fibre can be found by solving Maxwell's equations using cylindrical boundary conditions for the core/cladding and cladding/coating interfaces.[17] Only an approximate solution will be presented here. The modes of the set are linearly polarized (LP) and each is given a designation LP_{lm}, where l and m-1 give the number of azimuthal and radial nodes, respectively. The orders l and m are integers in the range[18]

$$\begin{aligned} l &= 0 \ldots 2V \\ m &= 1 \ldots V/(\pi - 1) \end{aligned} \tag{1.14}$$

where V is the normalized frequency[18]

$$V = \frac{2\pi a}{\lambda} NA \tag{1.15}$$

Note that the radius, *a,* and the numerical aperture, *NA,* determine the number of modes that can be carried by the fibre. The fibre may be manufactured with an *NA* and core radius such that a single mode or multiple modes will be guided over a range of wavelengths, giving rise to single mode and multimode fibres. The electric field distribution of a mode $\psi_{lm}(r,\theta)$ may be described by a Bessel function of the first kind, J_l, with order *l* in the core region and a modified Bessel function of the second kind, K_l, with order *l* in the cladding region[18]

$$\psi_{lm}(r,\theta) = \begin{cases} AJ_l(k_T r)\cos(l\theta) & r \le a \quad (core) \\ BK_l(\gamma r)\cos(l\theta) & r > a \quad (cladding) \end{cases} \tag{1.16}$$

Assuming an infinite cladding, the coefficients *A* and *B* are determined by the boundary condition $\psi_{lm}(a,\theta) = AJ_l(k_T a)\cos(l\theta) = BK_l(\gamma a)\cos(l\theta)$ so that $\psi_{lm}(r,\theta)$ is continuous and differentiable for all *r,θ.* The arguments of the Bessel functions depend on k_T and γ, which are constants depending on the fibre material and wavelength and are given by[18]

$$k_T = \left(n_{co}^2 k^2 - \beta^2\right)^{1/2} \tag{1.17}$$

$$\gamma = \left(\beta^2 - n_{cl}^2 k^2\right)^{1/2} \tag{1.18}$$

where *k* is the wave number ($k = 2\pi/\lambda$), and β is the propagation constant of the fibre. The field intensity (proportional to $\psi_{lm}^2(r,\theta)$) of the three lowest-order LP modes was simulated using Matlab and is shown in Figure 1.5.

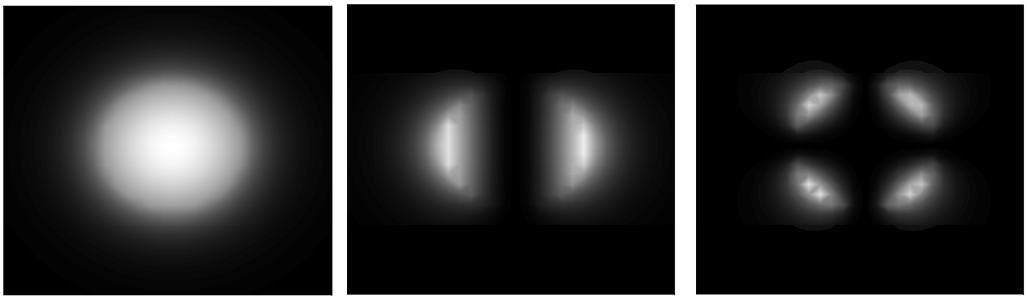

Figure 1.5: Contour plots of $\psi_{lm}^2(r,\theta)$ for the LP_{01}, LP_{11}, and LP_{21} modes.

Notice that $BK_n(\gamma r)$ in equation (1.16) is non-zero – some fraction of light in every core mode is carried by the cladding. As a consequence, each core mode experiences an effective refractive index n_{eff} that depends on how much of the light is carried in the core and in the cladding. A mode will be guided as long as its effective refractive index lies between the core and cladding indices:

$$n_{cl} < n_{eff} = \beta / k < n_{co} \tag{1.19}$$

The portion of a mode carried outside the core is termed the evanescent wave. Its intensity can be approximated as an exponentially decaying function of the distance from the core/cladding interface. The intensity is $1/e$ of its initial value at d_p, the depth of penetration

$$d_p = \frac{\lambda}{2\pi\sqrt{n_{co}^2 \sin^2 \phi_i - n_{cl}^2}} \tag{1.20}$$

where ϕ_i is the angle of incidence at the interface.[19] The evanescent wave may be used for performing absorption sensing using fibre cavity and fibre loop ringdown spectroscopy (FCRDS and FLRDS) and is detailed below (Chapter 1.4.1 and 1.4.2). In

Chapter 3, two fibre couplers were constructed that rely on the evanescent wave of cladding modes for their operation.

1.4 Literature Review

1.4.1 Cavity Ringdown Spectroscopy

An extensive historical review of cavity ringdown (CRD) methods has recently been published by Paldus et al.[20] and this section will therefore focus mainly on methods that are relevant to the work presented later. First, a summary of the beginnings of the methods used herein is given.

The origin of cavity ringdown spectroscopy lies in attempts to measure the reflectivity, R, of very high quality mirrors (e.g. $R > 0.99$). The first instance of this is the cavity-attenuated phase-shift method (a method now referred to as phase shift CRDS or FD-CRDS) reported by Herbelin et al.[21, 22] Here a *cw* laser was intensity modulated and the phase shift of the cavity output was detected using a lock-in amplifier. The phase shift was related to the total optical loss of the cavity, $1-R$, thus the individual mirror reflectivities could be determined from $R = R_1 R_2$. Anderson et al. later developed a method (now termed *cw*-CRDS) for a similar purpose that measures the ringdown time of the cavity directly.[23] A *cw* laser of constant intensity is coupled into the cavity and the cavity output is allowed to build up to a threshold value before the input is switched off using a Pockels cell. A ringdown trace can then be directly recorded. Both of these techniques, however, suffered from the problem of coupling the laser light to a resonant

cavity mode. If the laser cavity and optical cavity are not vibrationally well isolated, coupling of a laser mode to a cavity mode will occur at random. This can produce intensity fluctuations, differing delays between successive signals, and even non-exponential decays.[8]

Though it had been proposed by Herbelin et al., Deacon and O'Keefe report the first use of the cavity ringdown method for performing spectroscopy.[8] They avoided the problem of coupling to a single cavity mode by using a laser pulse shorter than the round-trip time of the cavity, which inherently is composed of a broad range of frequencies and couples to multiple modes[16] and every pulse enters the cavity (termed pulsed CRDS). They used this pulsed CRD spectroscopy method to record very weak forbidden transition ($b^1\Sigma_g \leftarrow X^3\Sigma_g$) of $O_2(g)$ near 690 and 630 nm, showing the enhanced detection limit afforded by the long effective absorption path length of CRDS – in their case about 10 km.

Since the example of Deacon and O'Keefe numerous variations of CRDS have been explored, in terms of both methodology and sample type. Other methods include cavity enhanced[24-26], phase shift[3, 27, 28], broadband[29-32], and evanescent wave[1, 12, 33] CRDS as well as CRD polarimetry[34] to study solid, liquid, gas and plasma phases. Today the most common mode of operation is related to the *cw*-CRDS technique introduced by Anderson et al. A high finesse cavity is aligned to work in single mode operation. The length of the cavity[35] or the laser wavelength[11] is varied over more than one free spectral range so that laser light couples into the cavity periodically. Whenever a cavity mode is

excited the intensity in the cavity builds up. A fast shutter then turns the laser light off when a threshold is exceeded and the ringdown of the cavity is recorded. The photon lifetime in the cavity can then be calculated from the build-up time or the ringdown time. This method provides high intracavity intensities and strong, low-noise ringdown signals.

Most of the research on ringdown methods applied to the liquid phase has focused on how to best interface the sample cell with the optical cavity. An early example by Xu et al. used one or two quartz sample cells (1 cm pathlength each) at Brewster's angle in a cavity that would normally be used for gas phase samples.[36] Brewster's angle, θ_B, is the angle at which the light plane-polarized parallel to the plane of incidence theoretically has no reflection loss. This angle is determined simply from $\tan\theta_B = n_t/n_i$ where n_t and n_i are the indices of the transmitted and incident media, respectively.[37] Orienting the cell(s) at Brewster's angle reduces the loss caused by introducing them into the cavity. Xu et al. investigated the fifth overtone of the C-H stretch of benzene at various concentrations in hexane. The percentage relative area of the absorption peaks matched very well with the percentage benzene in solution and they achieved sensitivity (εC_{DL} = 2 x 10^{-7} cm^{-1}) comparable to non-ringdown methods. Zare et al. then presented a liquid CRDS apparatus that placed the liquid directly into contact with the cavity mirrors.[38] This eliminated the reflection loss Xu et al. experienced even with their cell at Brewster's angle, but since the pathlength of the cavity was 21 cm scattering and absorption loss from the solvent was considerably higher (Figure 1.6).

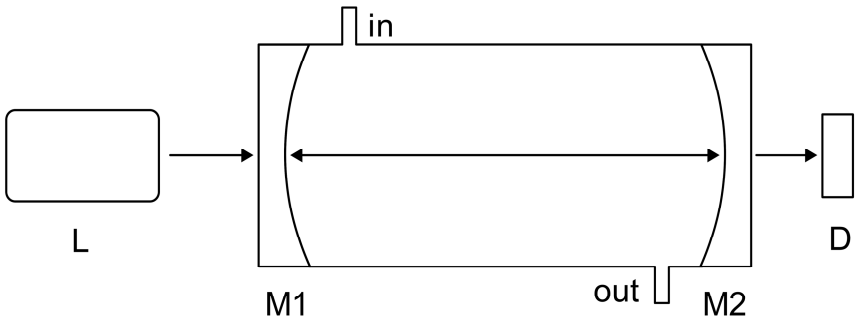

Figure 1.6: Bulk liquid CRDS apparatus of Zare et al.

Zare et al. flowed various concentrations of two laser dyes through their sample cell, however with such a long pathlength this required large volumes of both solvent and sample and had a slow response to concentration changes. They report a sensitivity of roughly the same order of magnitude as Xu ($\varepsilon C_{DL} = 10^{-6}$ cm^{-1}). Zare et al. later presented a refined version of Xu's apparatus where the light passing through the sample cell strikes all interfaces at Brewster's angle for a large range of sample refractive indices (Figure 1.7).

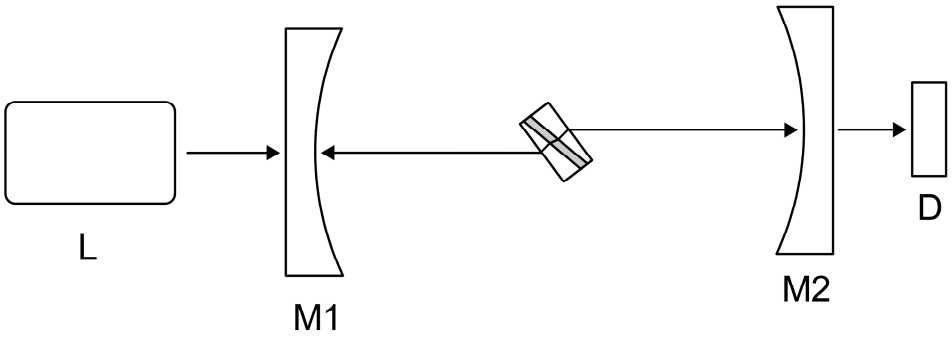

Figure 1.7: Brewster's angle flow cell of Zare et al. for interfacing HPLC with CRDS.

This custom designed flow cell had a 300 μm path length and was connected to the output of a high-performance liquid chromatography (HPLC) column, allowing the separated components of a mixture of anthraquinones to be detected ($\varepsilon C_{DL} = 2 \times 10^{-5}$ cm^{-1}).[37] Van

der Sneppen et al. reported a method akin to Zare's long pathlength apparatus, but with a much smaller volume, allowing it to be interfaced to an HPLC machine.[39] The two mirrors making up the miniature cavity were separated by only 2mm and were in contact with the liquid (Figure 1.8).

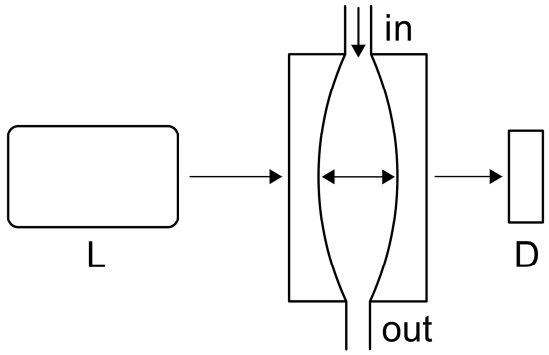

Figure 1.8: Miniature cavity used by van der Sneppen et al.

Experiments with flow injection of the dye crystal violet yielded a detection limit comparable to that obtained by Zare et al. for the Brewster's angle flow cell (εC_{DL} = 1.5 x 10^{-4} cm^{-1}). Disadvantages of the method of van der Sneppen et al. are the need for a short-pulse, large-bandwidth laser and fast detection electronics in order to couple to the mini-cavity and record its fast decay curves. Overall, these methods exhibit a detection limit equivalent to or better than a high quality UV-Vis absorption spectrometer.[37]

O'Keefe et al. applied the *cw*-CRDS method to an optical fibre cavity constructed from two fibre Bragg gratings (FBG) which act like mirrors (see Chapter 4) and was able to achieve 2 μs ringdown times.[13] They exposed the evanescent wave of the fibre core via a tapered region to solutions of differing refractive index and monitored the change in ringdown time (Figure 1.9). It was found that an enhancement factor of 100 is gained

over single pass evanescent wave detection of the external refractive index. They overcame the need for active mode-matching by using a 10 m long cavity which exhibits a pseudo-continuum of modes.

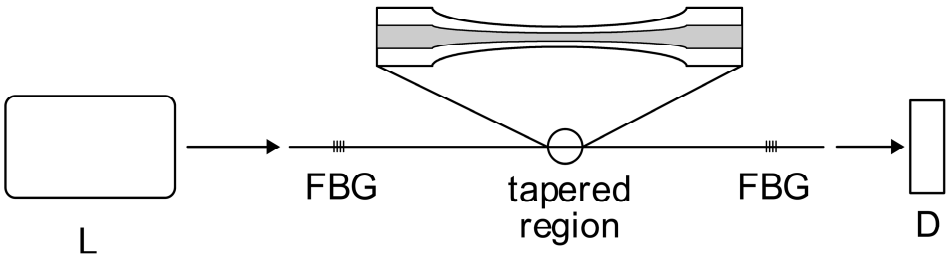

Figure 1.9: Fibre cavity resonator of O'Keefe et al.

1.4.2 Fibre-Loop Ringdown Spectroscopy

The first reported use of a fibre loop employed as an optical cavity for RDS came in 2001 from Stewart et al. where the technique was used for stand-off sensing of methane in landfills using a micro-optic gas cell of length 5 cm.[40] To counteract the high loss associated with the gas cell, an erbium doped fibre amplifier (EDFA) was included in the loop (Figure 1.10). This resulted in a long ringdown time (2.6 μs) but with the consequence of τ being dependent on the stability of the amplifier. Improvements to their system have yielded ringdown times of up to 9.8 ms but the problem of amplifier stability remains.[41]

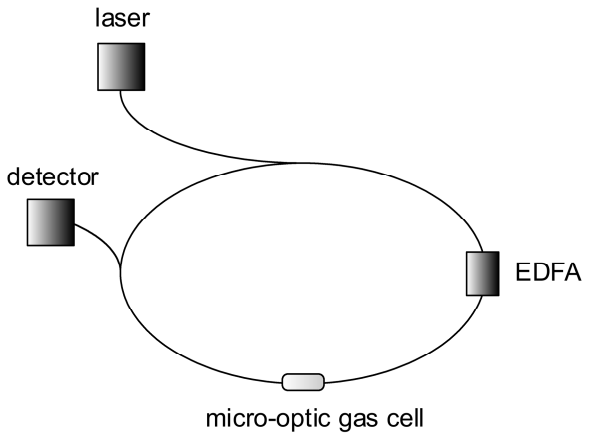

Figure 1.10: Active fibre loop for gas sensing of Stewart et al.

Soon after Stewart et al.'s initial report, our laboratory published the first report of a passive fibre loop for performing RDS.[14] A 12 m loop of multimode fibre exhibited a biexponential decay with time constants of 900 and 235 ns, corresponding to the decay of light in the core and cladding, respectively. A 3.8 μm gap in the loop allowed for introduction of a liquid sample while maintaining relatively high optical coupling (Figure 1.11). The absorption spectrum of the dye DDCI was recorded and a detection limit of εC = 100 cm^{-1} determined. Later work demonstrated that performing ringdown measurements in the frequency domain (see Chapter 2) enhanced the detection limit to εC = 2 cm^{-1} and improved the time resolution to 100 ms.[42]

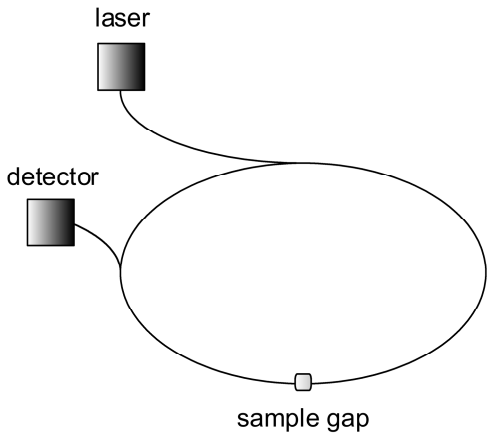

Figure 1.11: Passive fibre loop for liquid phase spectroscopy of Tong et al.

Lehmann et al. have made use of a tapered section of fibre in a passive loop to expose the evanescent field of a single core mode to an external medium (Figure 1.12). They recorded the absorption spectrum of the first vibrational overtone of 1-octyne between 1525 and 1550 nm, with an estimated detection limit of 1.05 % 1-octyne in a non-interacting solvent.[43] They later showed that single-cell detection is possible with a tapered fibre coated with poly-D-lysine to concentrate the cells in the evanescent field.[44]

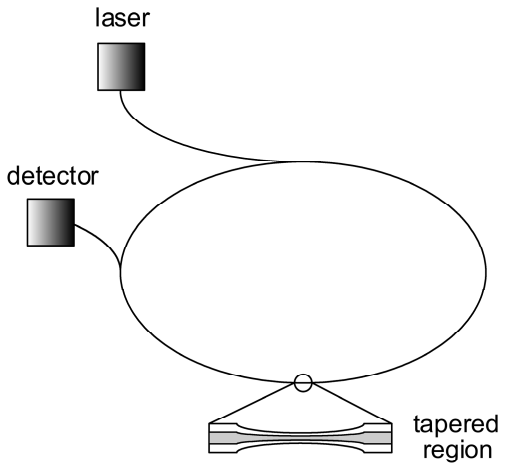

Figure 1.12: Passive fibre loop for liquid phase spectroscopy via the evanescent wave of Lehmann et al.

1.5 Conclusion

The need for low detection limit, sensitive absorption measurements has prompted the development of the field of ringdown spectroscopy. There are now a number of examples of optical cavities and loops being applied to spectroscopy of the liquid phase. The following chapters present some variations, improvements, and new means for performing ringdown spectroscopy on very small liquid volumes intended to find application in analyte detection for micro total analysis systems.

1.6 References

1. Shaw, A. M.; Hannon, T. E.; Li, F. P.; Zare, R. N., Adsorption of crystal violet to the silica-water interface monitored by evanescent wave cavity ring-down spectroscopy. *Journal of Physical Chemistry B* **2003,** 107, (29), 7070-7075.

2. Mazurenka, M.; Orr-Ewing, A. J.; Peverall, R.; Ritchie, G. A. D., Cavity ring-down and cavity enhanced spectroscopy using diode lasers. *Annual Reports on the Progress of Chemistry, Section C: Physical Chemistry* **2005,** 101, 100-142.

3. van Helden, J. H.; Schram, D. C.; Engeln, R., Phase-shift cavity ring-down spectroscopy to determine absolute line intensities. *Chemical Physics Letters* **2004,** 400, (4-6), 320-325.

4. Berden, G.; Peeters, R.; Meijer, G., Cavity ring-down spectroscopy: Experimental schemes and applications. *International Reviews in Physical Chemistry* **2000,** 19, (4), 565-607.

5. Vallance, C., Innovations in cavity ringdown spectroscopy. *New Journal of Chemistry* **2005,** 29, (7), 867-874.

6. Wheeler, M. D.; Newman, S. M.; Orr-Ewing, A. J.; Ashfold, M. N. R., Cavity ring-down spectroscopy. *Journal of the Chemical Society-Faraday Transactions* **1998,** 94, (3), 337-351.

7. Brown, S. S., Absorption spectroscopy in high-finesse cavities for atmospheric studies. *Chemical Reviews* **2003,** 103, (12), 5219-5238.

8. O'Keefe, A.; Deacon, D. A. G., Cavity Ring-Down Optical Spectrometer for Absorption-Measurements Using Pulsed Laser Sources. *Review of Scientific Instruments* **1988,** 59, (12), 2544-2551.

9. Paldus, B. A.; Harb, C. C.; Spence, T. G.; Wilke, B.; Xie, J.; Harris, J. S.; Zare, R. N., Cavity-locked ring-down spectroscopy. *Journal of Applied Physics* **1998,** 83, (8), 3991-3997.

10. Morville, J.; Romanini, D.; Kachanov, A. A.; Chenevier, M., Two schemes for trace detection using cavity ringdown spectroscopy. *Applied Physics B-Lasers and Optics* **2004,** 78, (3-4), 465-476.

11. Schulz, K. J.; Simpson, W. R., Frequency-matched cavity ring-down spectroscopy. *Chemical Physics Letters* **1998,** 297, (5-6), 523-529.

12. Pipino, A. C. R.; Hudgens, J. W.; Huie, R. E., Evanescent wave cavity ring-down spectroscopy with a total-internal-reflection minicavity. *Review of Scientific Instruments* **1997,** 68, (8), 2978-2989.

13. Gupta, M.; Jiao, H.; O'Keefe, A., Cavity-enhanced spectroscopy in optical fibers. *Optics Letters* **2002,** 27, (21), 1878-1880.

14. Brown, R. S.; Kozin, I.; Tong, Z.; Oleschuk, R. D.; Loock, H. P., Fiber-loop ring-down spectroscopy. *Journal of Chemical Physics* **2002,** 117, (23), 10444-10447.

15. von Klitzing, W.; Long, R.; Ilchenko, V. S.; Hare, J.; Lefevre-Seguin, V., Tunable whispering gallery modes for spectroscopy and CQED experiments. *New Journal of Physics* **2001,** 3, 141-1414.

16. Lehmann, K. K.; Romanini, D., The superposition principle and cavity ring-down spectroscopy. *Journal of Chemical Physics* **1996,** 105, (23), 10263-10277.

17. Keiser, G., *Optical Fiber Communications*. 3 ed.; McGraw-Hill Higher Education: 2000.

18. Saleh, B. E. A.; Teich, M. C., *Fundamentals of Photonics*. John Wiley & Sons, Inc.: 1991.

19. Palais, J. C., *Fiber Optic Communications*. 4 ed.; Prentice-Hall Inc.: 1998.

20. Paldus, B. A.; Kachanov, A. A., An historical overview of cavity-enhanced methods. *Canadian Journal of Physics* **2005,** 83, (10), 975-999.

21. Herbelin, J. M.; McKay, J. A., Development of Laser Mirrors of Very High Reflectivity Using the Cavity-Attenuated Phase-Shift Method. *Applied Optics* **1981,** 20, (19), 3341-3344.

22. Herbelin, J. M.; McKay, J. A.; Kwok, M. A.; Ueunten, R. H.; Urevig, D. S.; Spencer, D. J.; Benard, D. J., Sensitive Measurement of Photon Lifetime and True Reflectances in an Optical Cavity by a Phase-Shift Method. *Applied Optics* **1980,** 19, (1), 144-147.

23. Anderson, D. Z.; Frisch, J. C.; Masser, C. S., Mirror Reflectometer Based on Optical Cavity Decay Time. *Applied Optics* **1984,** 23, (8), 1238-1245.

24. Barry, H. R.; Corner, L.; Hancock, G.; Peverall, R.; Ritchie, G. A. D., Cavity-enhanced absorption spectroscopy of methane at 1.73 mu m. *Chemical Physics Letters* **2001,** 333, (3-4), 285-289.

25. Bakowski, B.; Corner, L.; Hancock, G.; Kotchie, R.; Peverall, R.; Ritchie, G. A. D., Cavity-enhanced absorption spectroscopy with a rapidly swept diode laser. *Applied Physics B-Lasers and Optics* **2002,** 75, (6-7), 745-750.

26. He, Y. B.; Orr, B. J., Ringdown and cavity-enhanced absorption spectroscopy using a continuous-wave tunable diode laser and a rapidly swept optical cavity. *Chemical Physics Letters* **2000,** 319, (1-2), 131-137.

27. Engeln, R.; vonHelden, G.; Berden, G.; Meijer, G., Phase shift cavity ring down absorption spectroscopy. *Chemical Physics Letters* **1996,** 262, (1-2), 105-109.

28. Lewis, E. K.; Moehnke, C. J.; Manzanares, C. E., Phase shift cavity ring down and FT-VIS measurements of C-H (Delta upsilon=5) vibrational overtone absorptions. *Chemical Physics Letters* **2004,** 394, (1-3), 25-31.

29. Ball, S. M.; Jones, R. L., Broad-Band Cavity Ring-Down Spectroscopy. *Chemical Reviews (Washington, DC, United States)* **2003,** 103, (12), 5239-5262.

30. Ball, S. M.; Povey, I. M.; Norton, E. G.; Jones, R. L., Broadband cavity ringdown spectroscopy of the NO3 radical. *Chemical Physics Letters* **2001,** 342, (1-2), 113-120.

31. Scherer, J. J., Ringdown spectral photography. *Chemical Physics Letters* **1998,** 292, (1-2), 143-153.

32. Thorpe, M. J.; Moll, K. D.; Jones, R. J.; Safdi, B.; Ye, J., Broadband Cavity Ringdown Spectroscopy for Sensitive and Rapid Molecular Detection. *Science (Washington, DC, United States)* **2006,** 311, (5767), 1595-1599.

33. Pipino, A. C. R., Ultrasensitive surface spectroscopy with a miniature optical resonator. *Physical Review Letters* **1999,** 83, (15), 3093-3096.

34. Muller, T.; Wiberg, K. B.; Vaccaro, P. H., Cavity ring-down polarimetry (CRDP): A new scheme for probing circular birefringence and circular dichroism in the gas phase. *Journal of Physical Chemistry A* **2000,** 104, (25), 5959-5968.

35. Romanini, D.; Kachanov, A. A.; Sadeghi, N.; Stoeckel, F., CW cavity ring down spectroscopy. *Chemical Physics Letters* **1997,** 264, (3-4), 316-322.

36. Xu, S. C.; Sha, G. H.; Xie, J. C., Cavity ring-down spectroscopy in the liquid phase. *Review of Scientific Instruments* **2002,** 73, (2), 255-258.

37. Snyder, K. L.; Zare, R. N., Cavity ring-down spectroscopy as a detector for liquid chromatography. *Analytical Chemistry* **2003,** 75, (13), 3086-3091.

38. Hallock, A. J.; Berman, E. S. F.; Zare, R. N., Direct monitoring of absorption in solution by cavity ring-down spectroscopy. *Analytical Chemistry* **2002,** 74, (7), 1741-1743.

39. van der Sneppen, L.; Wiskerke, A.; Ariese, F.; Gooijer, C.; Ubachs, W., Improving the sensitivity of HPLC absorption detection by cavity ring-down spectroscopy in a liquid-only cavity. *Analytica Chimica Acta* **2006,** 558, (1-2), 2-6.

40. Stewart, G.; Atherton, K.; Yu, H. B.; Culshaw, B., An investigation of an optical fibre amplifier loop for intra-cavity and ring-down cavity loss measurements. *Measurement Science & Technology* **2001,** 12, (7), 843-849.

41. Stewart, G.; Sheilds, P.; Culshaw, B., Development of fibre laser systems for ring-down and intracavity gas spectroscopy in the near-IR. *Meas. Sci. Technol.* **2004,** 15, 1621-1628.

42. Tong, Z. G.; Wright, A.; McCormick, T.; Li, R. K.; Oleschuk, R. D.; Loock, H. P., Phase-shift fiber-loop ring-down spectroscopy. *Analytical Chemistry* **2004,** 76, (22), 6594-6599.

43. Tarsa, P. B.; Rabinowitz, P.; Lehmann, K. K., Evanescent field absorption in a passive optical fiber resonator using continuous-wave cavity ring-down spectroscopy. *Chemical Physics Letters* **2004,** 383, (3-4), 297-303.

44. Tarsa, P. B.; Wist, A. D.; Rabinowitz, P.; Lehmann, K. K., Single-cell detection by cavity ring-down spectroscopy. *Applied Physics Letters* **2004,** 85, (19), 4523-4525.

Chapter 2 Ringdown Theory

As in fluorescence spectroscopy,[1] decay lifetime measurements for absorption spectroscopy in a ringdown cavity/loop can be performed either in the time domain (TD) or the frequency domain (FD). Here a time domain measurement involves recording the time dependent light intensity exiting the cavity. In the frequency domain, the frequency dependent phase shift and/or modulation depth of the signal exiting the cavity is recorded, rather than the frequency dependent intensity. In this chapter the theoretical foundation for measurements in both these domains is covered.

The FD technique originated in 1933 for the purpose of determining fluorescence decay lifetimes.[2] Since then it has been more fully developed to include multi-exponential decay behaviour[3] and has even been used for fluorescence lifetime imaging microscopy, where the technique is applied to every pixel of an image[4]. To the knowledge of the author, there are only two reports of the characterization of bi-exponential decays in the context of FD-CRDS.[5, 6] These reports include equations that appear at first glance to be different from the ones presented here, but can be shown to be equivalent if some assumptions are made. However, both papers lack a general theory that can be extended to multi-exponential decays. Such generally applicable expressions are developed below.

2.1 Time Domain

In the time domain, the intensity as a function of time coupled out of a cavity or loop resulting from an instantaneous (delta function) input is given by the impulse response function *I(t)*. This will be a single or multi-exponential decay depending on the properties of the system.[†,7] Each decay, i, has an amplitude, a_i, and decay time, τ_i, associated with it. The general case for N concurrent decays can be expressed as the sum of exponentials and is given by

$$I(t) = \sum_{i=1}^{N} a_i e^{-t/\tau_i} \tag{2.1}$$

The amplitude and ringdown time can be obtained from experiment by fitting the cavity or loop output to a single or multi-exponential function using a non-linear least-squares (Levenberg-Marquardt) fitting method.[8] In practice the laser input pulse is not infinitely short, but provided that the rise and fall times of the pulse are less than the shortest ringdown time, all τ values can be readily determined. (A general expression for the cavity/loop output given any arbitrary laser input is presented below.) If the pulse is longer than the round-trip time, t_r, of the cavity/loop then the fitting procedure is quite straightforward and the decay constant may be determined from either the build-up (given by $\sum_i 1 - I_i(t)$) or ringdown of the system. If the input pulse is shorter than the round-trip time then the (multi-) exponential curve is fit not to the cavity output, which shows discrete pulses, but to its envelope. These two cases are shown in Figure 2.1.

[†] More complicated decay processes are possible. For example, a cavity in which a small number of longitudinal modes are excited may show a heterodyne mode beating superimposed on the exponential decay if the emitted light from the cavity has a long coherence length.

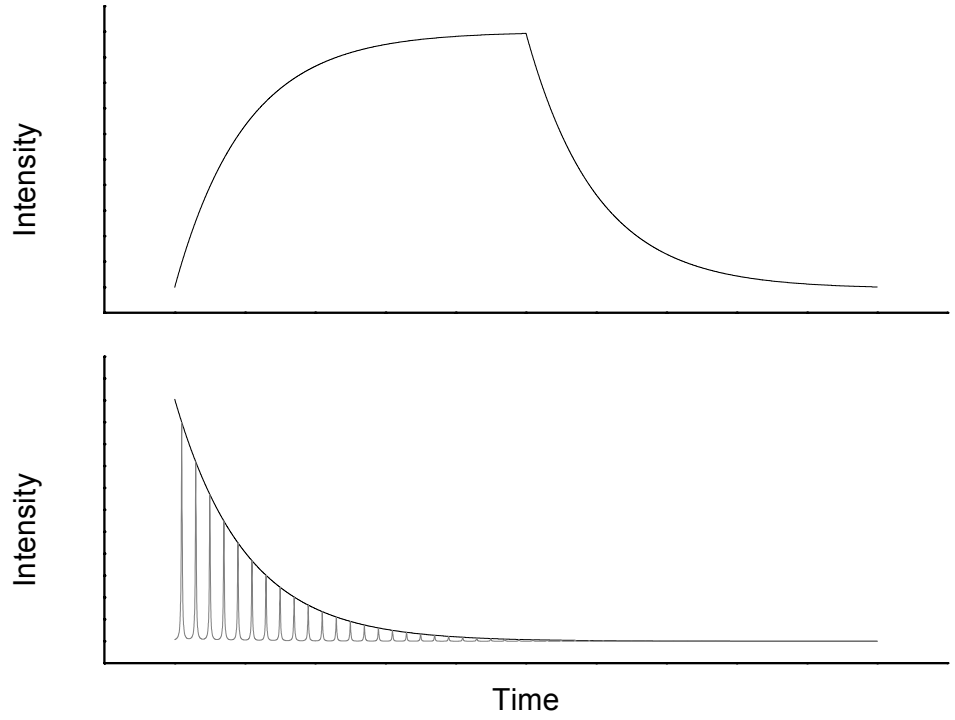

Figure 2.1: Simulated cavity output for an input pulse longer (upper plot) and shorter (lower plot) than the round-trip time.

There are advantages and disadvantages to each method. If the pulse is shorter than t_r then the round-trip time, and hence the length of the cavity/loop, L, can be easily determined from the difference in time between the peaks of the individual pulses. However, the total number of pulses emitted can affect how reliable the ringdown time and amplitude from a fit is. For example, if only 15 emitted pulses are observed, then only 15 points define the shape of the envelope used for fitting. This problem was discussed in detail by Jakubinek et al.[9] Using a pulse longer than t_r provides a curve with many more points and is ultimately limited by the time resolution and the buffer size of the sampler (usually an oscilloscope). More points are used for the fit, thus the error on the ringdown time and amplitude will be lower. The disadvantage here is that the round-

trip time and the length cannot be directly determined. Time domain measurements are used by the majority of researchers in the field, however another method exists, which we make use of, that determines the ringdown time and amplitude in the frequency domain.

2.2 Frequency Domain

In the frequency domain, the cavity or loop is excited by an intensity-modulated continuous-wave (*cw*) beam rather than by a pulse. This beam is usually sinusoidally modulated, though it can also be a square wave or any other periodic function. The measurand is no longer the intensity as a function of time, *I(t)*, but the phase angle, ϕ, or modulation depth, *m*, of the intensity-modulated cavity/loop output as a function of frequency. The modulation depth is defined as half the total amplitude of the output signal.[10] The phase angle is defined as the angle between the crossing of the modulated signals with their respective DC offsets for the input and output signals.[10] These are shown pictorially in Figure 2.2.

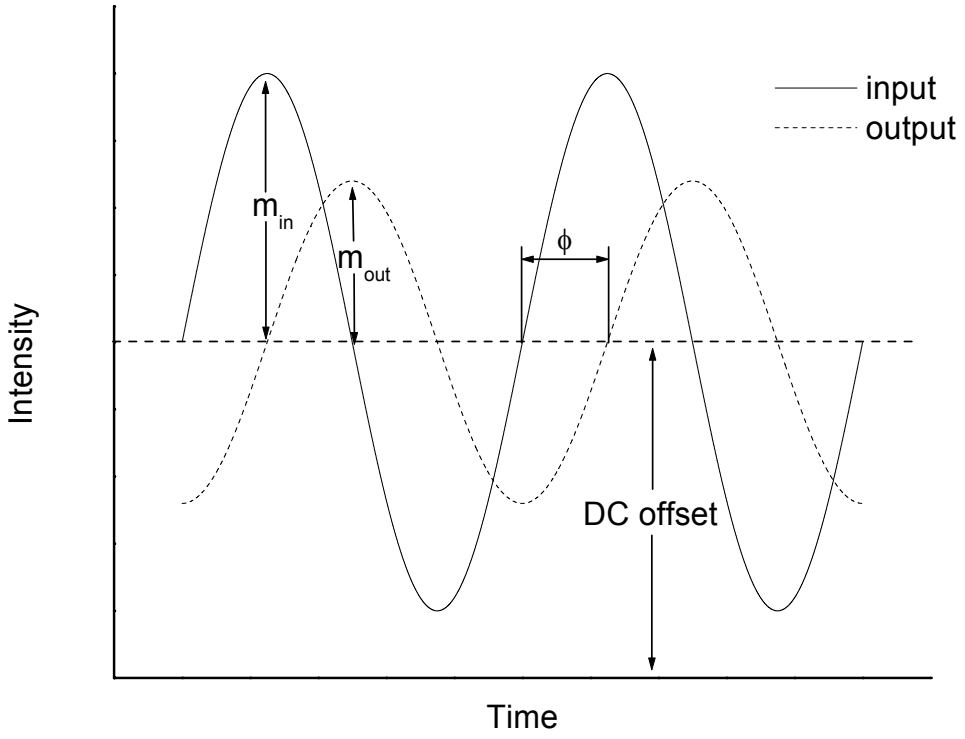

Figure 2.2: Depiction of the phase angle and modulation depth of the cavity output.

The modulation depth is measured from the peak amplitude to the DC offset of the signal. The phase angle is measured from the zero-crossings of the AC component of each signal, which occur at their respective DC offsets.

The cavity/loop output for an arbitrary input can be obtained by using expressions common in signal processing and can be applied to the determination of ringdown times. Mathematically, the cavity/loop output is related to the input by the convolution of the input waveform with the impulse response function (2.1) and is given by

$$f_{out}(t) = f_{in}(t) \otimes I(t) = \int_0^t f_{in}(t') I(t - t') dt' \qquad (2.2)$$

With this expression, nearly any cavity/loop output can be simulated given that the input and impulse response functions are known.[11, 12] (It is limited to input signals with features longer than t_r since reflection is not explicitly treated.) Similarly, the impulse

response function can be found by deconvolution of the cavity output, another method of finding a and τ that will be discussed later (Chapter 8). The cavity output for a sine wave input, such as that shown in Figure 2.2, is

$$I(t) = b + 2m\sin(\omega t + \phi) \tag{2.3}$$

where b is the DC offset, ω is the angular frequency ($\omega = 2\pi f$) and m and ϕ are the *overall* modulation and phase shift resulting from N decay components.

2.2.1 Derivation

To convert the impulse response function (IRF) from the time domain to the frequency domain the Laplace transform is used. From the transformed IRF, the overall phase and modulation can be written in terms of the individual decay components. In general, the Laplace transform of a function *f(t)* for $t \geq 0$ is given by

$$F(\omega) = L\left[f(t)\right](s) \equiv \int_0^\infty f(t)e^{-st}dt \tag{2.4}$$

where

$$s = \sigma + i\omega \tag{2.5}$$

Here i is the imaginary unit ($i = \sqrt{-1}$) and for an undamped function $\sigma = 0$. The Laplace transform of equation (2.1) is thus

$$I(\omega) = L\left[I(t)\right](i\omega) = \sum_{i=1}^{N} \frac{a_i}{i\omega + 1/\tau_i} \tag{2.6}$$

This expression must be related to the measurands of phase angle and modulation depth. Figure 2.3 shows a plot of the vector *I(ω)* in the complex plane.

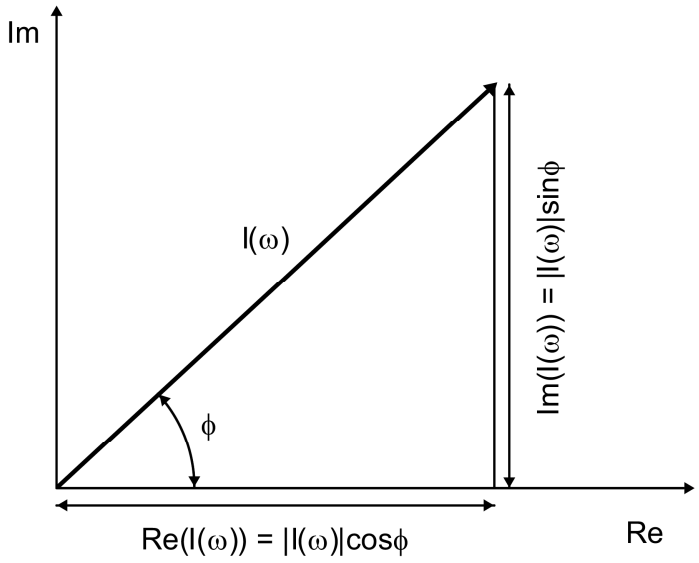

Figure 2.3: Frequency domain impulse response function plotted in the complex plane.

Using basic trigonometry the phase angle can be related to the imaginary (Im) and real (Re) components of $I(\omega)$ by

$$\tan\phi = \frac{\mathrm{Im}\left(I(\omega)\right)}{\mathrm{Re}\left(I(\omega)\right)} = \frac{-\sum_{i=1}^{N} \frac{a_i \tau_i^2 \omega}{1+\omega^2\tau_i^2}}{\sum_{i=1}^{N} \frac{a_i \tau_i}{1+\omega^2\tau_i^2}} \tag{2.7}$$

The modulation depth, m, is given by the magnitude of the transformed response function, $|I(\omega)|$, normalized by J

$$m = \frac{\left|I(\omega)\right|}{J} = \sqrt{\frac{\mathrm{Im}\left(I(\omega)\right)^2 + \mathrm{Re}\left(I(\omega)\right)^2}{J^2}} \tag{2.8}$$

where J is the total steady-state intensity, the sum of all integrals of the exponential decays given by equation (2.1))

$$J = \sum_{i=1}^{N}\left(\int_0^{\infty} a_i e^{-t/\tau_i} dt\right) = \sum_{i=1}^{N} a_i \tau_i = \sum_{i=1}^{N} \alpha_i \tag{2.9}$$

If the total steady-state intensity is normalized (J = 1) then equations (2.7) and (2.8) simplify to[4]

$$\tan\phi = \frac{-\sum_{i=1}^{N} \frac{\alpha_i \tau_i \omega}{1+\omega^2\tau_i^2}}{\sum_{i=1}^{N} \frac{\alpha_i}{1+\omega^2\tau_i^2}} \tag{2.10}$$

$$m = \left|I(\omega)\right| = \sqrt{\left(-\sum_{i=1}^{N} \frac{\alpha_i \tau_i \omega}{1+\omega^2\tau_i^2}\right)^2 + \left(\sum_{i=1}^{N} \frac{\alpha_i}{1+\omega^2\tau_i^2}\right)^2} \tag{2.11}$$

Equations (2.10) and (2.11) are the general forms commonly used by the fluorescence spectroscopy community.

The overall phase shift and modulation depth can also be written in terms of the phase and modulation of each decay component i. From the vector diagram in Figure 2.4 where the two-component case is shown, it is apparent that for the case of N decay components

$$\tan\phi = \frac{\sum_{i=1}^{N} \left|I_i\right| \sin\phi_i}{\sum_{i=1}^{N} \left|I_i\right| \cos\phi_i} \tag{2.12}$$

$$m = \sqrt{\left(\sum_{i=1}^{N} \left|I_i\right| \sin\phi_i\right)^2 + \left(\sum_{i=1}^{N} \left|I_i\right| \cos\phi_i\right)^2} \tag{2.13}$$

It is also obvious that the phase and modulation of each vector is independent of the others so one may write

$$\tan\phi_i = \frac{\sin\phi_i}{\cos\phi_i} = -\omega\tau_i \tag{2.14}$$

$$m_i = |I_i| = \sqrt{\left(|I_i|\sin\phi_i\right)^2 + \left(|I_i|\cos\phi_i\right)^2} = \frac{\alpha_i}{\sqrt{1+\omega^2\tau_i^2}} \tag{2.15}$$

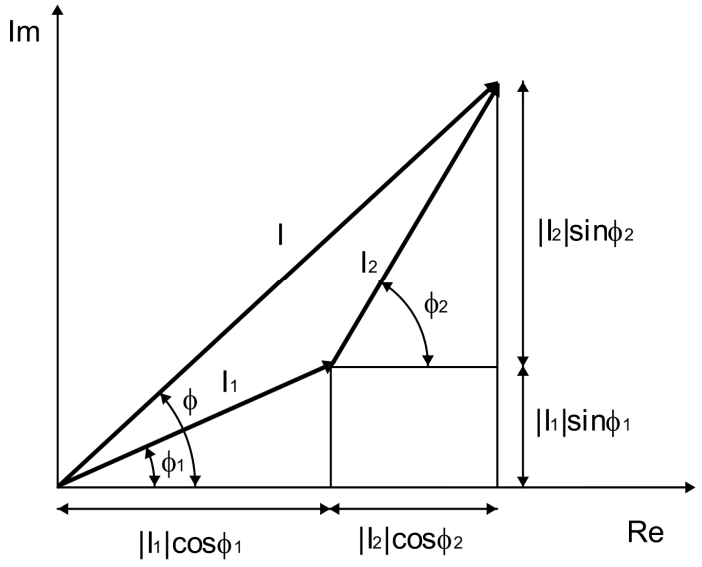

Figure 2.4: I(ω) for the two component case in the complex plane.

Equations (2.10) and (2.12) can be shown to be identical by substituting ϕ_i and m_i from (2.14) and (2.15) into (2.12) and simplifying. Likewise (2.11) and (2.13) can be shown to be equivalent by performing the same procedure. It is interesting to note that the simplest expression relating the time domain metrics to the frequency domain metrics is

$$\alpha_i = a_i\tau_i = \frac{m_i}{\cos\phi_i} \tag{2.16}$$

With this equation, one may now write the time domain impulse response function entirely in terms of frequency domain metrics:

$$I(t) = -\omega\sum_{i=1}^{N}\frac{m_i}{\sin\phi_i}\exp\left(\frac{\omega t}{\tan\phi_i}\right) \tag{2.17}$$

Equations (2.10) and (2.11) demonstrate that experimentally one can independently obtain the ringdown times and the relative contributions of all exponential decays in two ways, i.e. either from the phase shift or from the changes in modulation depth as long as both are determined as a function of frequency. However, the overall modulation must be normalized by the measured modulation for $\omega \to 0$ in order for the ringdown times to be extracted. In this respect, the phase angle is truly independent of the intensity, while the modulation is not, until normalized.

2.2.2 Comparison

Kasyutich et al. and Engeln et al. both use a specific form of the general expression given by (2.12) in their descriptions of a bi-exponential decay in FD-CRDS.[5, 6] The expression of Kasyutich et al. can be shown to be exactly identical to the result obtained from (2.12) for a bi-exponential with the assumption that one phase angle is zero (see 2.4 Appendix). In their experiment one phase angle is measured independently and then offset to zero on a lock-in amplifier. Engeln et al. present an expression that appears similar to (2.12), but closer inspection seems to prove otherwise. The contention comes in the form of the phase angle used in the expression. They write the equation

$$\Psi = \arctan\left(\frac{A'\sin\Delta\phi_A + B'\sin\left(\phi_o - \phi_B\right)}{A'\cos\Delta\phi_A + B'\cos\left(\phi_o - \phi_B\right)}\right) \tag{2.18}$$

where Ψ is the overall phase, A' and B' are the normalized intensities of decay A and B, ϕ_o is the phase of the empty cavity, and ϕ_B is the phase of decay B. The term $\Delta\phi_A$ is never clearly defined but one may assume it is $\Delta\phi_A = \phi_o - \phi_A$ by analogy. If one assumes

$A' = m_1$, $B' = m_2$, $\Delta\phi_A = \phi_1$, and $\Delta\phi_B = \phi_2$ then (2.18) equates with (2.12). However, the phase angles are not equal between the two models ($\Delta\phi_A \neq \phi_1$, $\Delta\phi_B \neq \phi_2$). In Engeln et al.'s case the phase angle used is relative to the phase of the empty cavity output, whereas in our case the phase angle is relative to the phase of the cavity input (which is defined as zero). Only the phase relative to the cavity input can be related to the ringdown time, thus the argument of the sines and cosines in (2.18) should not be the difference of angles, $\Delta\phi_i$, but should be only ϕ_i.

2.2.3 Simulation

Simulated data is plotted in Figure 2.5 showing the behaviour of m and ϕ for single and bi-exponential systems. For the single exponential case, a decrease in ringdown time shifts the phase and modulation curves to the right, while an increase in ringdown time shifts the curves to the left.

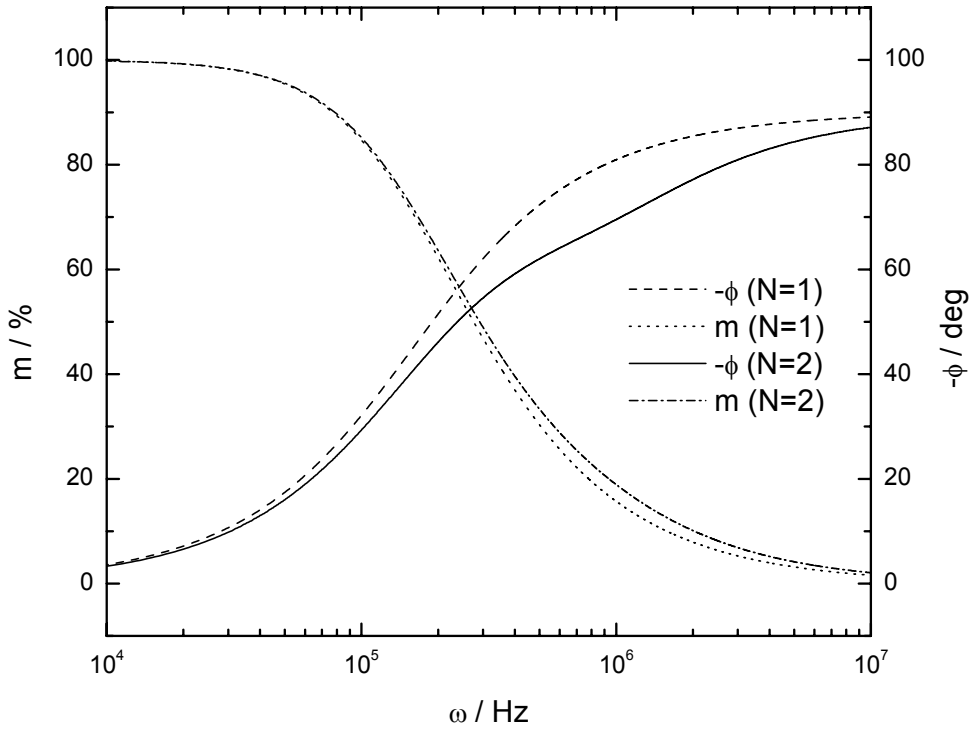

Figure 2.5: Dependence of the modulation depth and phase angle on angular frequency for single- and bi- exponential systems.

These plots were generated using the parameters τ = 1μs for the single exponential case and τ_1 = 1μs, τ_2 = 0.2μs, a_1 = 0.7 for the biexponential case.

A fit of equation (2.7) or (2.8) to the data yields the amplitude(s) and ringdown time(s). The number of parameters to be fit scales as *2N*. However this number can be reduced to *2N-1* since one of the steady-state intensities can be written in terms of the others by rearranging equation (2.9) to read

$$\alpha_N = 1 - \sum_{i=1}^{N-1} \alpha_i \qquad (2.19)$$

For the case of a single exponential decay (N = 1) equations (2.7) and (2.8) simplify to the more familiar expressions of[13]

$$\tan\phi = -\omega\tau \tag{2.20}$$

and

$$m = \frac{1}{\sqrt{1+\omega^2\tau^2}} \tag{2.21}$$

Fitting in this case is much easier since α = 1 and equations (2.20) and (2.21) can be linearized. A plot of $\tan\phi$ versus ω yields a straight line with an intercept of zero and a slope of $-\tau$. Plotting $\frac{1}{m^2}-1$ versus ω^2 will give a straight line with slope τ^2. An example is given (Figure 2.6) comparing the frequency dependence of $\tan\phi$ and $\frac{1}{m^2}-1$ for a biexponential system (with $\tau_1 > \tau_2$) and two single exponential decays with the same ringdown times. One notes that at no frequency does the slope for the biexponential system reflect the value of either of the ringdown times. Depending of the values of the decay times and amplitudes, the slope of $\tan\phi$ may even be positive at some frequencies.

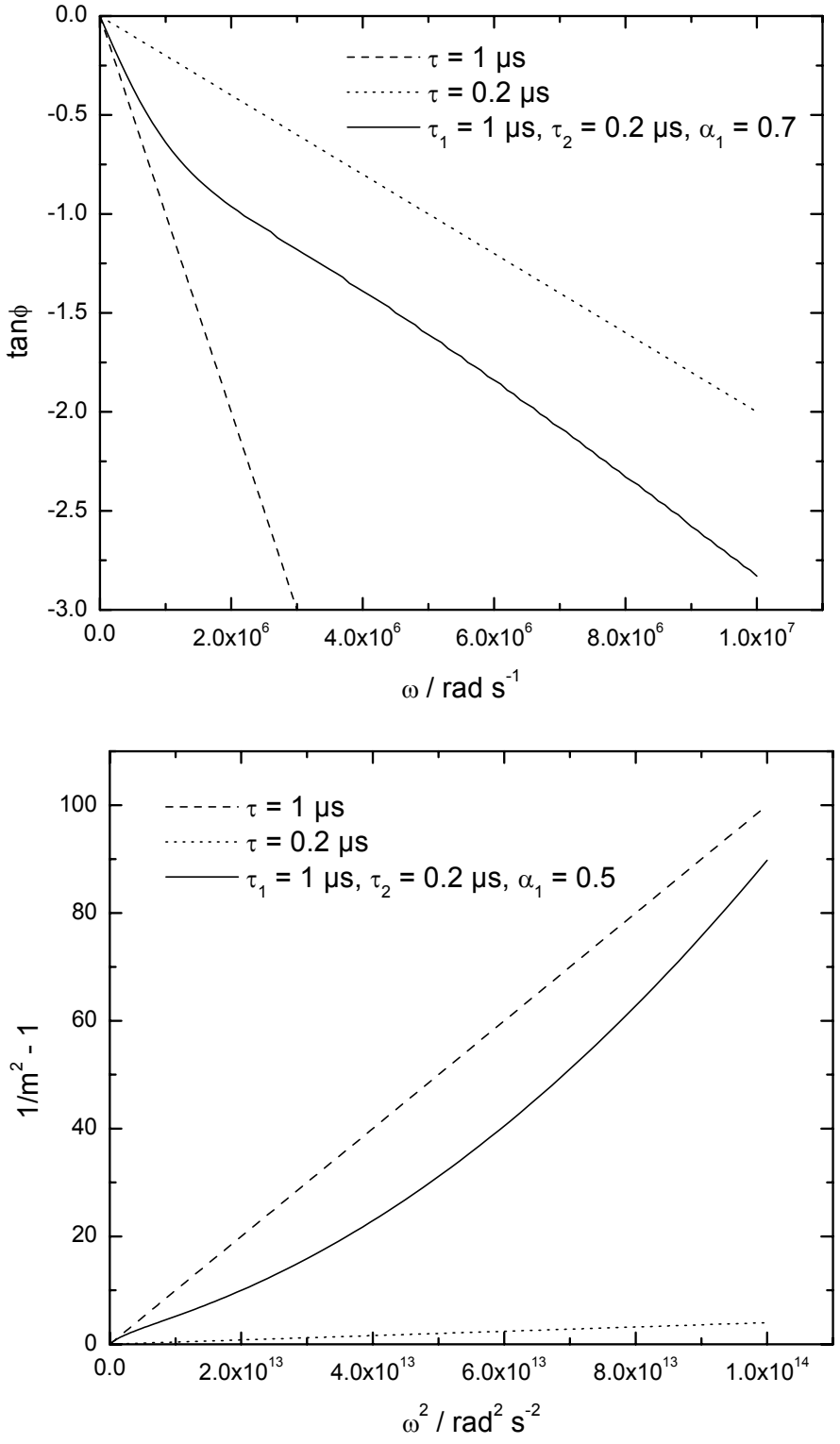

Figure 2.6: Comparison of tanϕ and *m* for single and biexponential decays.

2.2.4 Practical considerations

Lakowicz et al. give a detailed discussion of the resolvability of decay times in the frequency domain.[3] Based on the choice of frequency range, it is possible to resolve very similar decays with a ratio of 1.4:1 as well as very dissimilar decays with a ratio of 500:1. In both these regimes, they state the resolvability is better than that that can be achieved from time domain measurements.

When acquiring an electropherogram or other time trace, the phase angle as a function of time is recorded. For this purpose there is a single optimal modulation frequency, ω_{opt}, where the change in phase angle with ringdown time is the greatest. In general it is the frequency at which the slope of a plot of ϕ versus ω is at its global minimum. It can be found mathematically from the real, positive solutions of ω for

$$\frac{d^2\phi}{d\omega^2} = 0 \qquad (2.22)$$

This result is appropriate only if the range of analyte concentrations that is to be investigated is small since $\tau \propto 1/C$. For a single exponential system the optimal angular frequency found by solving equation (2.22) is simply $\omega_{opt} = 1/\tau$. Figure 2.7 shows a plot of the second derivative of ϕ with respect to ω for a bi-exponential system for which ω_{opt} = 9.28 x 10^5 rad s^{-1}. For some values of τ_1, τ_2, and a_1, there will be more than one real, positive solution of ω representing a second minimum at higher frequency than ω_{opt}.

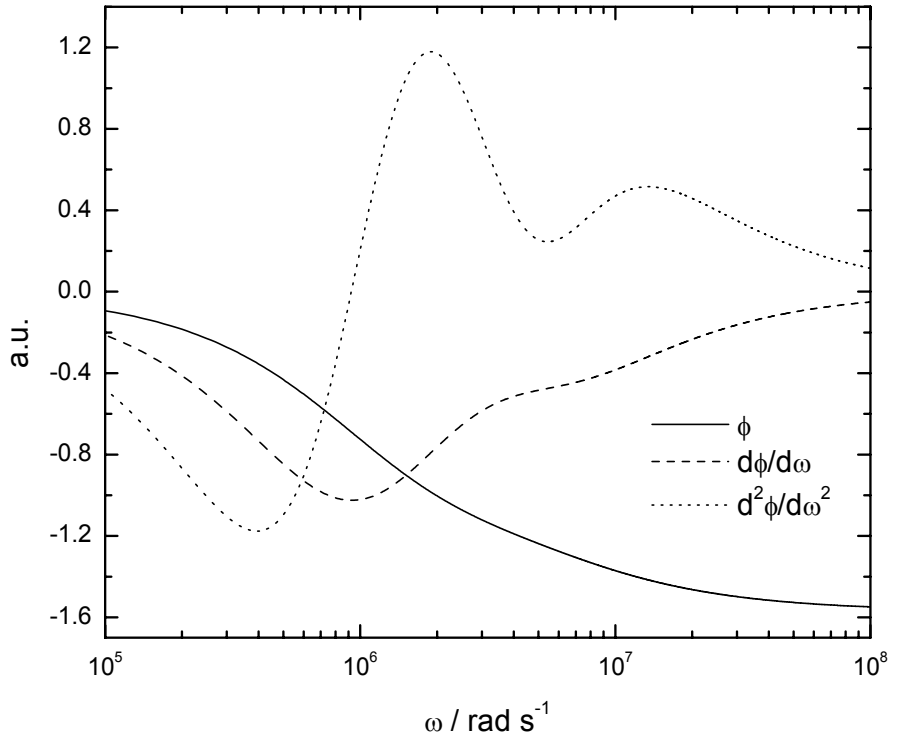

Figure 2.7: Illustration of the optimal working frequency, ω_{opt}.

The plot shows ϕ and its first and second derivatives for a biexponential system with parameters τ_1 = 1μs, τ_2 = 0.2μs, a_1 = 0.7.

It should be noted that in practice there is a frequency dependent offset phase angle, ϕ_o, that arises from delays in the electronics and cables which is included in the phase angle measured by the lock-in amplifier, ϕ_m.[5] The true phase angle, ϕ, which has been referred to thus far is then the difference of the measured phase and the phase offset

$$\phi = \phi_m - \phi_o \tag{2.23}$$

The phase offset must be measured or fit at all modulation frequencies, and then subtracted to obtain the true phase angle and hence the true ringdown time(s) and amplitude(s). Depending on the apparatus used, this can be a difficult process. This is a

complication that is unique to FD measurements and is especially a disadvantage for loop-based ringdown systems (Chapter 6).

The signal input channel of a lock-in amplifier is normally equipped with a narrow bandpass filter with a centre frequency matching the frequency of the reference input. This is to ensure no other frequencies, especially harmonic frequencies, interfere with the detection of the signal and the measurement of its phase angle. However, the lock-in amplifier used in the following experiments (SR844) suffers from an interesting problem in this regard. If the reference and signal inputs are both square waves, then the harmonics that are inherently contained in the square wave are passed and detected.[14] As a result the phase angle measured is not the phase of the fundamental frequency, but depends also on the phase of the harmonics. This can be modeled by modifying equation (2.10) to include a sum over N odd harmonic frequencies:

$$\tan\phi = -\frac{\sum_{i=1}^{M}\sum_{n=1}^{N}\frac{(2n-1)\omega\alpha_i\tau_i}{1+(2n-1)^2\omega^2\tau_i^2}}{\sum_{i=1}^{M}\sum_{n=1}^{N}\frac{\alpha_i}{1+(2n-1)^2\omega^2\tau_i^2}} \tag{2.24}$$

Even with this model it is difficult to correct for the contributions of higher harmonics, since the number of odd harmonics passed is not known and a weighting factor for each harmonic may need to be included due to some filtering nature still present in the lock-in amplifier. A much easier solution, and the one used below, is to always use a sinusoidally modulated reference input. Unfortunately, this problem was only realized after several months of inexplicable results were obtained.

2.3 Conclusion

The decay constants and modulation depths of a ringdown system can be determined in either the time or frequency domain. The overall phase and modulation can be related to the phases and modulations or to the amplitudes and ringdown times of each of the individual decays using the Laplace transform and a simple vector diagram. While TD measurements are generally easier to perform and fit, FD measurements have the advantages of better resolvability[3] and higher measurement repetition rate (Chapter 8). One drawback of working in the frequency domain is the necessity of determining the phase offset.

2.4 Appendix

Given here is a detailed proof that the expressions used by Kasyutich et al. are a special case of the general expressions given above (2.12). Kasyutich et al. measure ϕ_{ASE} (with the cavity misaligned) and subtract it from the measurement with an absorber present. However I_{ASE} cannot be subtracted so still contributes to the measured phase angle. He provides the vector diagram

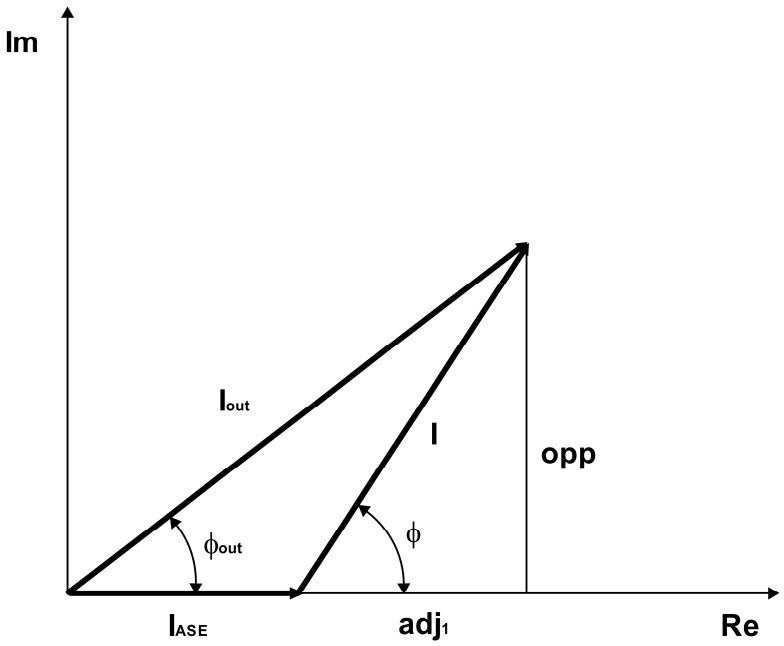

Figure 2.8: Vector diagram provided by Kasyutich et al.

In equation (5) he arrives at

$$\tan\varphi_{out} = \frac{I\sin\varphi}{I\cos\varphi + I_{ASE}}$$

We attempt to derive his equation starting from our general expression for $\tan\phi$ (2.12)and assuming $\phi_1 = \varphi_{\mathrm{ASE}} = 0$ (this phase angle was determined and then set to zero using the lock-in). Also we assume $\phi_2 = \varphi$, $|I_1(\omega)| = I_{\mathrm{ASE}}$, and $|I_2(\omega)| = I$.

$$\tan\phi = \frac{\sum_{i=1}^{N=2}\left|I_i(\omega)\right|\sin\phi_i}{\sum_{i=1}^{N=2}\left|I_i(\omega)\right|\cos\phi_i} = \frac{\left|I_1(\omega)\right|\sin\phi_1 + \left|I_2(\omega)\right|\sin\phi_2}{\left|I_1(\omega)\right|\cos\phi_1 + \left|I_2(\omega)\right|\cos\phi_2} = \frac{\left|I_1(\omega)\right|(0) + \left|I_2(\omega)\right|\sin\phi_2}{\left|I_1(\omega)\right|(1) + \left|I_2(\omega)\right|\cos\phi_2}$$

$$= \frac{\left|I_2(\omega)\right|\sin\phi_2}{\left|I_1(\omega)\right| + \left|I_2(\omega)\right|\cos\phi_2} = \frac{I\sin\varphi}{I_{ASE} + I\cos\varphi}$$

Our expression agrees with Kasyutich et al.'s.

We can also check if their expression for the modulation depth agrees with ours.

$$m = \sqrt{\sum_{i=1}^{N} \mathrm{Im}\left(I_i(\omega)\right)^2 + \sum_{i=1}^{N} \mathrm{Re}\left(I_i(\omega)\right)^2} = \left[\left(|I_1|\sin\phi_1 + |I_2|\sin\phi_2\right)^2 + \left(|I_1|\cos\phi_1 + |I_2|\cos\phi_2\right)^2\right]^{1/2}$$

$$= \left[\left(|I_1|(0) + |I_2|\sin\phi_2\right)^2 + \left(|I_1|(1) + |I_2|\cos\phi_2\right)^2\right]^{1/2}$$

$$= \left[\left(|I_2|\sin\phi_2\right)^2 + \left(|I_1| + |I_2|\cos\phi_2\right)^2\right]^{1/2}$$

$$= \left[|I_2|^2\sin^2\phi_2 + |I_1|^2 + 2|I_1||I_2|\cos\phi_2 + |I_2|^2\cos^2\phi_2\right]^{1/2}$$

$$= \left[|I_2|^2\left(\sin^2\phi_2 + \cos^2\phi_2\right) + |I_1|^2 + 2|I_1||I_2|\cos\phi_2\right]^{1/2}$$

$$= \left[|I_1|^2 + |I_2|^2 + 2|I_1||I_2|\cos\phi_2\right]^{1/2}$$

$$= \left[I_{ASE}{}^2 + I^2 + 2I_{ASE}I\cos\phi\right]^{1/2}$$

Our expression equates with their equation (4).

2.5 References

1. Lakowicz, J. R., *Principles of Fluorescence Spectroscopy*. 2 ed.; Kluwer Academic / Plenum Publishers: New York, 1999.

2. Duschinsky, F., Der zeitliche Intensitatsverlauf von intermittierend angeregter Resonanzstrahlung. *Z. Phys.* **1933,** 81, 7.

3. Lakowicz, J. R.; Laczko, G.; Cherek, H.; Gratton, E.; Limkeman, M., Analysis of Fluorescence Decay Kinetics from Variable-Frequency Phase-Shift and Modulation Data. *Biophysical Journal* **1984,** 46, (4), 463-477.

4. Verveer, P. J.; Squire, A.; Bastiaens, P. I. H., Global analysis of fluorescence lifetime imaging microscopy data. *Biophysical Journal* **2000,** 78, (4), 2127-2137.

5. van Helden, J. H.; Schram, D. C.; Engeln, R., Phase-shift cavity ring-down spectroscopy to determine absolute line intensities. *Chemical Physics Letters* **2004,** 400, (4-6), 320-325.

6. Kasyutich, V. L.; Martin, P. A.; Holdsworth, R. J., Effect of broadband amplified spontaneous emission on absorption measurements in phase-shift off-axis cavity enhanced absorption spectroscopy. *Chemical Physics Letters* **2006,** 430, (4-6), 429-434.

7. Lehmann, K. K.; Romanini, D., The superposition principle and cavity ring-down spectroscopy. *Journal of Chemical Physics* **1996,** 105, (23), 10263-10277.

8. Istratov, A. A.; Vyvenko, O. F., Exponential analysis in physical phenomena. *Review of Scientific Instruments* **1999,** 70, (2), 1233-1257.

9. Jakubinek, M.; Tong, Z. G.; Manzhos, S.; Loock, H. P., Configuration of ring-down spectrometers for maximum sensitivity. *Canadian Journal of Chemistry-Revue Canadienne De Chimie* **2004,** 82, (6), 873-879.

10. Gratton, E.; Jameson, D. M.; Hall, R. D., Multifrequency phase and modulation fluorometry. *Annual Review of Biophysics and Bioengineering* **1984,** 13, 105-24.

11. Iwata, T., Proposal for Fourier-transform phase-modulation fluorometer. *Optical Review* **2003,** 10, (1), 31-37.

12. Iwata, T.; Shibata, H.; Araki, T., Construction of a Fourier-transform phase-modulation fluorometer. *Meas. Sci. Technol.* **2005,** 16, 2351-2356.

13. Engeln, R.; vonHelden, G.; Berden, G.; Meijer, G., Phase shift cavity ring down absorption spectroscopy. *Chemical Physics Letters* **1996,** 262, (1-2), 105-109.

14. Model SR844 RF Lock-In Amplifier User's Manual. In Stanford Research Systems: Sunnyvale, California, 2003.

Chapter 3 Methods for reducing optical loss

3.1 Context and motivation

In general, a fibre loop used in ringdown spectroscopy for probing a bulk liquid consists of a discontinuous loop of fibre containing some means of coupling light into and out of the loop. The discontinuity is used as the location to introduce a liquid sample into the light path. Injecting light into and tapping light out of a loop is most easily achieved using commercially available fused fibre evanescent field (FFEF) couplers. Each of these components (input coupler, output coupler, and sample gap) has an insertion loss associated with it. The insertion loss is here defined as the optical loss (in % or dB) that results from the component being present in the loop (and in the case of couplers it does not include the loss associated with coupling). FFEF couplers commonly have an insertion loss of 2 to 4 % each. The insertion loss of the sample gap depends on its configuration and can vary from ~2 to 10 %. Each commercial FFEF coupler includes 2 m fibre pigtails out of which a loop of 4 m or less can be fabricated. Longer loops require a minimum of two splices and each splice has an insertion loss of typically 1 %. The fibre itself has an unavoidable optical loss associated with it, though this contribution (0.005 % / m for SMF-28 at 1550 nm) is usually small in comparison to the loss associated with other components. Thus a fibre loop containing two FFEF couplers, two splices, and a well-configured sample gap has a minimum optical loss of 8 % per pass (T = 0.92). This corresponds to a cavity enhancement, $d_{eff}/d = 1/(1-T)$, of 12.5. For

comparison, the cavity enhancement of a perfect loop of SMF-28 ($T = 0.99995$) is 20 000. From this example it is obvious that in order to exploit the main advantage of ringdown spectroscopy, i.e. a greatly enhanced pathlength through the sample, it is necessary to reduce the insertion loss of the components contained in the loop to a minimum. This chapter focuses on two approaches to this – the design of a low loss coupler, and the use of microlenses to reduce loss associated with the sample gap.

3.2 Couplers

Various coupler types are commercially available. For comparison to the coupler designs investigated below, we will briefly mention two broadband coupler types – fused fibre evanescent field (FFEF) couplers and field access block (FAB) couplers.

FFEF couplers are inexpensive and commonly used. They are available with fixed split ratios between 0.5 and 50 %, but as mentioned previously have an insertion loss of 2 – 4 %. Two fibres are twisted around each other over a short length (< 1 cm) and melted (fused) together so that their fibre cores are close together. The evanescent field of the input fibre core overlaps with the evanescent field of the output fibre core and coupling occurs. The distance between cores and the interaction length determines the coupling ratio.

The performance of field access block couplers also depends on the overlap of the evanescent waves of the input and output fibres. The evanescent field of a core mode is "accessed" by precisely polishing away part of the cladding so the fibre is D-shaped in

cross-section. When two such D-shaped fibres are positioned face to face, coupling can occur (Figure 3.1). FAB couplers have similar fixed split ratios but with lower insertion loss (~ 1 %) compared to FFEF couplers. The lower insertion loss is accompanied by a considerably increased price.

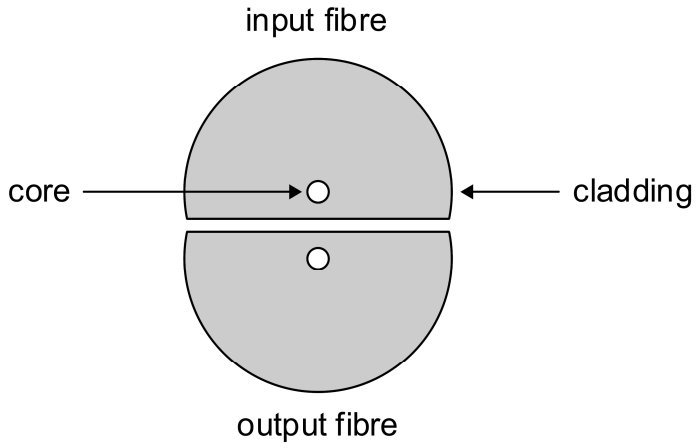

Figure 3.1: Schematic of an FAB coupler in cross-section.

A short portion of a fibre is polished into a D-shape to access the evanescent field. Placing two D-shaped fibres in optical contact allows evanescent coupling between the cores.

It should be noted that in both of these designs light is coupled equally in both directions. In the context of a fibre loop, this means that if 50 % of the light in the input fibre is coupled into the loop then 50 % of the light already in the loop will be coupled out. Since we desire the light to be resonant in the loop for as long as possible (i.e. have a long ringdown time) the coupling ratio must be low, preferably 1 % or less.

To address insertion loss and price while offering a variable coupling ratio, we investigated two coupler designs – grating-assisted couplers and cladding mode injection couplers.

3.2.1 Grating-assisted coupler

Grating-assisted couplers have previously been used to couple light between fibre waveguides with the intended application of being add-drop filters in telecommunications.[1-3] We investigated their feasibility for use in coupling between fibre waveguides for injection and tapping of light in and out of fibre loops.

The grating-assisted couplers we constructed consist of two long-period gratings (LPGs), one in each waveguide. An LPG is an optical element which consists of a periodic modulation of the fibre core refractive index, $\delta n \simeq 10^{-4}$, over a length L of 2 – 3 cm. The LPG can couple light from a core mode (e.g. LP_{01}) to a cladding mode (LP_{0m}, m = 3, 5, 7, …) or vice versa, with the extent of coupling characterized by the coupling coefficient κ. This coupling occurs at specific wavelengths of light, λ_o, where the phase matching condition is met, and is given by

$$\lambda_o = \left(n_{01}(\lambda) - n_{0m}(\lambda)\right)\Lambda \qquad (1.1)$$

where n_{01} is the effective refractive index of the core mode LP_{01}, n_{0m} is the effective refractive index of the cladding mode LP_{0m}, and Λ is the pitch (or period) of the change in refractive index that forms grating.[1] The coupling coefficient κ depends on δn, λ_o, and the spatial overlap of the LP_{01} and LP_{0m} modes such that,[1]

$$\kappa = \frac{\pi \delta n I}{\lambda_o} \qquad (1.2)$$

where

$$I = \frac{\int_0^{2\pi}\int_0^{r} \psi_{01}\psi_{0m} r dr d\theta}{\left(\int_0^{2\pi}\int_0^{\infty} \psi_{01}^2 r dr d\theta\right)^{1/2}\left(\int_0^{2\pi}\int_0^{\infty} \psi_{0m}^2 r dr d\theta\right)^{1/2}} \tag{1.3}$$

The insertion loss of an LPG is < 0.2 dB.[4] Light is redistributed between the core and cladding with a small amount lost to scattering and back-reflection.

To construct a grating-assisted coupler (GAC), the lengths of fibre in which the gratings occur are overlapped and the claddings are held in contact. This is shown schematically in Figure 3.2. Light couples between the claddings of the two fibres via the evanescent wave (see Chapter 1.3), with the extent of evanescent coupling characterized by the coupling coefficient *C*. *C* is related to the spatial overlap of the LP_{0m} cladding modes, and is approximately expressed as[1]

$$C = \frac{\sqrt{2\Delta}}{\rho}\frac{U^2}{V^3}\frac{K_0\left[W\left(2+\frac{d}{\rho}\right)\right]}{K_1^2(W)} \tag{1.4}$$

where K_0 and K_1 are modified Bessel functions, Δ is the relative index difference between the cladding and external medium ($(n_2^2-n_3^2)/(2n_2^2)$), *d* is the distance between the fibres which was here kept as zero, and ρ is the fibre's outer radius. *U*, *V*, and *W* are normalized parameters where $U = (2\pi\rho/\lambda)\left(n_2^2 - n_{0m}^2\right)^{1/2}$, $V = (2\pi\rho/\lambda)\left(n_2^2 - n_3^2\right)^{1/2}$, and $W = (2\pi\rho/\lambda)\left(n_{0m}^2 - n_3^2\right)^{1/2}$.

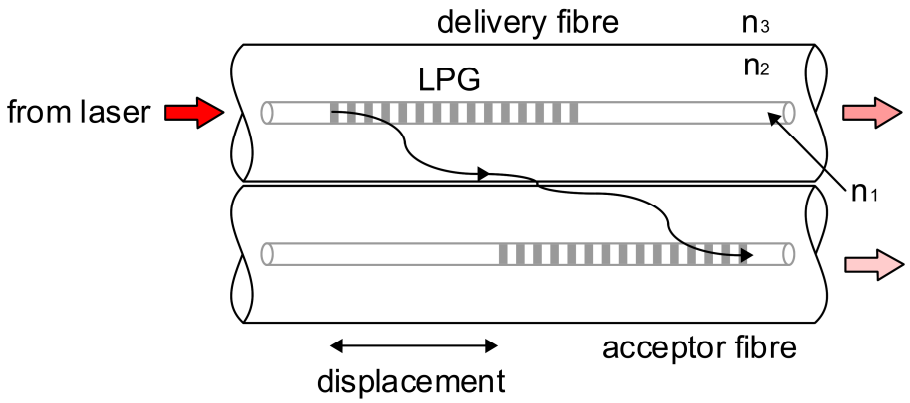

Figure 3.2: Grating-assisted coupler.

Light is coupled from the core to a cladding mode of the delivery fibre via the long-period grating (LPG). This is followed by evanescent coupling between the cladding modes of the delivery and acceptor fibres. Finally, the light is coupled from the cladding to the core within the acceptor via another LPG.

Two LPGs in SMF-28 with identical centre wavelengths (1582 nm) provided by Avensys were used to create the GAC. The LPG of the delivery fibre was chosen to have a higher loss (18 dB) than that of the acceptor fibre (13 dB) to make available as much light as possible for coupling into the acceptor. A high-loss (i.e. large κ) acceptor fibre LPG was used in this initial test to ensure a large signal amplitude for easy detection; in a real application a loss of < 1 dB would likely be desirable. A system of channels in an aluminum slab were specially designed for the purpose of ensuring contact between the claddings of the two fibres (i.e. $d = 0$) whilst allowing the extent of overlap between the LPGs to be varied. This is pictured in Figure 3.3.

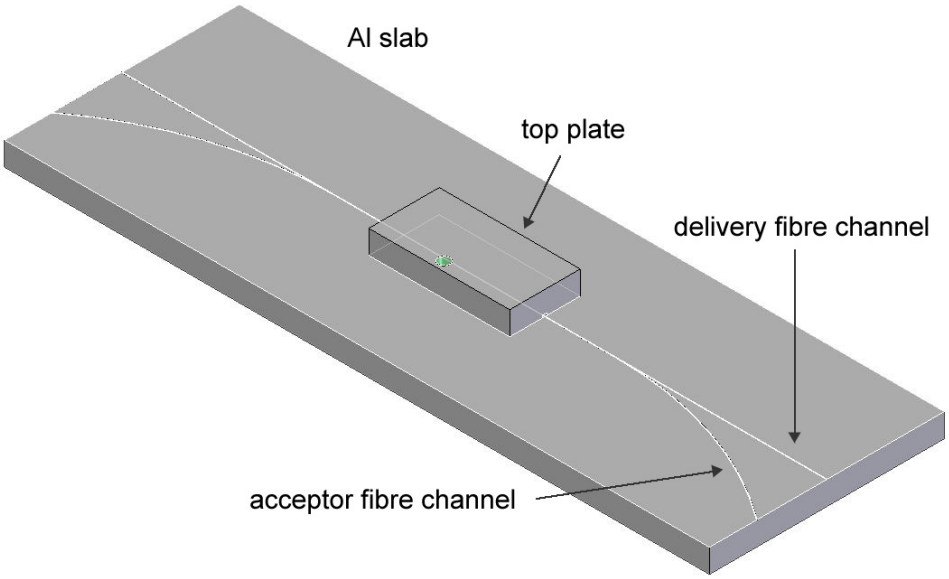

Figure 3.3: Schematic of the Al slab used for constructing the grating-assisted coupler.

The static LPG (acceptor fibre) is affixed where it passes through the curved channels, while the other LPG (delivery fibre) is made movable in precise and measurable quantities by fastening it to a 1D translation stage beyond the Al slab. The channels are rectangular, with dimensions 125 x 250 μm (depth x width) in order to accommodate two SMF-28 fibres stripped of their coating. A hinged aluminum top plate coated with PDMS served to hold the fibers in place where the LPGs overlap.

The light source used was an Ando AQ4320D laser at 1582.000 nm intensity modulated at 270 Hz. Two InGaAs photodetectors (Thorlabs DET410, Thorlabs D400FC) and a Tektronix TDS 3032 oscilloscope were used to detect and measure the voltage of the signal at the output of the delivery and acceptor fibres.

In the experiment, the delivery fibre was translated past the acceptor fibre in 100 μm increments. At each increment the output voltage amplitude in both fibres was

measured. The overall coupling ratio, $\eta = \left(V_{acceptor} / V_{delivery}\right)$ x 100%, is shown in Figure 3.4.

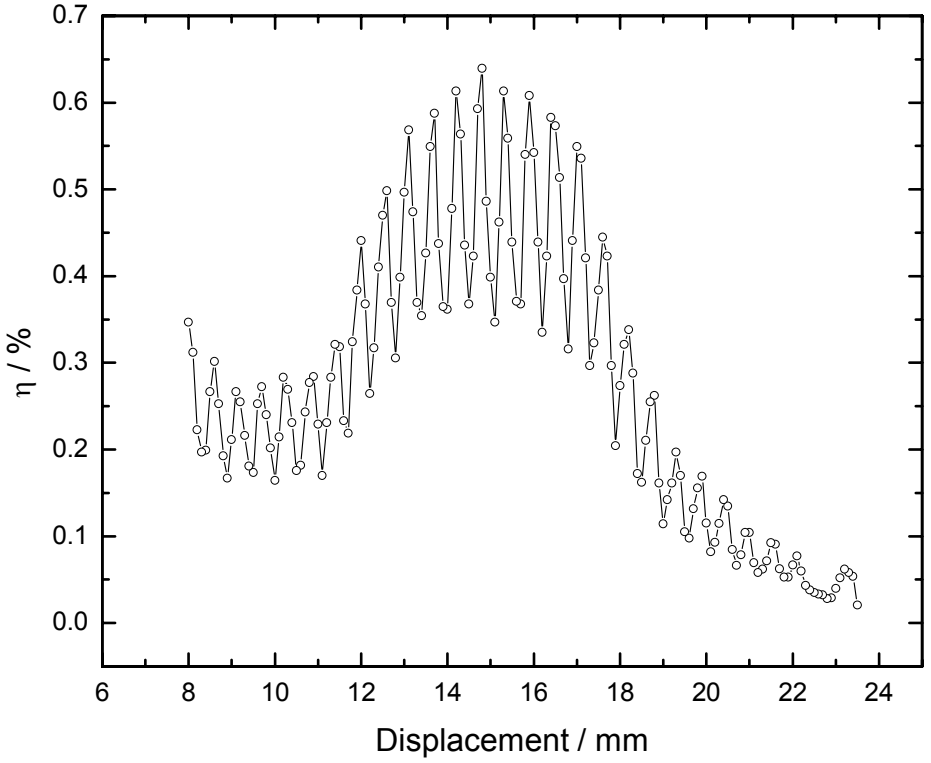

Figure 3.4: Overall coupling ratio for the grating-assisted coupler (GAC) as a function of delivery fibre displacement. The solid line was added to make obvious the oscillation of period 569 μm.

A maximum η of 0.64 % was achieved with the GAC. The variable coupling with respect to displacement evident in Figure 3.4 is periodic in nature. The short oscillation period (569 μm, from the Fourier transform of Figure 3.4) matches the pitch of the gratings (570 μm), while the long period is related to coupling of light back and forth between gratings over their overlap. A detailed description and analysis of this behaviour is beyond the scope of this thesis and the reader is referred to the paper of Chiang et al. for more information.[1] The core/cladding mode coupling coefficient κ (corresponding to

18 and 13 dB) must be quite high, while the overall coupling η was observed to be small. This implies that the evanescent coupling coefficient C was quite low. C could be improved by placing an index-matching medium around the fibres, however the refractive index of this medium must be below that of the cladding lest the cladding modes become so weakly guided that no evanescent coupling occurs.[1] A GAC consisting of a high-loss delivery fibre (> 15 dB), low-loss acceptor fibre (< 1 dB), and an appropriate index-matching medium to increase C could lead to a suitable coupler for use in a fibre loop.

Grating-assisted couplers were not pursued any further as a means of coupling light into and out of fibre loops for the following reasons: the coupler requires lengthy characterization to determine the overlap at which the desired coupling ratio occurs; the resonant wavelength is temperature dependent limiting its practicality for field use, and; the coupling is inherently restricted to a small range of wavelengths. For performing spectroscopy, especially on the liquid phase where spectral features are broad, it is desirable to have access to a larger range of wavelengths than an LPG-based grating-assisted coupler can afford. Thus, we next investigated a novel broadband coupling method.

3.2.2 Cladding mode injection coupler

Given the deficiencies of a grating-assisted coupler, we set out to design a coupler that operated in a similar manner but with no wavelength or temperature dependence.

Two changes were made to the construction of the GAC presented above – no gratings were included and the fibre type was changed from single mode to multimode. To account for the fact that there was no longer an optical element such as an LPG to facilitate coupling between core and cladding modes, we purposefully excited cladding modes in the delivery fibre. The cladding modes of the delivery fibre can then couple to the cladding modes of the acceptor fibre, and then gradually equilibrate with the core modes of the acceptor fibre. This is shown schematically in Figure 3.5. Coupling from the acceptor cladding to core depends on the fact that out of the hundreds of supported cladding modes and ~ 600 core modes,[5] some must overlap and result in a transfer of light, though κ here should be small. (Here we still use κ to denote cladding to core coupling, however it is no longer given by equation (1.2)). This coupler should exhibit zero insertion loss since the geometry and refractive index of the fibre are left completely unchanged.

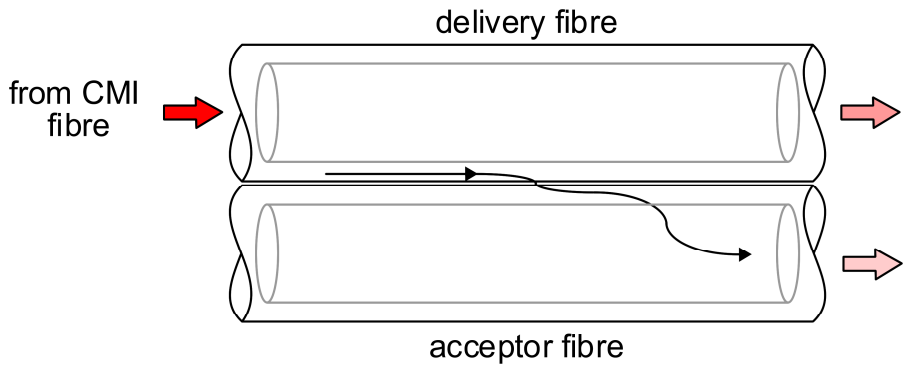

Figure 3.5: Schematic of the CMI coupler.

Light is coupled from cladding modes of the delivery fibre to cladding modes of the acceptor fibre, followed by coupling from cladding to core modes within the acceptor fibre.

The coupler apparatus was identical to the one used for the GAC save for the change in fibre type from single mode to multimode and the exclusion of the 1D translation stage since it was no longer necessary. An important addition to the overall apparatus was a means to excite cladding modes in the delivery fibre. This was achieved by what we term a cladding mode injection (CMI) fibre. The CMI fibre is separate from the delivery fibre and guides light from the laser to the delivery fibre. The flat-cut ends of the two fibres are separated longitudinally by a small amount, and most importantly are offset laterally (Figure 3.6). The purpose of the lateral offset is to have a large intensity of light from the CMI fibre incident on the cladding of the delivery fibre so as to excite cladding modes within it. Control and measurement of the longitudinal and lateral offsets were accomplished by means of the positioning and image analysis functions of a Fitel S182A fusion splicer.

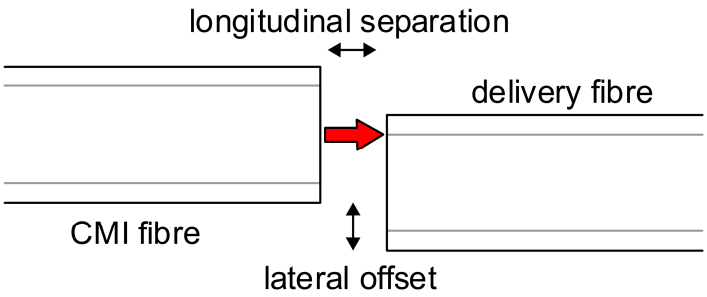

Figure 3.6: Illustration of lateral offset between CMI and delivery fibre.

The lateral offset allows for excitation of cladding modes in delivery fibre.

The signal intensities at the delivery and acceptor fibre outputs were measured as a function of lateral offset between the CMI and delivery fibre. These results are shown in Figure 3.7.

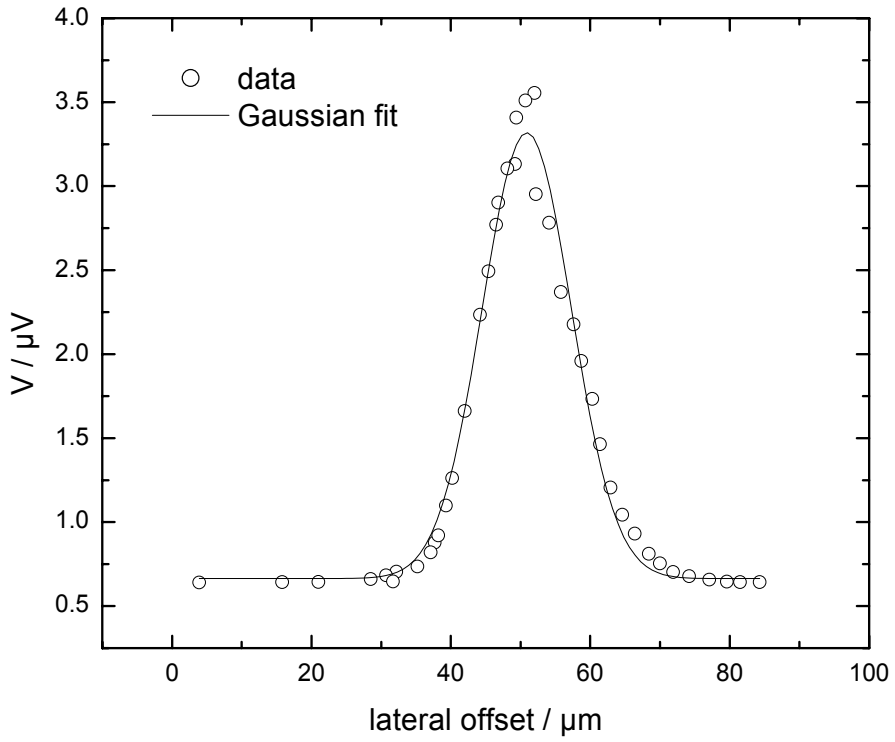

Figure 3.7: Acceptor fibre intensity as a function of lateral offset for the CMI coupler.

A maximum coupling of 0.05 % was achieved at an offset of 50.9 ± 0.1 µm. This corresponds to the centre of the CMI fibre being aligned with the core/cladding boundary of the delivery fibre. The coupling follows a Gaussian trend with offset and can be roughly modeled by the overlap integral of the Gaussian mode field distribution (MFD) of the CMI fibre with the cladding of the delivery fibre. The model predicts a maximum coupling at and offset 58 µm. This value is close to the experimental value, however there is some disagreement. The disparity is likely due to a number of factors: the model does not account for the MFD of the delivery fibre, the numerical aperture of the CMI fibre, nor the longitudinal separation between the CMI and delivery fibres.

An important feature that differentiates the CMI coupler from GAC, FFEF, and FAB couplers is that it is a "one-way" coupler. Recall that for the GAC, FFEF, and FAB designs if 1 % of the light in the delivery fibre is coupled into the acceptor fibre (the forward direction), then 1 % of the light in the acceptor fibre must be coupled out to the delivery fibre (the reverse direction) – in this respect the couplers are "two-way". The CMI coupler uses purposeful excitation of cladding modes in the delivery and acceptor fibres to facilitate coupling. Cladding modes are lossy – over many metres they will be either coupled to core modes, lost to the coating, absorbed, or scattered. Thus using a long enough loop, the cladding modes will be completely attenuated by the time they return to the position of the CMI coupler. Since spatial overlap between core modes of the loop fibre and cladding modes of the delivery fibre is very small, almost no light will couple in this reverse direction. This fact is what defines the CMI coupler effectively as a "one-way" coupler. This was tested by directly exciting core modes of the acceptor fibre with the laser and measuring the coupling ratio at the output. It was found to be < 0.0005 %. However, the presence of a sample gap counteracts this useful one-way property – when light traverses the gap it is coupled to both core and cladding modes in the receiving end.

In a separate experiment the extent of cladding to core coupling in the acceptor fibre was qualitatively determined. Cladding mode injection was used to couple light from a multimode delivery fibre to a single mode acceptor fibre which was part of a fibre Bragg grating (FBG) cavity (see Chapter 4) ~ 80 m in length (Figure 3.8).

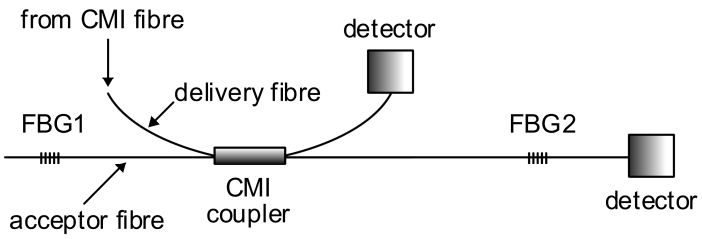

Figure 3.8: CMI coupler used in conjunction with a fibre Bragg grating (FBG) cavity to test the extent of cladding to core mode coupling in the acceptor fibre.

FBGs act like mirrors over a narrow range of wavelengths near their Bragg resonance. At the Bragg resonance they will only reflect the core mode (LP_{01}) and will allow any cladding modes to pass. Thus by tuning the laser to the Bragg resonance of the cavity, the core mode is "trapped" inside and any light detected outside the cavity should be due to cladding modes. The extent of cladding to core coupling should then be related to the intensity of light measured at the detector with the laser tuned to the Bragg resonance and away from it. This value could not be quantified since the intensity at the detector actually consists of cladding modes, the attenuated core mode, and broadband amplified spontaneous emission (ASE) from the laser (see Chapter 4). When the experiment was performed the intensity on resonance was greatly attenuated compared to the intensity off resonance. Therefore coupling from cladding to core in the acceptor fibre occurs to large extent given a long enough length of fibre is used (i.e. κ is small). C may also be concluded to be small since the maximum η was 0.05 % and air surrounded the fibres (n = 1). As with the GAC, C could be increased by choosing a suitable index-matching medium.

Though it was not determined directly, the result of the last experiment implies that the CMI coupler is broadband. Light was coupled to the acceptor fibre both on and off the Bragg resonance. The CMI coupler consists of nothing other than optical fibre, which itself is broadband. Therefore there is naught to suggest that the CMI coupler is not broadband in a manner similar to FFEF and FAB couplers (i.e. limited only by the transmission spectrum of the fibre and the penetration depth of the evanescent field).

The cladding mode injection coupler realizes the goal of designing a variable coupler that is broadband and has no temperature dependence in the manner of a grating-assisted coupler. The forward coupling ratio can be varied between 0 and 0.05 % by altering the offset of the CMI fibre. The reverse coupling ratio is < 0.0005 % and effectively makes the coupler one-way. Despite these favourable characteristics, the pursuit of a broadband low insertion loss coupler based on cladding mode injection was discontinued in light of other experiments which indicated that the presence of any cladding modes at all in a fibre loop increases the difficulty of extracting the ringdown time from the phase shift (cf. Chapter 2). Taking this fact into consideration, intentionally introducing cladding modes into the loop seemed counter-productive.

3.3 Lenses

The transmission of light across a sample gap decreases exponentially with gap length when using flat-cut fibre facets (see equation (1.18) below). The transmission

drops to 0.9 at a fibre separation of 4.6 μm for SMF and 27 μm for MMF. SMF (core diameter 8.4 μm) is more amenable to use in microfluidic chips, where the channels are commonly 20 x 20 μm (width x depth), than MMF (core diameter 100 μm). However, at a fibre separation of 20 μm the transmission for SMF is predicted to be only 0.65. Clearly some means must be found to increase the transmission across gaps comparable in size to the core diameter if SMF is to be used in conjunction with microfluidic systems. The solution proposed here is the use of two confocal micro-lenses formed directly from the fibre material itself.

Hemispherical microlenses were fabricated by exposing a flat-cleaved fibre end to multiple electrical arcs.[6] The melted glass is pulled by surface tension into a hemispherical shape. The process was performed and monitored on a fusion splicer (Fitel S182A). The fibre end was aligned with the centre of the arc and the arc discharged repeatedly until a suitable shape was created. Lenses were made from 8.4/125 SMF and 100/140 MMF. FC connectors were added to connect to a laser (Ando AQ4320D) and detector (Thorlabs D400FC). Matching lenses were placed in a translation stage (Thorlabs MBT616) and the transmission recorded with a Tektronix TDS 3032 oscilloscope while varying the axial and transverse displacement. The radius of curvature of the lenses was approximated from microscope images.

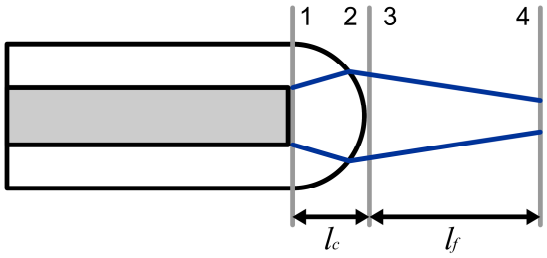

Figure 3.9: Fibre lens showing the regions used in the ray matrix transformation.

Region 12 is the beam-expanding region of length l_c. Region 23 is the lens-air interface. Region 34 is the air region of length l_f.

The ray matrix transformation was used to model the effect of the fiber lenses on transmission efficiency.[7] The ray matrix contains elements A, B, C, D which relate the ray parameters of the input and output planes. The matrix M_{ij} describes the transformation of the ray parameters between planes i and j. M_{12} represents the beam-expanding region of length l_c, M_{23} the lens-air interface, and M_{34} the air region (Figure 3.9).

$$\begin{pmatrix} A & B \\ C & D \end{pmatrix} = M_{34}M_{23}M_{12} \tag{1.5}$$

$$M_{12} = \begin{pmatrix} 1 & l_c \\ 0 & 1 \end{pmatrix} \tag{1.6}$$

$$M_{23} = \begin{pmatrix} 1 & 0 \\ \dfrac{n_2 - n_1}{n_2 R} & \dfrac{n_1}{n_2} \end{pmatrix} \tag{1.7}$$

$$M_{34} = \begin{pmatrix} 1 & l_f \\ 0 & 1 \end{pmatrix} \tag{1.8}$$

In (1.7) n_1 is the refractive index of the lens, n_2 that of air, and R the radius of curvature of the fibre lens. Utilizing the fact that the radius of curvature of the beam goes to infinity at the focal length, one may write

$$AC + b^2 BD = 0 \tag{1.9}$$

where

$$b = \frac{\lambda}{\pi w_0^2 n_1} \tag{1.10}$$

Solving (1.9) for l_f yields the focal length. The initial beam waist size, w_0, is approximated as the mode field radius, given by the manufacturer as being 5 μm for SMF and 56 μm for MMF. The waist size at the focal length, l_f, is

$$w_{01} = w_0 \left[\left(\frac{n_1}{n_2} \right) \frac{A^2 + a^2 B^2}{AD - BD} \right]^{1/2} \tag{1.11}$$

The beam radius at axial distance z is

$$w_1(z) = w_{01} \left[1 + \left(\frac{(z - l_f)\lambda}{\pi n_2 w_{01}^2} \right)^2 \right]^{1/2} \tag{1.12}$$

The radius of curvature of the beam at z is

$$R_1(z) = (z - l_f) \left[1 + \left(\frac{\pi n_2 w_{01}^2}{\lambda (z - l_f)} \right)^2 \right] \tag{1.13}$$

The coupling efficiency between two lenses is expressed as

$$\eta = \frac{\eta_0}{\sqrt{1+\gamma}} \exp \left[-\frac{x^2}{w_{02}^2} \left(\frac{\frac{w_{02}\eta_0}{w_1(z)} + 2\gamma}{1+\gamma} \right) \right] \tag{1.14}$$

where x is the transverse displacement,

$$\eta_0 = \frac{2 w_1(z) w_{02}}{w_1^2(z) + w_{02}} \tag{1.15}$$

and

$$\gamma = \left(\frac{\pi n_2 w_1(z) w_{02} \eta_0}{2\lambda R_1(z)} \right)^2 \tag{1.16}$$

Here we assume the two lenses to be identical so that $w_{02} = w_{01}$ (i.e. the waist size at the focal length for both lenses is the same). The beam volume at a total axial separation of l is given by

$$V_{beam} = \int_0^l \pi w_1^2(z)\, dz \tag{1.17}$$

The coupling efficiency for two flat-cut fibres, η_{FC} can also be expressed mathematically and is provided for comparison to the lensed results.[5] A cylindrically symmetric Gaussian intensity distribution is assumed. The width of the beam expands as determined by the numerical aperture (NA) of the fibre and the refractive index (n) of the medium between the fibre ends. The coupling is estimated as the overlap of the final beam with the initial beam, scaled by an intensity factor that decreases with increasing axial separation. The coupling efficiency is

$$\eta_{FC} = \frac{\int_0^{2\pi}\int_0^a \exp\left(-\frac{r^2}{2w_2^2}\right) r\, dr\, d\theta}{\left(1+\frac{zNA}{an}\right)^2 \int_0^{2\pi}\int_0^a \exp\left(-\frac{r^2}{2w_0^2}\right) r\, dr\, d\theta} \tag{1.18}$$

where the beam width at the receiving fibre (w_2) is given by

$$w_2 = w_0\left(1+\frac{zNA}{an}\right) \tag{1.19}$$

and a is the fibre core radius.

Table 3.1: Parameters for SMF and MMF lenses.

	SMF	MMF
n_1 †	1.4682	1.457
a / μm †	4.2	50
R / μm ‡	63	74
w_0 / μm †	5	56
l_f / μm ‡	4	65
$V_{beam}(2l_f)$ / L	7.3×10^{-13} [a]	1.2×10^{-10} [b]

† Manufacturer's specifications. ‡ Experimentally determined. [a] Calculated from modeled value of w_{01}. [b] Calculated from experimental value for w_{01}.

The coupling efficiency was measured for two SMF fibre lenses at 5 mW of 1550 nm light as a function of axial separation (Figure 3.10). The coupling efficiency was scaled to unity for the maximum efficiency recorded. Referencing against a continuous piece of fibre yields a scaled efficiency of 0.98. To fit the model to the data for the SMF lenses the length of the beam expanding region was adjusted, resulting in l_c = 26 μm. Melting during lens formation likely alters the core geometry at the lens tip, so including a beam expanding region can be thought to be valid. The model assumes that the transverse offset is zero at all axial separations. Deviations from the model at larger axial separation are possibly due to a slight transverse offset (on the order of a few μm) of the fibers that occurred during the experiment. Cross-talk between translation stage axes could easily cause a deviation of this magnitude. Aberrations in the lens due to mixing of core and cladding glasses during melting might also contribute to this disagreement. Most likely the difference results from the lenses not being identical, as the model assumes. The lens and beam parameters are summarized in Table 3.1. It was found a

Gaussian function fits the experimental data quite well; however the only parameter such a fit yields is the focal length. One can see from Figure 3.10 that the lenses provide a large enhancement in efficiency over flat-cut fibers at all axial separations except those under about 1 μm.

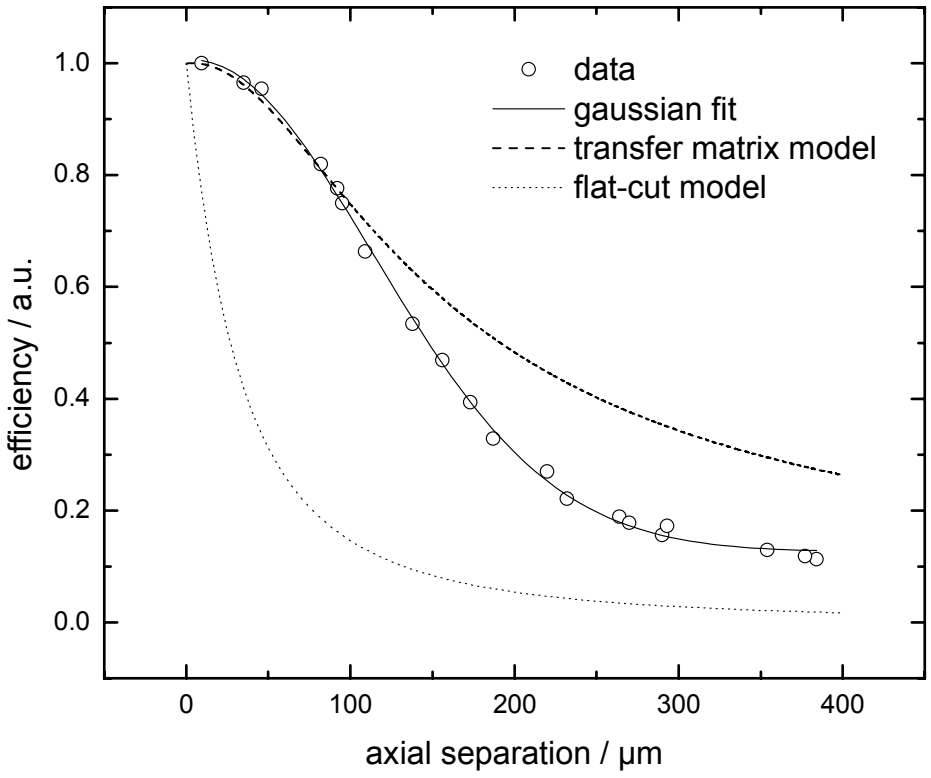

Figure 3.10: Efficiency as a function of axial separation for two SMF lenses.

Simulation using the transfer matrix model with no beam-expanding region (l_c = 0 μm) and water as the medium yields a focal length of 7.3 μm, which is well matched with the channel dimensions of a microfluidic chip (ideal focal length is 10 μm). These experimental and simulated results suggest microlenses present a very good means of reducing optical loss at the sample gap.

The coupling efficiency for two MMF lenses was measured in the same manner described above and is plotted in Figure 3.11. The efficiency for the transfer matrix model and the flat-cut case are also plotted. One immediately notes the large discrepancy between the experimental data and the transfer matrix model (TMM). This arises because the beam is assumed to arrive parallel to the axis of the fibre in a single mode that experiences a single effective core refractive index. In reality the multimode fibre carries approximately 600 modes[5] each experiencing a different n_{eff} and exiting the fibre at a different angle. The experimental data thus represents a sum of the coupling efficiency of each of the modes, each with their own beam parameters. The TMM result presented can be thought of as an approximation to the coupling efficiency only for the LP_{01} mode. A full treatment, not given here, would require the determination of the beam parameters and relative intensities of all modes so a weighted sum could be performed. The entrance (θ_1) and exit angle (θ_2) through the lens for each mode can be taken into account by using a more general form of the TMM[8]

$$\begin{pmatrix} A & B \\ C & D \end{pmatrix} = \begin{pmatrix} 1 & lf \\ 0 & 1 \end{pmatrix} \begin{pmatrix} 1 & 0 \\ 0 & \frac{n_1}{n_2} \end{pmatrix} \begin{pmatrix} \frac{\cos\theta_2}{\cos\theta_1} & 0 \\ \frac{n_2\cos\theta_2 - n_1\cos\theta_1}{R\cos\theta_1\cos\theta_2} & \frac{\cos\theta_1}{\cos\theta_2} \end{pmatrix} \begin{pmatrix} 1 & lc \\ 0 & 1 \end{pmatrix} \qquad (1.20)$$

A Gaussian fit to the data yields a focal length of 65 μm. The beam volume in Table 3.1 was approximated by using experimentally determined values for l_f and the Gaussian width of the beam at l_f, w_{01} = 33 μm. If equation (1.12) is assumed to be valid then the beam volume from (1.17) is 1.2 x 10^{-10} L. Other lens parameters for MMF are

listed in Table 3.1. The maximum efficiency referenced against a patch cable was 0.97. As with the SMF lenses, the MMF lenses provide a large improvement in coupling efficiency at all axial separations except those below 10 μm.

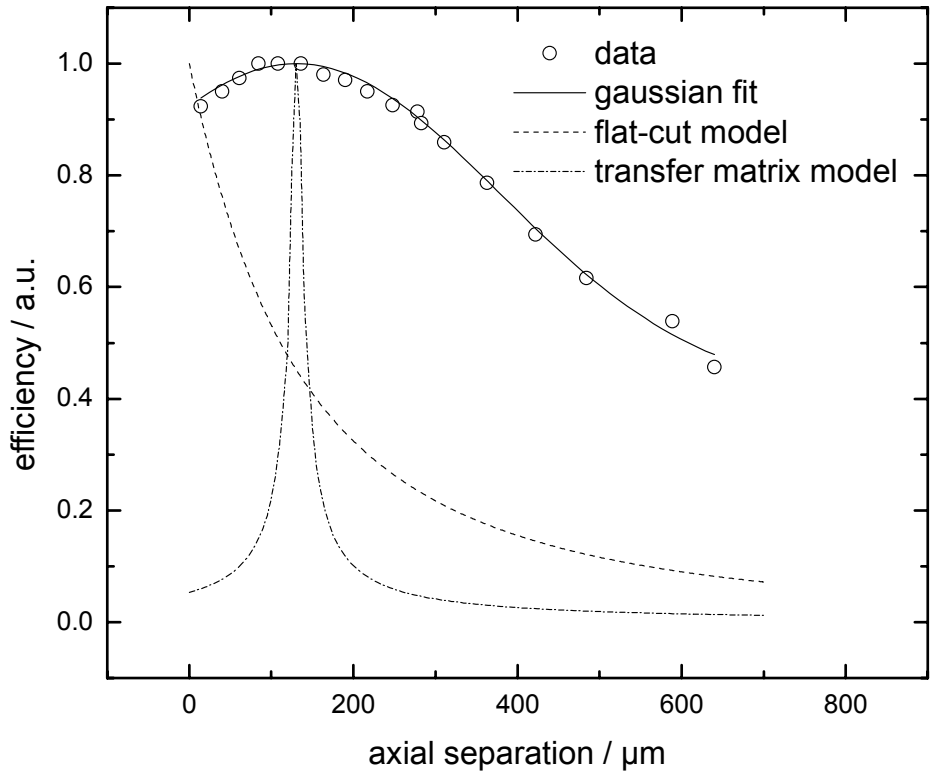

Figure 3.11: Efficiency as a function of axial separation for two MMF lenses.

The coupling efficiency of the same two MMF lenses was tested while submerged in water to gauge their performance in the setting in which they would be used. The efficiency data in Figure 3.12 no longer follow a Gaussian curve but vary linearly over the axial separation range scanned. It is not known why this is the case. Again the lenses afford an increase in efficiency over the flat-cut transmission, which was modeled assuming a refractive index of 1.33 for water.

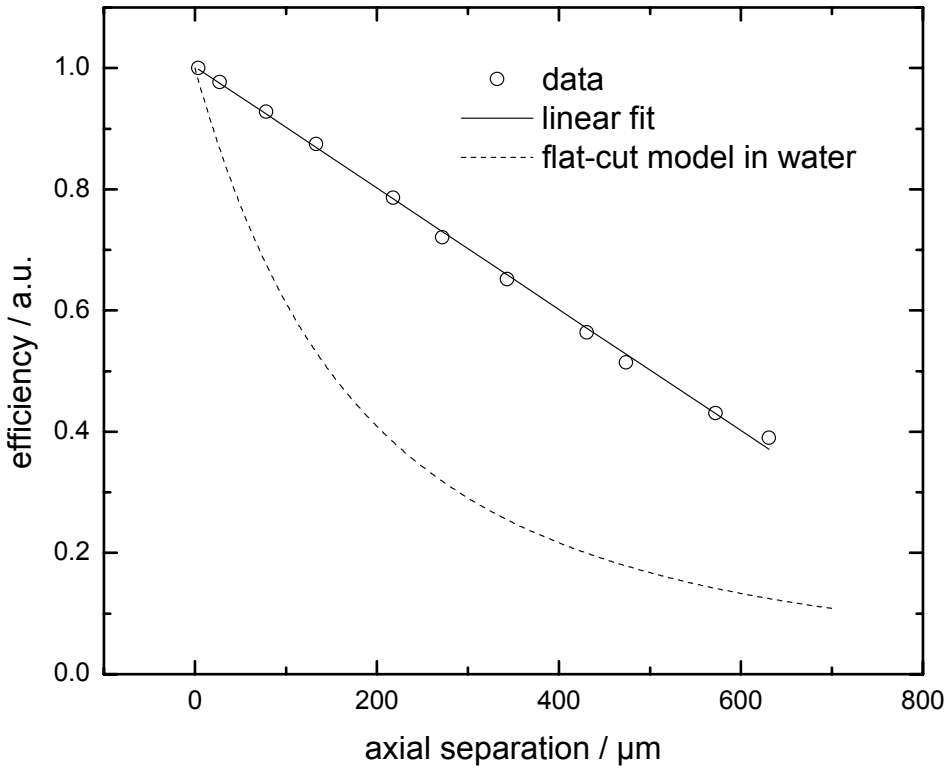

Figure 3.12: Efficiency as a function of axial separation for two MMF lenses in water.

In the later experiments (Chapter 6) one lensed and one flat-cut fibre were used in a sample interface. This scheme can only be used in a loop where the light travels in one direction through the gap. No model has been devised to predict the efficiency of this scheme, however one can predict that the maximum coupling efficiency should likely occur at an axial separation of l_f.

3.4 Conclusion

Two coupling methods for reducing optical loss in fibre loops were investigated – grating-assisted coupling and cladding mode injection coupling. They exhibit a maximum coupling of 0.64 % and 0.05 %, respectively. Due to numerous drawbacks

associated with these methods, neither was adopted for use in fibre loop ringdown spectroscopy. Commercial FAB couplers with their low insertion loss, broadband transmission, and high price are likely the best choice of coupling method for use in FLRDS.

The majority of optical loss in a fibre loop occurs at the sample gap. We addressed this by incorporating microlenses into the fibre itself. A means of fabricating the microlenses was developed and the coupling between two such lenses was measured and modeled for SMF and MMF. For all fibres and through all media (air and water) the lenses led to increased coupling across the sample gap compared to flat-cut fibres, except at small axial separations. Given their easy fabrication and reduction of optical loss, with the concomitant enhancement of detection limit,[9] it is advantageous to incorporate microlenses into almost any fibre-based RDS system. However, one note for consideration should be made - microlenses may perturb sample flow to a greater extent than flat-cut fibre ends and thus may lead to band broadening when used in chromatographic or electrophoretic applications.

An alternative to reducing loss by better design of components present in the loop is to compensate for any loss by introducing gain. This option was exercised by Stewart et al. in their implementation of FLRDS as a methane gas sensor which utilized an erbium-doped fibre amplifier in the loop.[10] Future work incorporating FAB couplers, fibre lenses, and amplification within the loop may provide a good balance between loss and gain.

3.5 References

1. Chiang, K. S.; Chan, F. Y. M.; Ng, M. N., Analysis of Two Parallel Long-Period Fiber Gratings. *Journal of Lightwave Technology* **2004,** 22, (5), 1358-1366.

2. Chiang, K. S.; Liu, Y.; Ng, M. N.; Li, S., Coupling between two parallel long-period fiber gratings. *Electronics Letters* **2000,** 36, 1408-1409.

3. Grubsky, V.; Starodubov, D. S.; Feinberg, J., Wavelength-selective coupler and add-drop multiplexer using long-period fiber gratings. *Tech. Dig., Opt. Fiber Commun. Conf.* **2000,** 4, 28-30.

4. Vengsarkar, A. M.; Lemaire, P. J.; Judkins, J. B.; Bhatia, V.; Erdogan, T., Long-period fiber gratings as band-rejection filters. *Journal of Lightwave Technology* **1996,** 14, 58-65.

5. Tong, Z. Fiber-Loop Ring-Down Spectroscopy. Queen's University, Kingston, 2004.

6. Kong, G. J.; Kim, L.; Choi, H. Y.; Im, L. E.; Park, B. H.; Paek, U. C.; Lee, B. H., Lensed photonic crystal fiber obtained by use of an arc discharge. *Optics Letters* **2006,** 31, (7), 894-896.

7. Emkey, W. L.; Jack, C. A., Analysis and Evaluation of Graded-Index Fiber-Lenses. *Journal of Lightwave Technology* **1987,** 5, (9), 1156-1164.

8. Hecht, E.; Zajac, A., *Optics*. Addison-Wesley: London, 1974.

9. Li, R. K.; Loock, H. P.; Oleschuk, R. D., Capillary Electrophoresis Absorption Detection Using Fiber-Loop Ringdown Spectroscopy. *Analytical Chemistry* **2006**.

10. Stewart, G.; Atherton, K.; Yu, H. B.; Culshaw, B., An investigation of an optical fibre amplifier loop for intra-cavity and ring-down cavity loss measurements. *Measurement Science & Technology* **2001,** 12, (7), 843-849.

Chapter 4 Cavity ringdown spectroscopy in optical waveguides

An optical cavity for performing ringdown spectroscopy is commonly formed from two highly reflective mirrors aligned at either end of a sealed chamber. An equivalent cavity can be formed using optical fibre as the cavity medium by depositing reflective coatings on the end-facets of the fibre.[1-3] This requires very careful preparation of the end-facets to ensure high reflectivity and reflection perfectly parallel to the long axis of the fibre. A solution easier to implement than end-facet mirrors is the use of optical elements termed fibre Bragg gratings (FBGs) which act in a manner somewhat analogous to mirrors, i.e. they reflect light incident upon them. Two FBGs in an optical fibre thus form an optical cavity. The specifics of how an FBG operates are discussed in section 4.1.

An FBG cavity has been used by O'Keefe et al. for the purpose of measuring the refractive index of a medium external to a tapered length of fibre via the evanescent field.[4] They injected 10 ns pulses at 1563.6 nm into the cavity through one of the FBGs (end-pumping) and recorded and fit the ringdown event in the time domain. They immersed a field access block inside the cavity into glycerin/water mixtures of varying refractive index and recorded the optical loss. They found a cavity enhancement of ~ 100 for small losses.

This chapter focuses on the development of an FBG cavity that may be used for absorption spectroscopy of a bulk liquid. The entire LP_{01} mode transmitted from a fibre facet is passed through the liquid, in contrast to O'Keefe et al. who allowed only the

evanescent wave to interact with the liquid. In further contrast we introduce light into the cavity not through an FBG but through the side of the cavity via a FFEF coupler. This we term side-pumping. Side-pumping initially was chosen in order to generate higher intracavity intensities than end-pumping can easily afford. (Very high intracavity intensities through end-pumping can be achieved using a short cavity with the laser wavelength resonant with a single longitudinal cavity mode. Recall that meeting the resonant condition requires fine control of either the laser wavelength or the cavity length.) Beyond our initial purpose, the side-pumped scheme allowed for the identification of factors in the experiment that were detracting from the utility of the cavity as a ringdown spectrometer that would likely not be apparent using end-pumping. These factors were broadband amplified spontaneous emission (ASE) from the laser and broadband reflection from fibre facets outside the cavity. In section 4.5 a cavity configuration to minimize these factors was found and a cavity design better suited to RDS is proposed.

Before these detrimental factors were realized, a number of experiments were carried out to characterize the cavity and to test its ability to detect absorbing liquid species. First, the phase angle was recorded as a function of modulation frequency and wavelength for two cavity configurations that differed only by the initial propagation direction of the laser light inside the cavity (4.3). Second, a sample gap was introduced in the cavity and the phase angle and modulation depth were recorded at numerous wavelengths for various

neat liquids (4.4). It was the analysis of the results from these experiments that eventually led to the identification of ASE from the laser.

The experiments performed are presented below in chronological order. A discussion of the results obtained in sections 4.3 and 4.4 in the context of the presence of ASE is given in section 4.5.

4.1 Fibre Bragg gratings

The interaction of light with a fibre Bragg grating may be described by coupled mode theory, which may be used to predict its transmission or reflection properties. A fibre Bragg grating consists of a periodic change in the refractive index of the fibre core. The magnitude of this change is typically on the order of 10^{-4} refractive index units, with a pitch Λ of ~ 2 μm (cf. for an LPG Λ = 570 μm) and a total grating length of 2 to 10 mm. An FBG couples the forward-propagating LP_{01} core mode into the reverse-propagating LP_{01} core mode at a wavelength, λ_B, termed the Bragg resonance. The FBG also couples the forward-propagating LP_{01} core mode into various reverse-propagating cladding modes, LP_{0m}, at wavelengths to the blue of the Bragg resonance. In other words, the FBG acts as a mirror at wavelengths specified by the phase-matching condition,

$$\lambda_B = 2n_{01}\Lambda \tag{4.1}$$

for the Bragg resonance,[5] and,

$$\lambda_i = \left[n_{01}\left(\lambda_i, n_{co}, n_{cl}\right) + n_{0m}\left(\lambda_i, n_{co}, n_{cl}, n_{ext}\right)\right]\Lambda \tag{4.2}$$

for the cladding mode resonances (of radial mode order m),[6] where n_{01} and n_{0m} are the effective refractive indices of the fibre core and cladding modes, and n_{co}, n_{cl}, *and* n_{ext} are the refractive indices of the core, cladding, and external medium, respectively.

In the following, two identical FBGs with a laser tuned to their Bragg resonance are used to form an optical cavity. Figure 4.1 shows the transmission spectrum of an end-pumped FBG cavity. One notes a strong attenuation band due to the Bragg resonance and a number of weaker attenuations due to cladding mode resonances.

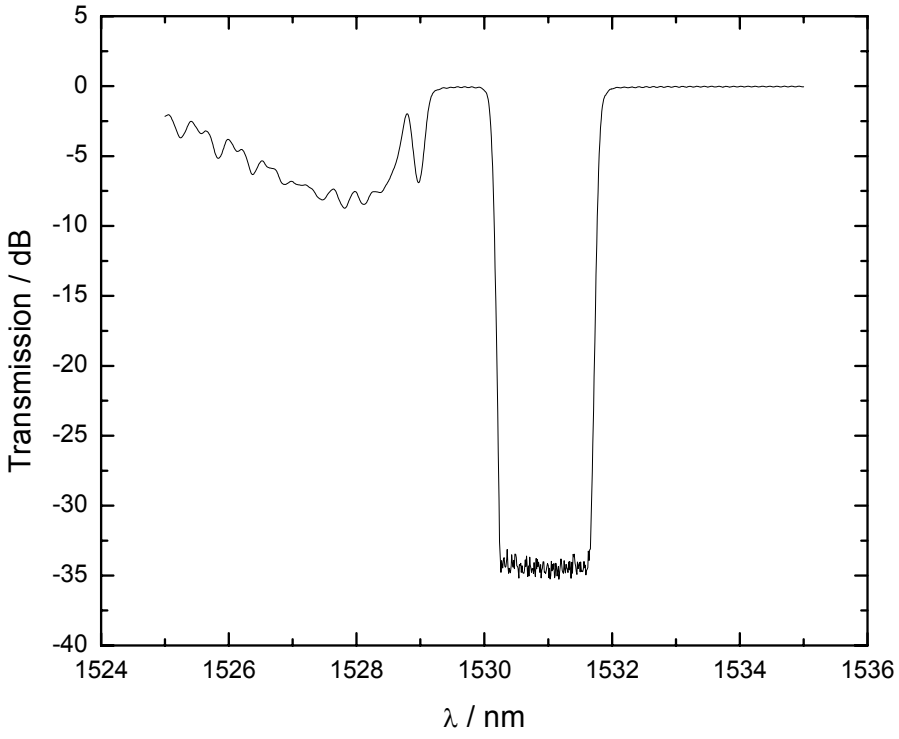

Figure 4.1: FBG cavity transmission spectrum.

The Bragg resonance of both FBGs occurs at 1531 nm, with the cladding modes resonances occurring at shorter wavelengths.

4.2 Apparatus and experiment

The FBGs provided by Avensys (now ITF Labs, Montreal) had a centre wavelength of 1531.0 nm and bandwidth of ~ 2 nm. A fusion splicer (Fitel S182A) was used to create the cavity by splicing together the FBGs, ~74 m of single mode fibre (ThorLabs SMF-28-J9) and a 99:1 coupling ratio 2x2 fused fibre evanescent field (FFEF) coupler (Lightel Technologies Inc.). Cavity spectra were collected with an optical spectrum analyzer (OSA, Agilent 86140B) using a broadband light emitting diode (LED, Exfo FOS-120A) as a light source unless otherwise noted.

When conducting frequency domain experiments a tunable laser (Ando AQ4320D) was sinusoidally current modulated using a LeCroy 9100 arbitrary function generator. The FBG cavity output was detected with an InGaAs photodetector (ThorLabs D400FC) and amplified using a 40 dB gain amplifier from Panametrics-NDT (model 5670DC, 10 MHz bandwidth). All measurements where performed using the same sensitivity scale on the lock-in amplifier (Stanford Research Systems SR844) including the phase angle offset, scaling the laser power if need be. The time constant was set to 300 ms on the lock-in amplifier, and a 24 dB / octave filter was used to suppress any harmonics. The phase and modulation output from the lock-in amplifier is digitized at a 10 Hz sample rate by a National Instruments PCI-6024E DAQ card. The lock-in amplifier is given a 4 s interval to settle at each new frequency before the phase and modulation data is digitized over 6 seconds and averaged. A homewritten program in Visual Basic automates the

instrument control and data collection and processing. Figure 4.2 gives a schematic of the connections between the electronics using in the experiments.

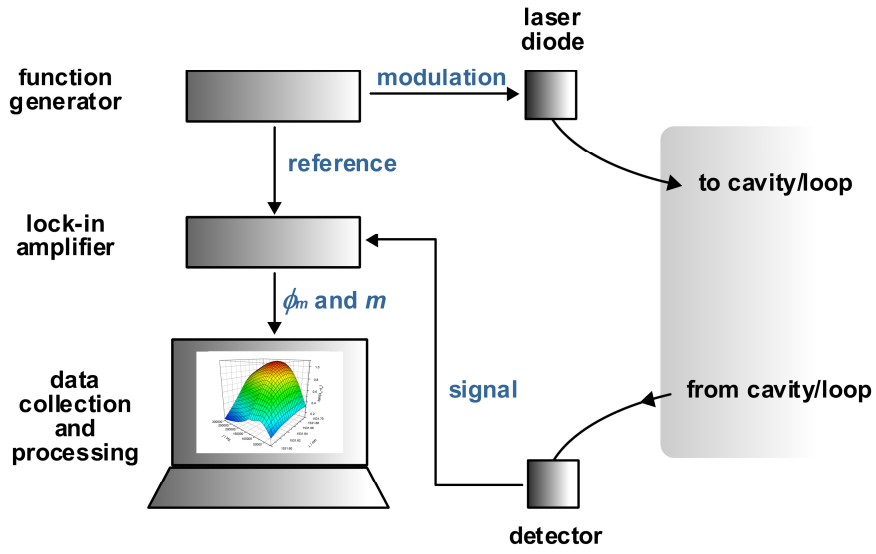

Figure 4.2: General schematic of the electronics used for FD interrogation of a fibre cavity/loop.

Ringdown events were recorded in the time domain on a Tektronix TDS 3032 oscilloscope (500 MHz bandwidth), averaging 512 acquisitions to increase the S/N ratio. The averaged data was transferred to a PC via a GPIB interface. 100 ns pulses at a repetition rate of 1 kHz provided by the function generator were used to drive the laser.

Chemicals were purchased from Sigma-Aldrich and used without further purification. These include dimethylsufloxide (DMSO), benzylamine (or 1-aminomethylbenzene, $C_6H_5CH_2NH_2$, 99%), and *m*-xylylenediamine (1,3-bis(aminomethyl)benzene, $C_6H_4(CH_2NH_2)_2$, 99%).

4.3 Side-Pumped FBG Cavity

Side-pumping of an FBG cavity via a 99:1 coupler allows ~ 30 times more light to enter the cavity compared to end-pumping through a 35 dB FBG. On the other hand, a side-pumped cavity has additional losses over an end-pumped one since the coupler has an insertion loss of about 2 %. The benefits of an easily detectable signal resulting from high intracavity intensity were expected to outweigh the reduction in cavity enhancement due to the presence of the coupler.

Two different side-pumped configurations were characterized. The first configuration tested, denoted **A** (Figure 4.3 **A**), showed the light was following a biexponential decay with time. The ringdown time of the second decay was too short to be representative of light resonant in the cavity. We reasoned that the source of such a short "decay time" must be light that somehow travels directly from the laser to the detector (through FBG2). The identity of this "direct" light was first thought to be cladding modes since they are not reflected by an FBG when tuned to its Bragg resonance. However there was no easily identifiable source of cladding modes within the system. Regardless, we then reasoned that changing the initial propagation direction of the laser light to be opposite than in **A** should deny the non-resonant "direct" light any possibility of reaching the detector. This second configuration, with different initial propagation direction, we denote **B** (Figure 4.3 **B**). Later we determined that the source of this "direct" light was broadband ASE from the laser (see 4.5).

The phase angle offset (ϕ_o, see Chapter 2.2.4) for **A** can easily be obtained by tuning the laser to the red of the Bragg resonance of the cavity and scanning the laser modulation frequency. The phase offset for **B** can be obtained by splicing another FBG (FBG3), with a Bragg resonance well to the red of those forming the cavity, opposite of the detector and tuning the laser to its resonant wavelength.

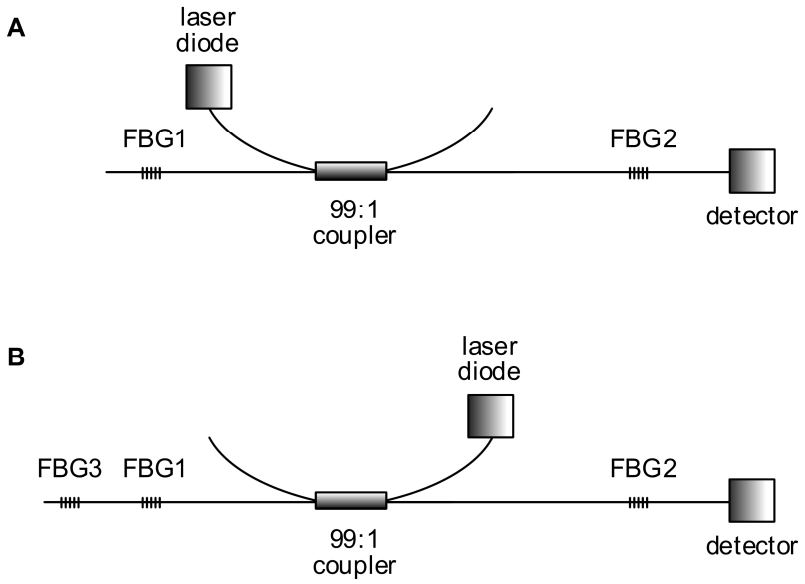

Figure 4.3: Two configurations of the side-pumped FBG cavity.

In configuration A the detector receives light that is both transmitted and reflected. In configuration B the detector only receives light that has been reflected.

The pulsed ringdown method was used to determine the length of the cavity –100 ns pulses at 1531.720 nm were injected and ringdown traces recorded. The average round-trip time t_r from the difference between peaks was found to be 760 ± 10 ns. From this the cavity length is determined to be 78 ± 1 m.

For both configurations **A** and **B** the phase angle as a function of frequency and wavelength was measured over the ranges 20 to 300 kHz in 20 kHz steps and 1531.600 to

1531.700 nm in 0.01 nm steps. This wavelength range is near the edge of the Bragg resonance (λ_B = 1530 nm, see Figure 4.1) so R and τ were expected to decrease with λ.

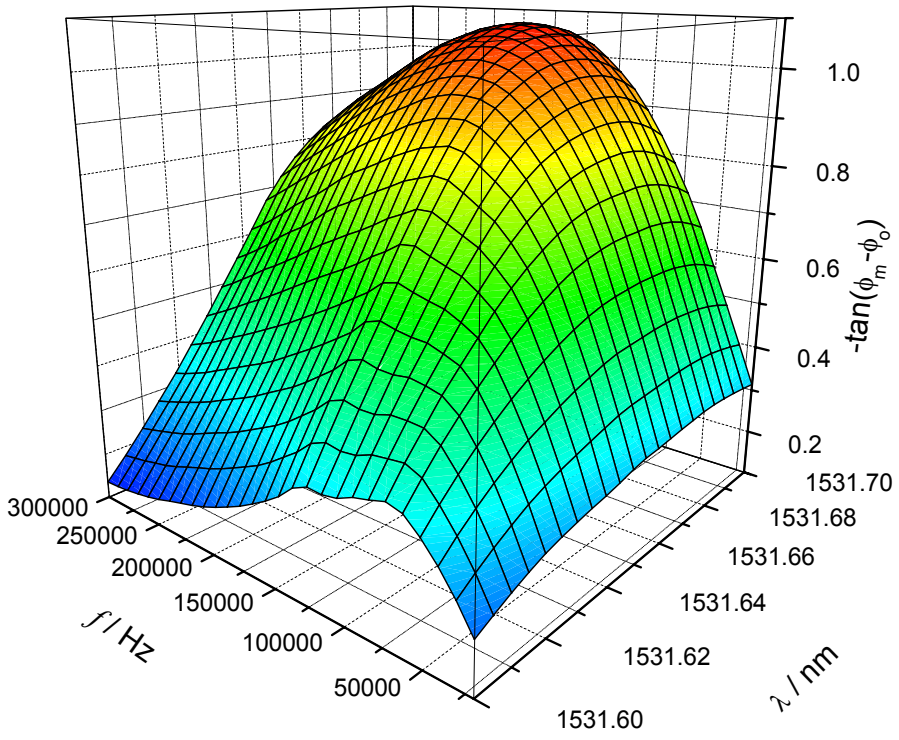

Figure 4.4: 3D plot of FBG cavity transmission with wavelength and frequency for configuration A.

Figure 4.4 shows a three-dimensional plot of the tangent of the corrected phase angle (the negative is taken to display it in "transmission mode") against the modulation frequency and wavelength for configuration **A**. The plot shows a steep negative slope at low frequency and gentle positive slope a high frequency characteristic of a biexponential (or multiexponential) decay. The trend with wavelength shows the expected behaviour, with transmission decreasing as the laser is tuned from 1531.700 nm onto the Bragg resonance.

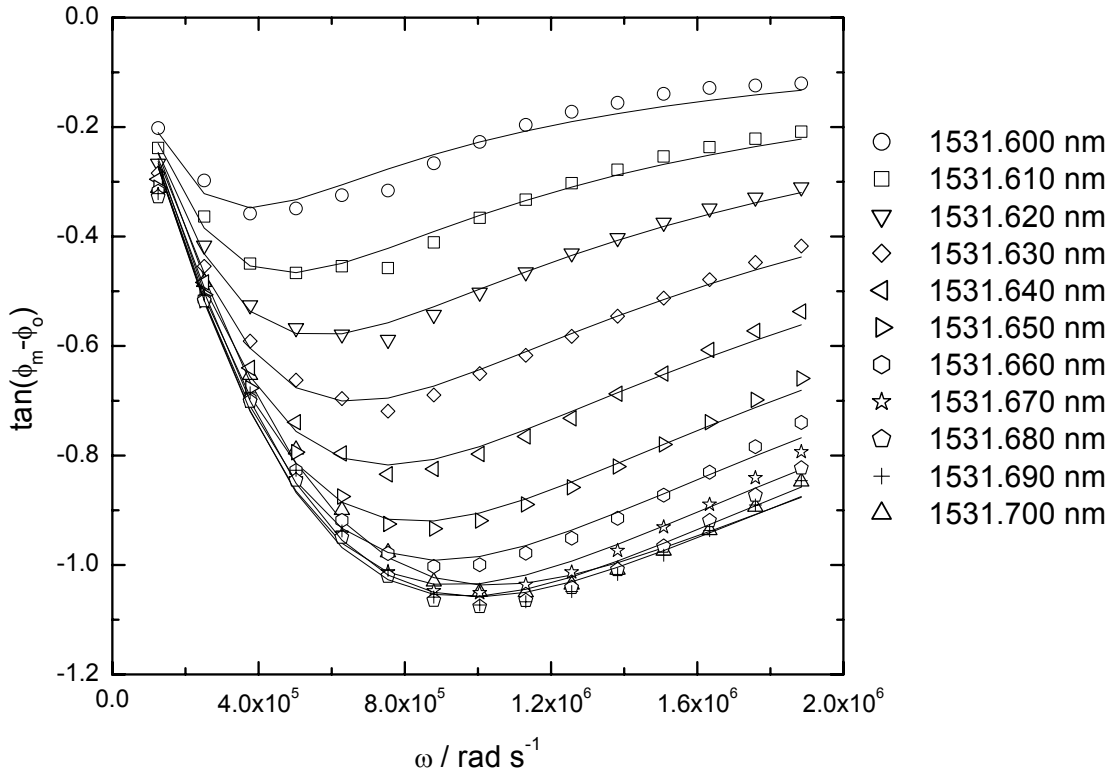

Figure 4.5: Fits to the data using a biexponential model for configuration A.

Figure 4.5 and Table 4.1 show the results from fitting the data in Figure 4.4 to a biexponential model. The product of the grating reflectivities, $R_1R_2 = R$ is estimated as

$$R = 1 + \varepsilon_{fibre}L + \varepsilon_{splice} + \varepsilon_{coupler} - \frac{nL}{c_o\tau_1} \qquad (4.3)$$

The loss of the splices (ε_{splice}) as estimated by the fusion splicer was 1.8 %. The coupler insertion loss ($\varepsilon_{coupler}$) was estimated as 2 %. The fibre loss is given by the manufacturer as 0.22 dB / km.

Table 4.1: Fitting results for the side-pumped FBG cavity

λ / nm	α_1	α_2	τ_1 / s	τ_2 / s	R
1531.600	0.494	0.506	3.76E-06	6.86E-12	0.937
1531.610	0.594	0.406	3.29E-06	9.47E-12	0.922
1531.620	0.669	0.331	3.07E-06	1.10E-11	0.914
1531.630	0.777	0.223	2.91E-06	1.67E-11	0.907
1531.640	0.760	0.240	2.81E-06	1.78E-11	0.903
1531.650	0.798	0.202	2.74E-06	2.08E-11	0.899
1531.660	0.824	0.176	2.69E-06	2.29E-11	0.896
1531.670	0.834	0.166	2.65E-06	2.63E-11	0.894
1531.680	0.848	0.152	2.61E-06	3.26E-11	0.892
1531.690	0.847	0.153	2.52E-06	4.09E-11	0.887
1531.700	0.832	0.168	2.39E-06	5.79E-11	0.878

The modulation depth was recorded concurrently with the phase angle in the wavelength and frequency scans. Figure 4.6 shows the trend in modulation depth one would expect: the modulation depth increases as the ringdown time decreases at a given frequency. Only the data for the first five wavelengths is shown since the laser power was kept constant over this range. Due to the lower frequency limit of the lock-in (20 kHz) the maximum modulation depth, which is necessary for normalization of *m* for comparison of data acquired at different power and for fitting, could not be obtained.

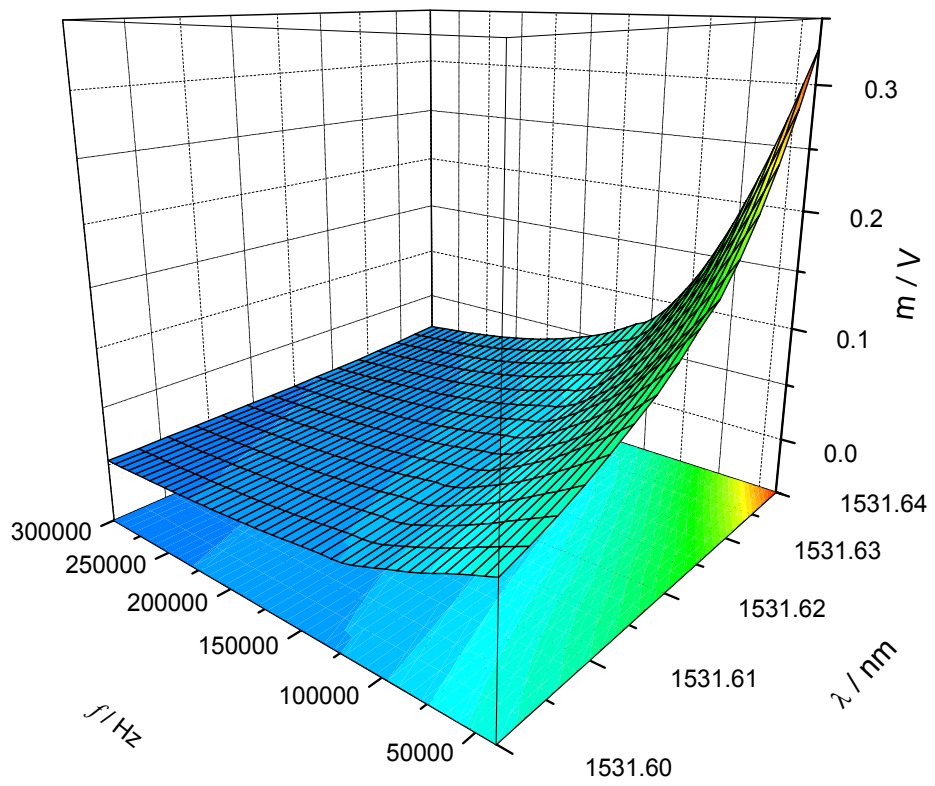

Figure 4.6: Dependence of the modulation depth on wavelength and frequency for configuration A.

In Figure 4.7 a plot of phase angle with wavelength and frequency is shown for the cavity in configuration **B**. The shape of the surface shows similar trends to that in Figure 4.4 and indicates that this configuration does not result in the elimination of the "direct light" as predicted, but instead also shows bi-exponential or even multi-exponential behaviour.

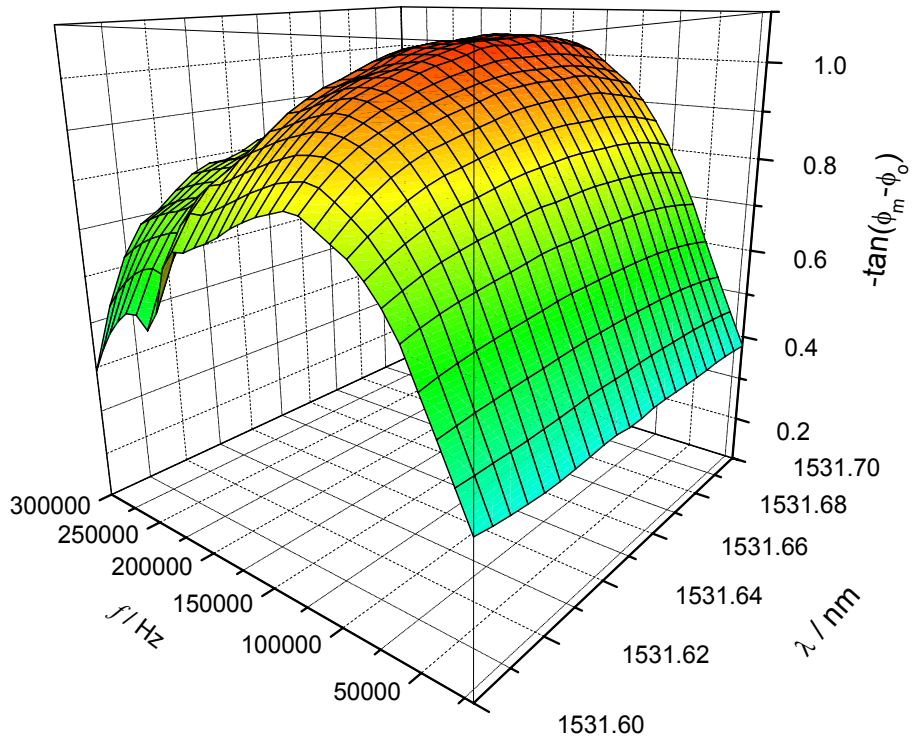

Figure 4.7: 3D plot of FBG cavity transmission with wavelength and frequency for configuration B.

The data were fit to a bi-exponential model; this is shown in Figure 4.8. The ringdown times and the steady-state intensity of the short "decay" are plotted together in Figure 4.9 for comparison with the results from configuration **A**.

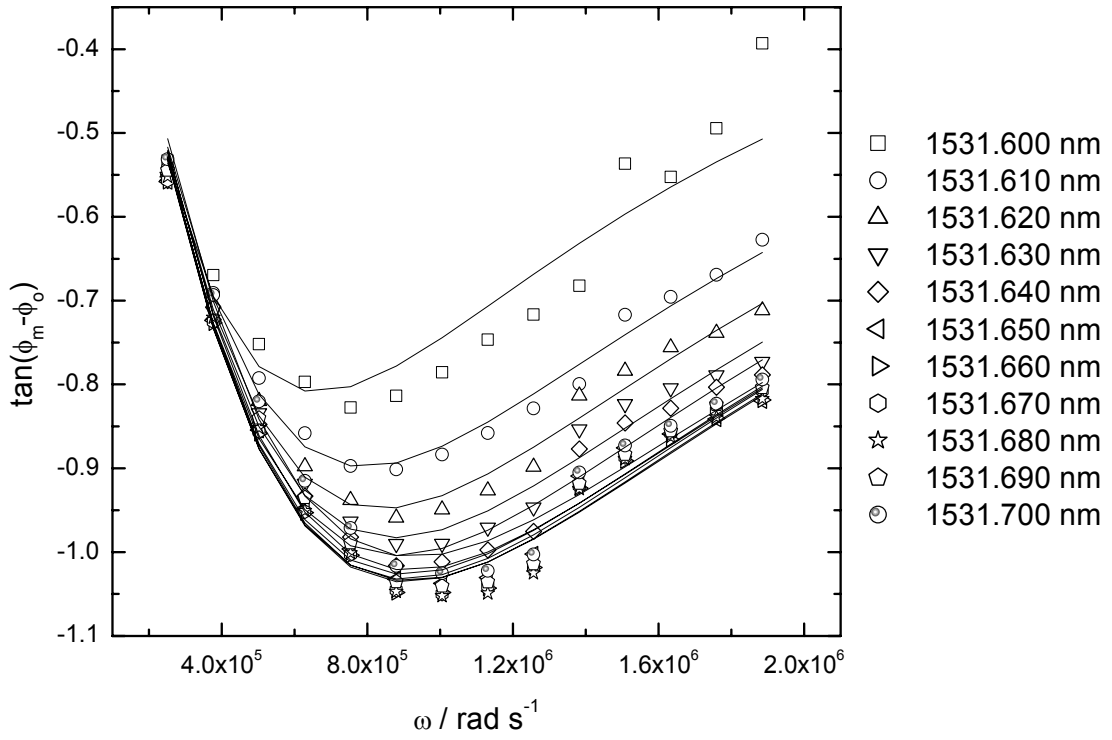

Figure 4.8: Fits to the data using a biexponential model for configuration B.

The slow decays for the two configurations do not agree at all wavelengths but show a similar trend. The fast decays are expected to be short and relatively constant since they are due to light traveling directly from the laser to the detector (discussed below). τ_2 for both configuration **A** and **B** meet these expectations. The steady-state intensity of the "direct" light decreases with wavelength in both cases and approach the same value. Below 1531.650 nm α_2 for configuration **A** is considerably larger than for **B**. These results in the context of the presence of ASE are discussed below.

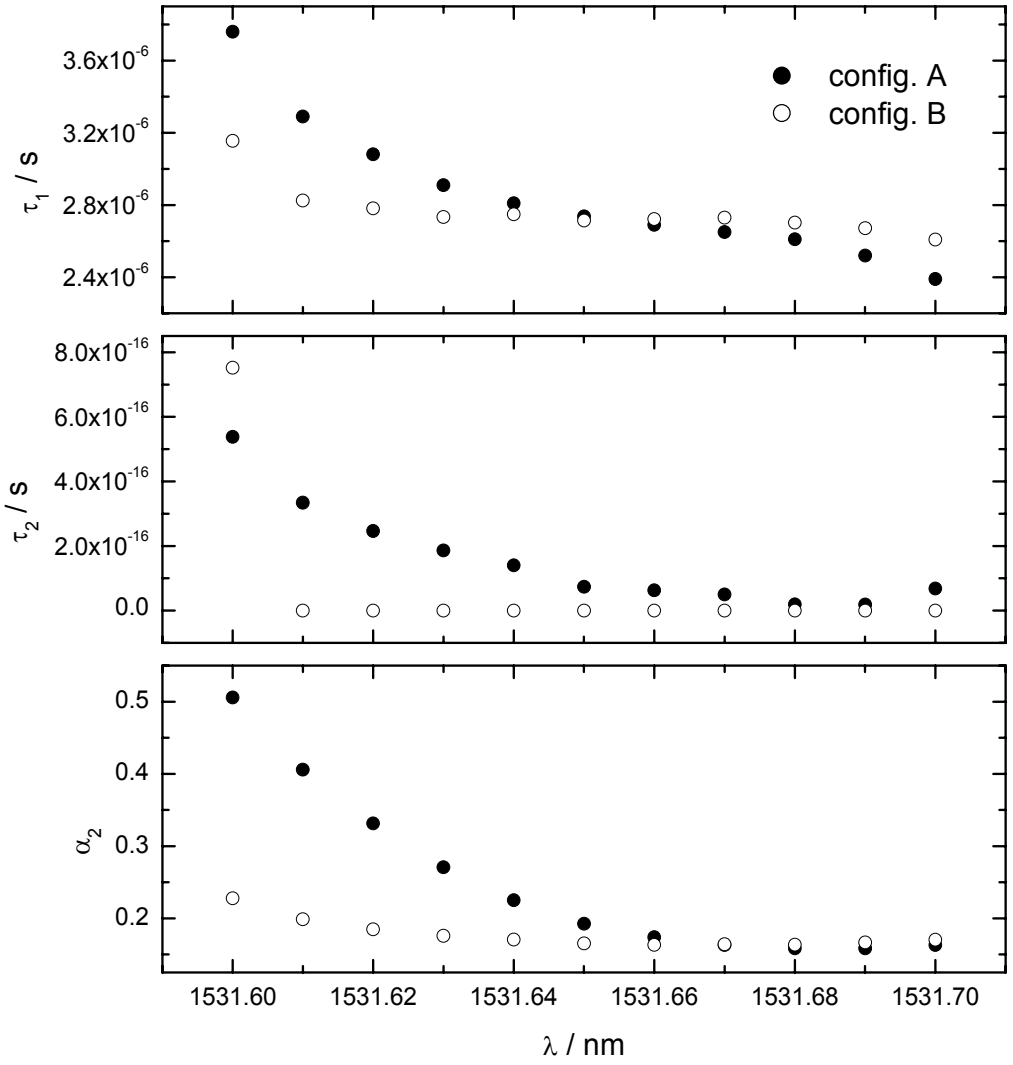

Figure 4.9: Comparison of the decay times and steady-state intensity for configurations A and B.

4.4 Detection of amines

N-H bonds exhibit a stretching vibration overtone absorption near 1530 nm with an absorption coefficient of ~ 275 L mol^{-1} cm^{-1}.[7] Amine groups are common in biological molecules and thus NIR-FCRDS may provide a means of detecting these species. O-H groups also show a small absorption in this range (~36 L mol^{-1} cm^{-1}).[7] As water would be the solvent of choice for almost any biomolecule, absorption due to the solvent may

eclipse any absorption due to the N-H stretch. It may be possible to use D_2O as a solvent since its stretching overtone will be red-shifted relative to H_2O and may provide a window for observing N-H. However, proton exchange with the solvent and subsequent quick diffusion of HOD may lead to band broadening during electrophoresis resulting in poor separation resolution. Of course the exchange could be controlled via the pH of the solution, with more basic solutions showing a slower rate. The C-H stretch overtone could also be probed but it lies outside the wavelength range of our laser for most molecules. Here the performance of FD-FCRDS in detecting two simple amines is tested.

A capillary interface[8] was spliced into the FBG cavity to allow the introduction of an absorbing species. From a micrograph the gap is estimated to be 75 μm. A syringe pump was used to force flow of H_2O, DMSO, benzylamine, and *m*-xylylenediamine through the interface. Figure 4.10 shows the apparatus (a slightly modified form of configuration **A**) and an image of the interface.

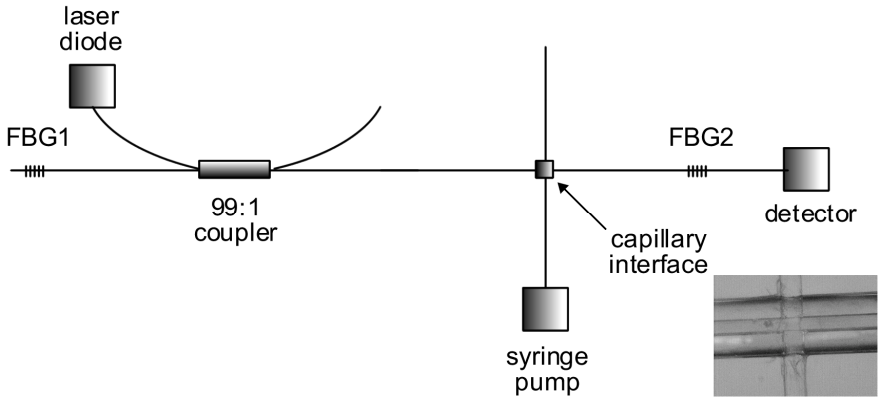

Figure 4.10: Apparatus and image of flow cell for detection of amines.

The laser was stepped from 1530.000 to 1532.000 nm in 0.020 nm increments, recording the phase and modulation at each wavelength to form the cavity spectrum shown in Figure 4.11. One notes a turn-around in the phase shift as the high reflectivity region of the cavity is approached. This behaviour is due to ASE and is explained below.

Light in cladding modes may also make a contribution to the turn-around. There are two possible sources of cladding modes. Firstly, there is a mismatch between the laser output mode field radius (MFR ~ 5.95 μm) and the MFR of the fibre (5.00 μm). The light incident on the fibre not falling on the core may be coupled into cladding modes, with 4.8 % of the light entering the cladding assuming a Gaussian distribution. Secondly, the beam expands as it traverses the sample gap. Here with a gap of 75 μm, only 16 % of the light is incident on the core of the receiving fibre, while the remaining 84% is incident on the cladding. At the Bragg wavelength, cladding modes will pass straight through the cavity without reflection and will therefore have a phase angle identical to the ASE. Recall from Chapter 3 that the cladding modes can couple back into the core mode. 1.36 dB of the laser peak may be due to light in the cladding introduced at the gap. This was determined from the difference of the means of the maximum attenuation in the cavity spectra obtained with and without the sample interface.

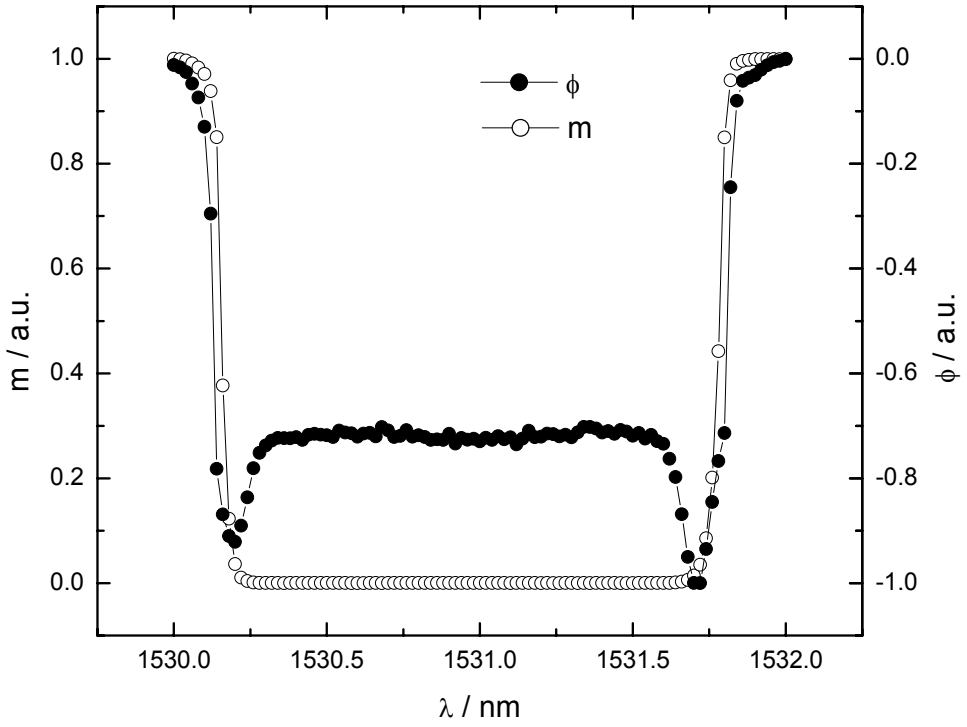

Figure 4.11: Phase and modulation cavity spectra with the sample interface.

Figure 4.12 shows the modulation spectra recorded for water, DMSO, benzylamine ($BzNH_2$), and xylylenediamine ($Xy(NH_2)_2$) across a wavelength range where the cavity spectrum is relatively flat. The curved shape, present in all spectra, is thought to be due to ASE. The modulation depth was observed to decrease in the order DMSO > $BzNH_2$ > $Xy(NH_2)_2$ > H_2O. Recall from Chapter 2 that for a cavity/loop the modulation depth is expected to increase with increasing absorption (i.e. decreasing ringdown time). Thus the observed trend for DMSO and the amines is opposite the trend predicted by making use of the absorption coefficients given in Table 4.2. Water having the smallest observed modulation depth may be related to its comparatively low refractive index (RI). Light transmitted from a fibre facet will be more divergent upon entering a

low RI medium than a high RI one (see Chapter 1) and thus less light will be incident on the core of the receiving fibre.

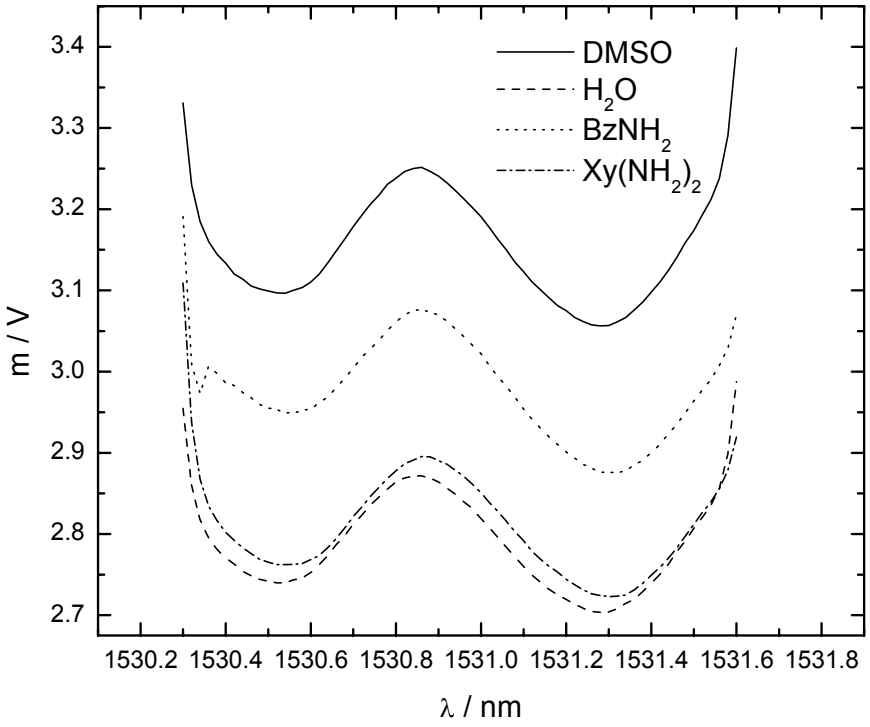

Figure 4.12: Modulation spectra of water, DMSO, benzylamine, and xylylenediamine.

Figure 4.13 shows the ratio of the modulation depth of the diamine with respect to DMSO to that of the monoamine also referenced to DMSO. The ratio is close to 2:1 over the wavelength range examined, and is the ratio expected since the diamine has twice the absorption of the monoamine. Deviations from the 2:1 ratio may be explained by differences in spectral shape for the two molecules or by fluctuations in ASE intensity.

Table 4.2: Absorption coefficient and refractive indices of the compounds examined.

compound	ε / L mol^{-1} cm^{-1}*	n†
DMSO	0	1.479
H_2O	70	1.330
$BzNH_2$	550	1.543
$Xy(NH_2)_2$	1100	1.571

* Absorption coefficient at 1530 nm. † Refractive index at 633 nm.

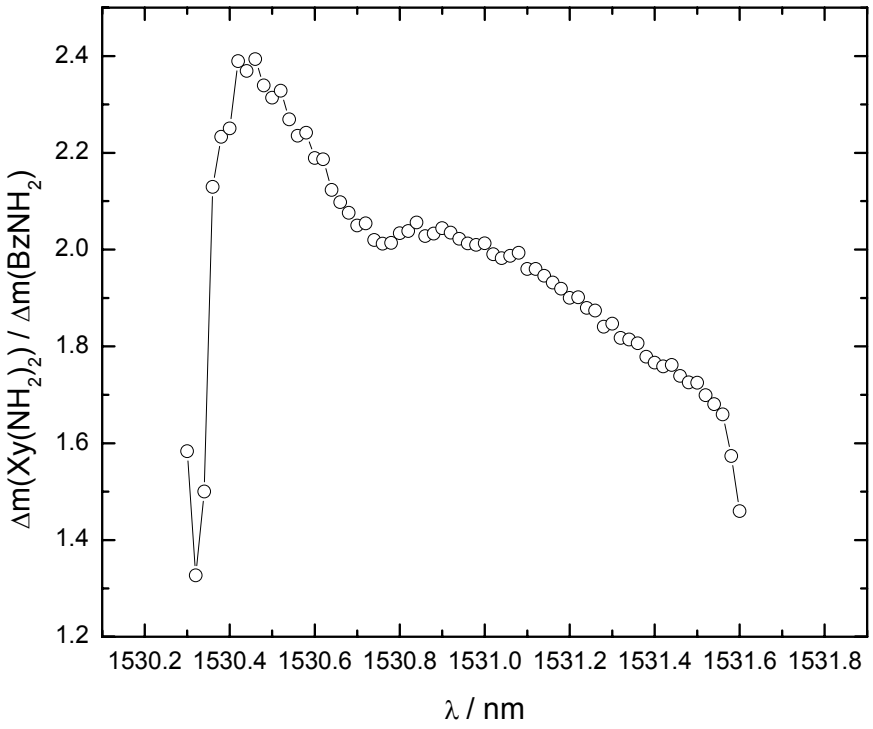

Figure 4.13: Ratio of the modulation depth of the diamine to the monoamine.

The detection limit for the diamine was determined to be εC_{DL} = 360 cm^{-1}. This poor result is due to the apparatus behaving effectively as a single-pass instrument rather than a multi-pass one. This behaviour is attributed to the presence of ASE, discussed in more detail in the next section.

4.5 Effect of ASE

Amplified spontaneous emission (ASE) is broadband emission from a laser diode generally 10^4 times less intense than the laser emission. It has been noted by other researchers that while ASE is normally negligible, its effect while performing FD-CRDS cannot be ignored.[9, 10] The reason is that when using such high reflectivity mirrors or FBGs the laser light reaching the detector will be attenuated to such an extent that ASE outside the bandwidth of the mirrors will form a significant portion of the light striking the detector. This is the source of the "direct light" encountered above.

In the previously reported experiments the researchers accounted for the effect of ASE in two ways not possible with a fibre cavity and a near infrared source. Engeln et al. used a strong absorber in the cavity to completely attenuate the laser light so only the ASE reached the detector and its phase and intensity contributions could be measured.[9] Kasyutich et al. purposefully misaligned one mirror, again so the laser light does not reach the detector, while the ASE outside the reflection band of the mirror is transmitted and detected.[10] In the NIR range of the laser used in our experiments the most common absorption features present are the first overtones of stretching vibrations found in the IR. These overtones typically have absorption coefficients of < 300 L mol^{-1} cm^{-1} per bond; too weak to completely attenuate the laser light even with a neat liquid. Highly conjugated molecules have their electronic transition shifted from the visible range into the NIR and strong absorbers in the 750 – 900 nm range are available. To the knowledge of the author no strong absorbers in the 1520 – 1620 nm range are available

commercially, so following the example of Engeln et al. is not easily done. FBGs, while similar to mirrors, cannot be altered to couple the forward propagating core mode anywhere but the reverse propagating core mode, so the option exercised by Kasyutich et al. is not feasible in our case.

Below we show that ASE reaches the detector for three cavity configurations; **A**, **B**, and another configuration **C**. We also show that ASE can be nearly eliminated in our current system and propose a system where its complete elimination should be possible. This is expected to make future NIR detection schemes more successful.

The laser emission spectrum (Figure 4.14) was recorded using an optical spectrum analyzer (OSA, Agilent 86140B). The full width at half maximum (FWHM) was found to be 0.048 nm wide with a small side band seen 0.020 nm to the blue and nearly 30 dB below the main emission. On a linear scale the laser line can be fit to a Gaussian with R^2 = 0.999. Broadband ASE is not apparent here, with the baseline being 48 dB below the laser intensity.

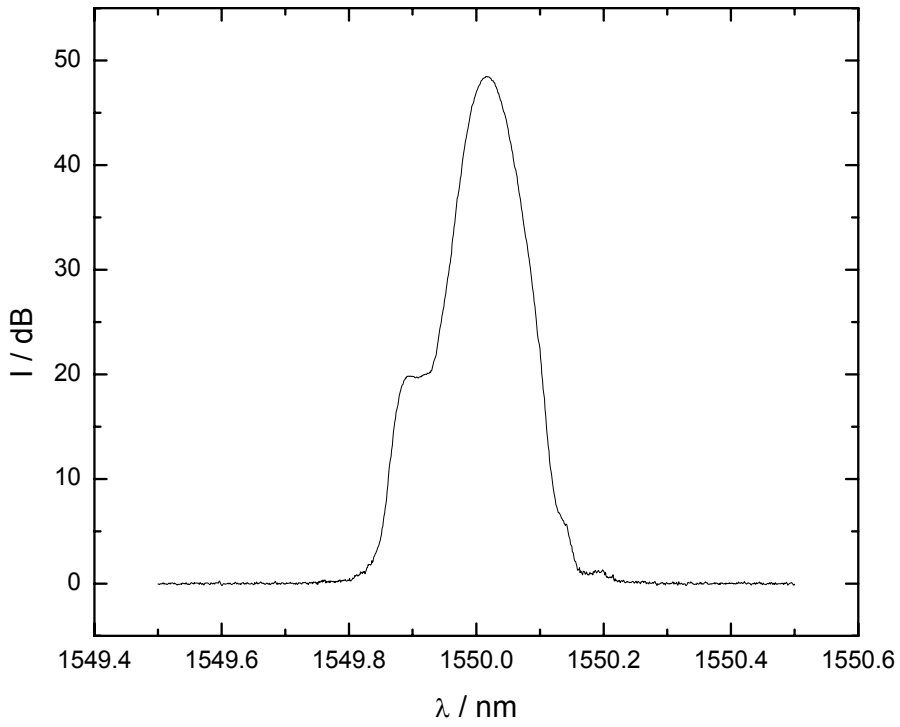

Figure 4.14: Laser emission spectrum.

The side-pumped FBG cavity spectrum (configuration **A**) recorded with a broadband source is shown in plot A of Figure 4.15. The presence of ASE becomes apparent when the cavity spectrum is recorded by using the laser tuned to the Bragg resonance as a light source (plot B). Here the laser line can be seen, greatly attenuated, at 1531.000 nm. ASE illuminates all the features of the cavity spectrum, including the cladding mode resonances to the blue of the Bragg resonance. If ASE were not present, no features other than the laser line would be seen. Here the peak ASE is 6.5 times greater than the attenuated laser peak. Thus in the wavelength range where absorption spectroscopy was performed (Chapter 4.4) ASE is dominant, and the system effectively behaves as a single-pass absorption spectrometer, with the modulation depth being

directly proportional to the transmitted power. This fact explains the decreasing trend in *m* with increasing absorption in Figure 4.12 and the poor detection limit obtained. With the laser tuned to 1530.600 nm and 1530.700 nm the laser light is more prominent than the ASE by 12.7 and 29.4 dB, respectively (not shown). Thus for the experiments in Chapter 4.3 the multi-pass picture is still valid since the laser light is much more intense than the ASE.

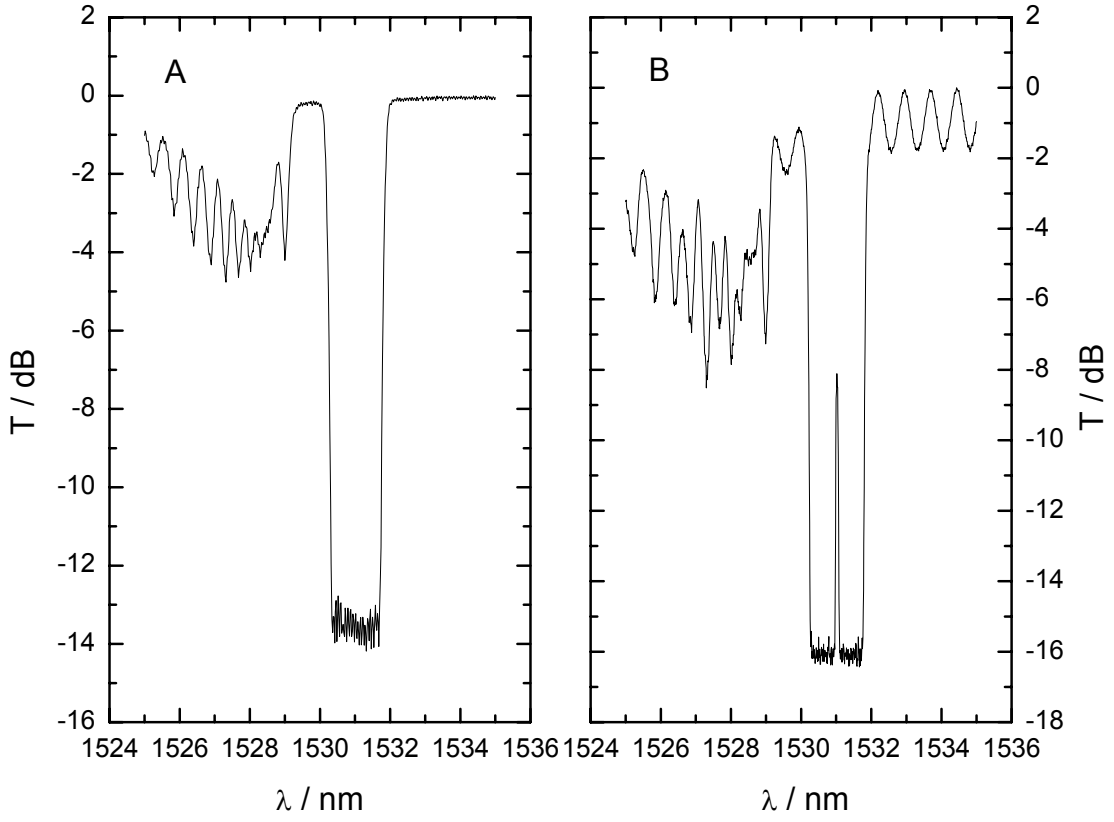

Figure 4.15: FBG cavity spectra for configuration A.

Spectrum A was recorded using a broadband illumination source. Spectrum B shows the cavity spectrum recorded using a laser as the light source. ASE is evident in B since features other than the laser line are present.

Similar spectra were gathered with the apparatus in configuration **B** and are shown in Figure 4.16. Two features are apparent in plot A, acquired with a broadband source.

These peaks near the edges of the grating attenuation bands are due to a mismatch of reflection bandwidth. Referring to Figure 4.3, FBG1 has a wider reflection band than FBG2. Thus some light reflected from FBG1 passes by FBG2 and reaches the detector. Plot B, acquired with the laser source, shows these same features due to reflection of ASE, as well as the laser line at 1531.02 nm. The ASE peak at 1530.15 nm is 2.7 dB more intense than the laser line. This explains the biexponential behaviour observed in Figure 4.7. At 1530.600 and 1530.700 nm the peak laser to ASE power ratio is 17.9 and 32.4 dB, respectively. Thus the interpretation of the system as biexponentially decaying is valid. The lower relative ASE power in configuration **B** as compared to **A** is consistent with the results presented in the lower panel of Figure 4.9 where α_2 for **B** is less than for **A** at most wavelengths.

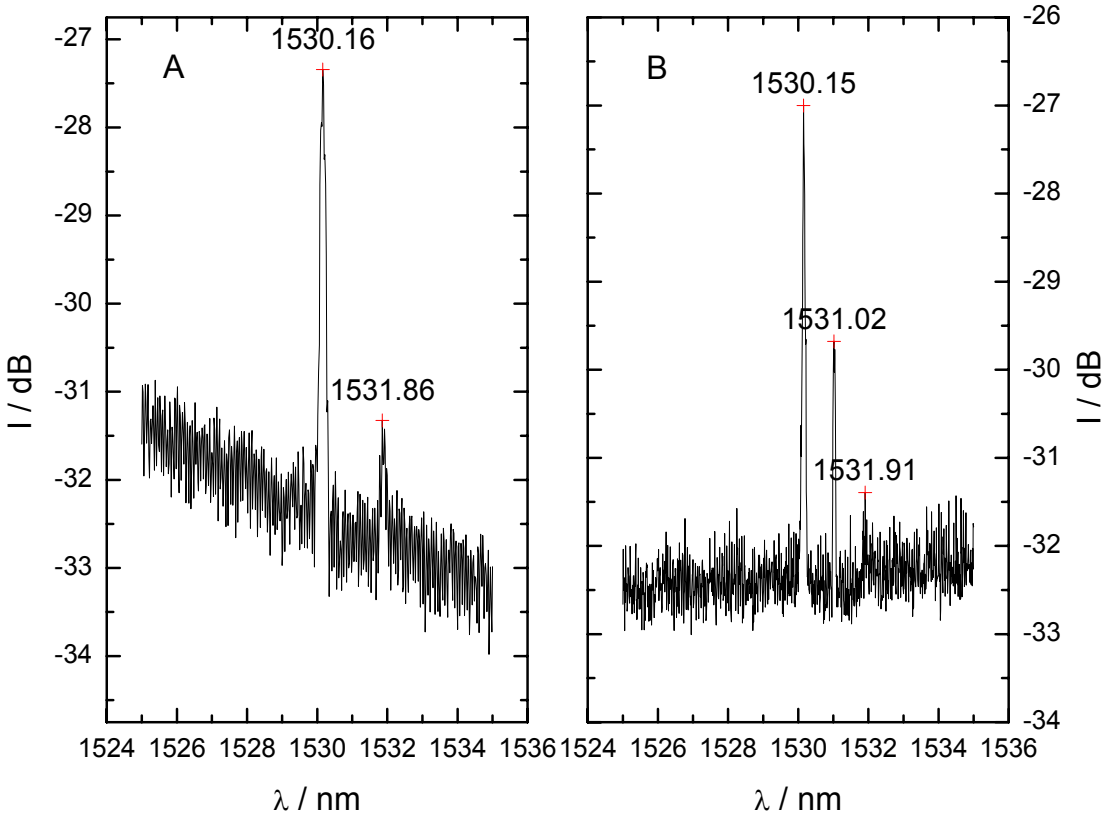

Figure 4.16: FBG cavity spectra for configuration B.

Spectrum A and B use a broadband and laser light source for illumination, respectively. The peaks in A are due to mismatch of the reflection bands of the gratings. In B, ASE is evident in the features other than the laser line.

In an attempt to minimize the ASE reaching the detector, the laser is first reflected from the narrower band FBG2, where most ASE leaves the cavity, and then reflected from the wider band FBG1, behind which is placed the detector. We term this configuration **C**. It was also noted that broadband reflection occurs at the fibre facet outside the cavity. To quell this reflection, index-matching liquid (DMSO) is placed on the fibre facet. Figure 4.17 displays the cavity spectrum with DMSO on the fibre facet and with DMSO in the sample gap, showing the reduction of ASE compared to the laser

line. Some mismatch of the gratings is still present, evidenced by the small peak at 1531.83 nm.

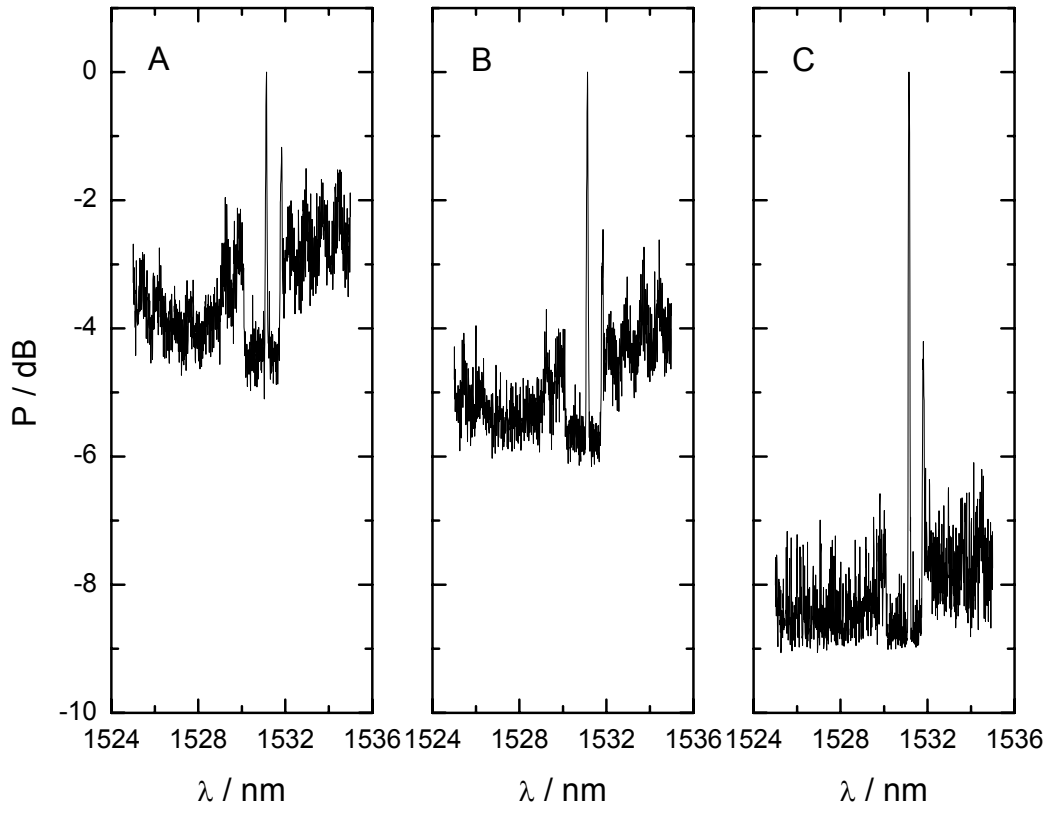

Figure 4.17: Cavity spectra showing broadband ASE reflection from fibre facets.

The laser peak at 1531 nm was offset to 0 dB for easy comparison. In plot A no means to reduce ASE reflection were used. In Plot B, DMSO was used to reduce reflection from the end facet of the cavity. Plot C shows the spectrum for DMSO on the end facet and in the sample interface.

In panel B of Figure 4.17, the peak ASE is reduced by 25 % compared to panel A by placing DMSO on the cavity end facet. In panel C, the peak ASE reduced 50 % compared to panel A by additionally introducing DMSO in the sample gap. Finally, DMSO was also placed on the end facet of the 99 % leg of the 2x2 coupler and the spectrum recorded (Figure 4.18). The ratio of the laser peak area to the reflection mismatch ASE peak area is 92.5:7.5. This configuration accomplishes the goal of having

the laser power reaching the detector be greater than the ASE. No features are discernible other than the laser and reflection mismatch peaks, indicating ASE has been nearly eliminated.

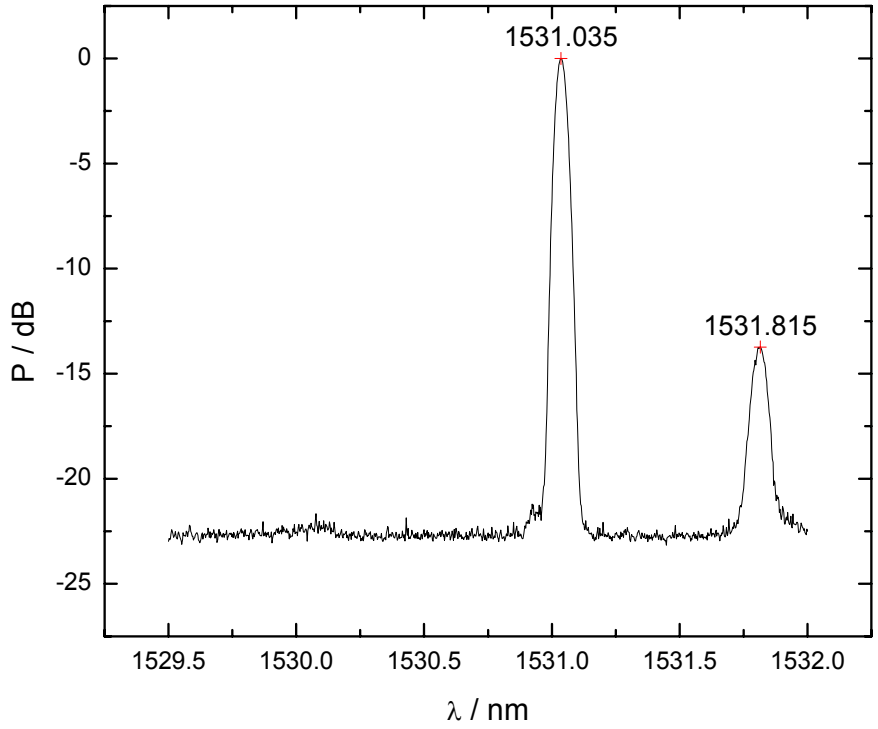

Figure 4.18: Cavity spectrum with DMSO on all reflection points.

Thus, to minimize the effect of ASE in an FBG cavity, a side-pumped cavity in reflection mode should be used, reflecting off a narrow band FBG first to eliminate ASE, then off a wider band FBG, behind which is placed the detector. Near elimination of ASE can be realized by placing an index matching liquid on all fibre facets to minimize broadband reflection reaching the detector.

Referring back to Figure 4.11, when the laser is tuned onto the Bragg resonance the ratio of ASE intensity to core intensity reaching the detector will increase and thus the overall phase angle will be weighted more towards that of the ASE. At some

intermediate reflectivity the dominating contribution to the ratio changes and a turn-around in phase is observed. In the high R region ($R > 0.99$) it may no longer be valid to relate the phase angle to a ringdown time since the majority of the light passes directly from the laser to the detector. (For $R < 0.94$ as in the experiments in 4.3 the majority of the light is laser light carried in the core so assigning a ringdown time is valid.) The modulation spectrum does not exhibit such a turn-around, and would not be expected to. The ASE contributes a small but non-zero modulation depth to the overall modulation. As the laser is tuned towards the Bragg wavelength, the modulation depth decreases consistent with an increase in ringdown time, until the laser intensity striking the detector is nearly zero.

4.6 Conclusion

The feasibility of performing CRDS in the frequency domain using an optical fibre cavity medium was examined. Two FBG cavity configurations were characterized at wavelengths near the edge of the cavity reflection band. A maximum ringdown time of 3.76 μs at 1531.600 nm was observed. Contributions from a second exponential decay with very short "ringdown" times indicated that non-resonant light was reaching the detector. The response of the cavity upon introduction of absorbing species was then tested. A detection limit for *m*-xylylenediamine of εC_{DL} = 360 cm^{-1} was obtained. Recording the cavity spectrum with the laser as the light source revealed ASE as the major component of non-resonant light. Minimizing the intensity of ASE reaching the

detector is the most important factor in good FD-CRDS performance. A method for achieving this was demonstrated, and its application should allow a much lower detection limit to be reached compared to the experiments presented in Chapter 4.4, where most of the light passes through the sample a single time. In summary, FD-CRDS using a well-configured cavity with provision to minimize ASE shows promise for sensing and spectroscopic applications that require a very small liquid volume to be probed.

The final optimized cavity configuration presented is in effect a way of filtering any non-resonant light so that it does not reach the detector. In a time domain experiment under short pulse excitation, all the non-resonant light would be contained within the first peak of the ringdown event. Therefore all non-resonant light could be easily filtered by excluding the first peak from fitting. Thus, while FD-CRDS is better suited to electrophoretic and chromatographic applications by way of its higher time resolution, working in the time domain may be beneficial since filtering of non-resonant light is easily achieved. However, the increase in experimental complexity for effective filtering in FD-CRDS is not great. In conclusion, FD-CRDS is likely the better choice for incorporation with microfluidic systems.

These experiments were performed with FBGs that have a relatively narrow bandwidth (FWHM ~ 2 nm) so spectroscopic applications are limited for the liquid phase since absorption features are generally broad. In the future, use of commercially available broadband FBGs with a FWHM of 50 nm and reflectivity of 94 % could enable broader ranging spectra to be recorded.

4.7 References

1. von Lerber, T.; Sigrist, M. W., Cavity-ring-down principle for fiber-optic resonators: experimental realization of bending loss and evanescent-field sensing. *Applied Optics* **2002,** 41, 3567-3575.

2. Vogler, D. E.; Lorencak, A.; Rey, J. M.; Sigrist, M. W., Bending loss measurements using a fibre cavity ringdown scheme. *Optics and Lasers in Engineering* **2005,** 43, 527-535.

3. Vogler, D. E.; Muller, M. G.; Sigrist, M. W., Fiber-optic cavity sensing of hydrogen diffusion. *Applied Optics* **2003,** 42, (27), 5413-5417.

4. Gupta, M.; Jiao, H.; O'Keefe, A., Cavity-enhanced spectroscopy in optical fibers. *Optics Letters* **2002,** 27, (21), 1878-1880.

5. Schroeder, K.; Ecke, W.; Mueller, R.; Willsch, R.; Andreev, A., A fibre Bragg grating refractometer. *Measurement Science & Technology* **2001,** 12, (7), 757-764.

6. Laffont, G.; Ferdinand, P., Tilted short-period fibre-Bragg-grating-induced coupling to cladding modes for accurate refractometry. *Measurement Science & Technology* **2001,** 12, (7), 765-770.

7. Buback, M.; Vögele, H. P., *FT-NIR Atlas*. VCH Publishers: Weinheim, 1993.

8. Li, R. K.; Loock, H. P.; Oleschuk, R. D., Capillary Electrophoresis Absorption Detection Using Fiber-Loop Ringdown Spectroscopy. *Analytical Chemistry* **2006**.

9. van Helden, J. H.; Schram, D. C.; Engeln, R., Phase-shift cavity ring-down spectroscopy to determine absolute line intensities. *Chemical Physics Letters* **2004,** 400, (4-6), 320-325.

10. Kasyutich, V. L.; Martin, P. A.; Holdsworth, R. J., Effect of broadband amplified spontaneous emission on absorption measurements in phase-shift off-axis cavity enhanced absorption spectroscopy. *Chemical Physics Letters* **2006,** 430, (4-6), 429-434.

Chapter 5 Fibre loop ringdown spectroscopy using standard telecom components

Optical fibre offers the possibility of forming an optical cavity without using mirrors or fibre Bragg gratings (see Chapter 4). This can be accomplished simply by joining a length of fibre to itself to form a loop. Light injected into the loop will propagate around and return to its starting point travelling in the same direction. The only source of loss in a perfect loop would be from the fibre material itself. Optical fibre is designed to have high transmission in a wavelength range of several hundred nanometres in the telecom region. (The major telecom bands are the S-band: 1485 to 1520 nm, the C-band: 1530 to 1562 nm, and the L-band: 1570 to 1610 nm. Fibre transmission is high from ~ 1300 to 1700 nm). Thus a fibre loop represents a broadband, low loss resonator that can be easily and inexpensively fabricated.

The equations describing the round-trip time (t_r), the ringdown time (τ), and the free spectral range (FSR, $\Delta\nu$) for a loop are slightly different than for a linear cavity. This difference arises because light in a loop need only traverse the entire resonator length once to return to its starting point rather than twice as in the case of a linear cavity. Thus a factor of two or one-half needs to be removed to describe a loop. The round-trip time becomes

$$t_r = \frac{nL}{c_o} \tag{5.1}$$

The general expression for ringdown time is now

$$\tau = \frac{t_r}{\Gamma_{fibre} + \Gamma_{components} + \Gamma_{sample}} \tag{5.2}$$

Note that upon substituting (5.1)into (5.2) the loop ringdown time becomes equal to that for a linear cavity:

$$\tau = \frac{nL}{c_o\left(-\ln\left(T\right)+\Gamma_{components}+\varepsilon Cd\right)} \tag{5.3}$$

Finally, the free spectral range is now defined as

$$\Delta\nu = \frac{c_o}{nL} \tag{5.4}$$

All other equations relating to a conventional cavity also apply to a loop with only one minor change: the reflectivity R for a cavity is replaced by the transmission of the loop T.

Fibre–loop ringdown spectroscopy (FLRDS) at telecom wavelengths using evanescent sensing via a tapered fibre to record the absorption spectrum of 1-octyne[1] and to detect single cells[2] has been recently reported. In these time domain experiments Lehmann et al. achieve very long ringdown times (50 μs) by using a very long loop (2.2 km). They recorded the first vibrational overtone spectrum of 1-octyne between 1520 and 1550 nm. 1-octyne is a stronger absorber than any of the analytes we examine below (ε = 3700 L mol^{-1} cm^{-1}). They report a detection limit of 1.05 % 1-octyne in decane by volume. This corresponds to εC_{DL} = 263 cm^{-1}. For the cell detection experiments they use large cells (> 10 μm diameter) which have a high scattering efficiency. To concentrate the cells in the evanescent field, they coated the tapered region with a polypeptide which the cells adhere to. They report a change in ringdown time of $\Delta\tau$ = 230 ns per cell.

In our laboratory we record the absorption of an analyte which is brought directly into the light's path rather than absorption via the evanescent wave demonstrated by Lehmann et al. Since a loop has no end, side-pumping and side-tapping must be used. The problems due to ASE encountered in the side-pumped linear cavity experiments (Chapter 4) are not expected to be encountered here due to the broadband nature of the loop, i.e. the ASE and laser light should be attenuated equally over all wavelengths before reaching the detector.

We present the phase and modulation spectra of four liquid species acquired with a frequency domain (FD) fibre-loop ringdown spectrometer.

5.1 Apparatus and experiment

A fibre–loop was fabricated from two 99:1 FFEF couplers (Lightel Technologies Inc.), 5 m of fibre (Corning SMF-28), and a drilled 100 μm capillary interface[3] in which the flat-cleaved fibre ends formed a gap of 75 μm. These components were spliced together with a Fitel S182A fusion splicer. The loss due to the couplers and splices was estimated as 7 % per pass. The loop is shown schematically in Figure 5.1. The same laser, lock-in amplifier, detector, function generator, amplifier, and oscilloscope listed in Chapter 4 were also used here. The phase angle and modulation depth were recorded as a function of laser wavelength using a 4 mW beam intensity modulated at f = 263.2 kHz. To record spectra, the wavelength was stepped by 1.000 nm from 1520.000 to 1620.000 nm – the entire available range of the laser. At each step the phase and modulation were

averaged for 5 s at 10 Hz. In the figures below the modulation depth is not normalized and the phase angle is not referenced to the phase offset. Neat liquids were flowed through the interface using a syringe pump (Harvard Apparatus pump II) at 2 μL / min. Chemicals were purchased from Sigma-Aldrich and used without further purification. Spectra were recorded for the following liquids: water, dimethylsulfoxide (DMSO), benzylamine ($BzNH_2$), and *m*-xylylenediamine ($Xy(NH_2)_2$).

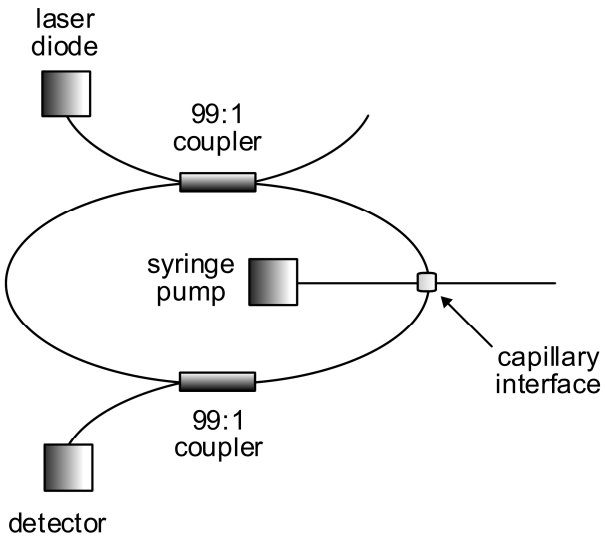

Figure 5.1: Fibre loop with capillary interface.

Light is coupled in and out of the loop via 99:1 FFEF couplers. The light path intersects the sample flow at right angles in the capillary interface.

5.2 Results and discussion

5.2.1 Modulation spectra

The modulation spectra of the four liquids are shown in Figure 5.2. The DMSO spectrum was used as a baseline and was subtracted from the other modulation data, shown in Figure 5.3.

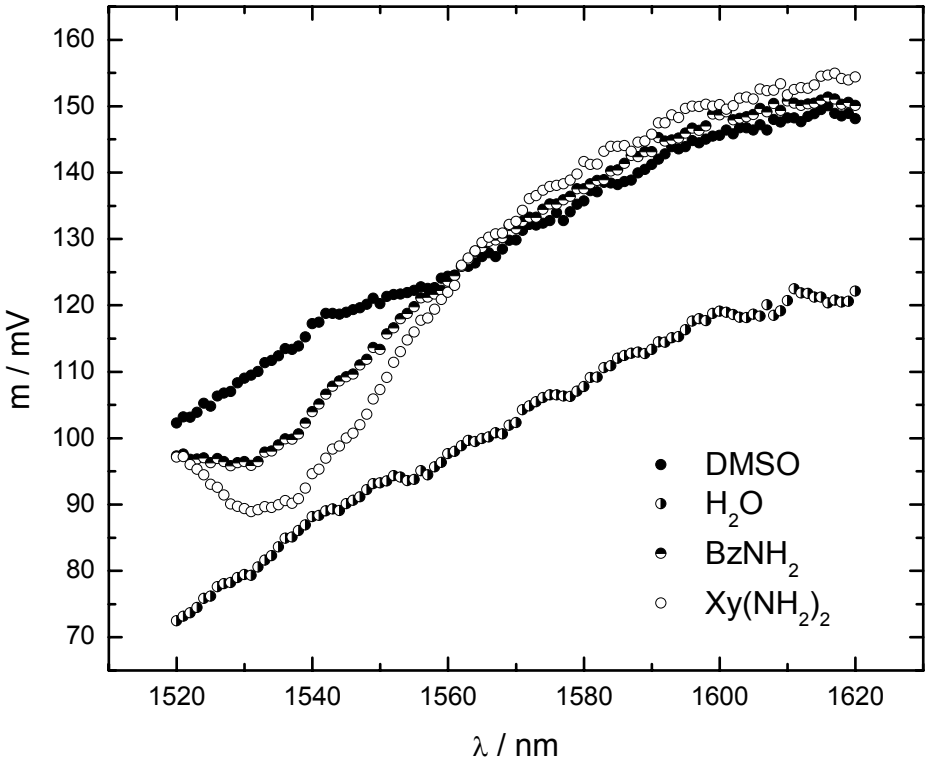

Figure 5.2: Modulation spectra of water, DMSO, $BzNH_2$, and $Xy(NH_2)_2$.

One immediately notes the prominent peaks centred near 1535 nm for both amines. This is exactly where one would expect to see the first vibrational overtone for N-H.[4] Recall from Chapter 2 that optical absorption should lead to a shorter ringdown time and hence a larger modulation depth. Here the modulation depth shows the opposite trend than expected. This behaviour was also observed in Chapter 4 when broadband amplified spontaneous emission was the major contributor to the intensity striking the detector. That this reversed trend in *m* is again observed may indicate that just as before there is some component of "direct light". As mentioned in the introduction to this chapter, ASE

is not expected to be the culprit in this case since it should be attenuated to the same extent as the laser light due to the broadband nature of the loop. The most likely cause is laser light in the fibre cladding. By making reference to equation (3.18) one can estimate that for a 75 μm sample gap, 16 % of the light leaving the transmitting fibre strikes the core of the receiving fibre, with the remaining 84 % being incident on the cladding. Thus cladding modes may be excited upon traversing the sample gap. In Chapter 3 it was shown that over 80 m of fibre the cladding modes will be almost completely attenuated, with the light either lost to absorption and scattering or coupled to core modes. Here the length of fibre is much less (~ 11 m) so light will almost certainly still be present in the cladding when it encounters the output coupler leading to the detector. It is not known what the coupling coefficient for cladding modes passing though the FFEF coupler is. However, one can estimate that it is quite high since in the coupler the claddings of the two fibres are fused together. Light entering the coupler in the cladding is subjected to a new mode structure due to the new boundary conditions imposed by the fused geometry. The intensity will be redistributed according to the new mode structure and it can be envisioned that upon leaving the coupler, half the cladding mode intensity will remain in the loop with the other half being directed to the detector. Therefore, the combination of cladding mode excitation at the sample gap and a high coupling efficiency of those modes out to the detector is the most likely source of "direct light" responsible for a reversal in the trend of modulation depth upon increasing absorption. This result stresses the

importance of using two confocal lenses separated by $2l_f$ to constrain the light solely to the core.

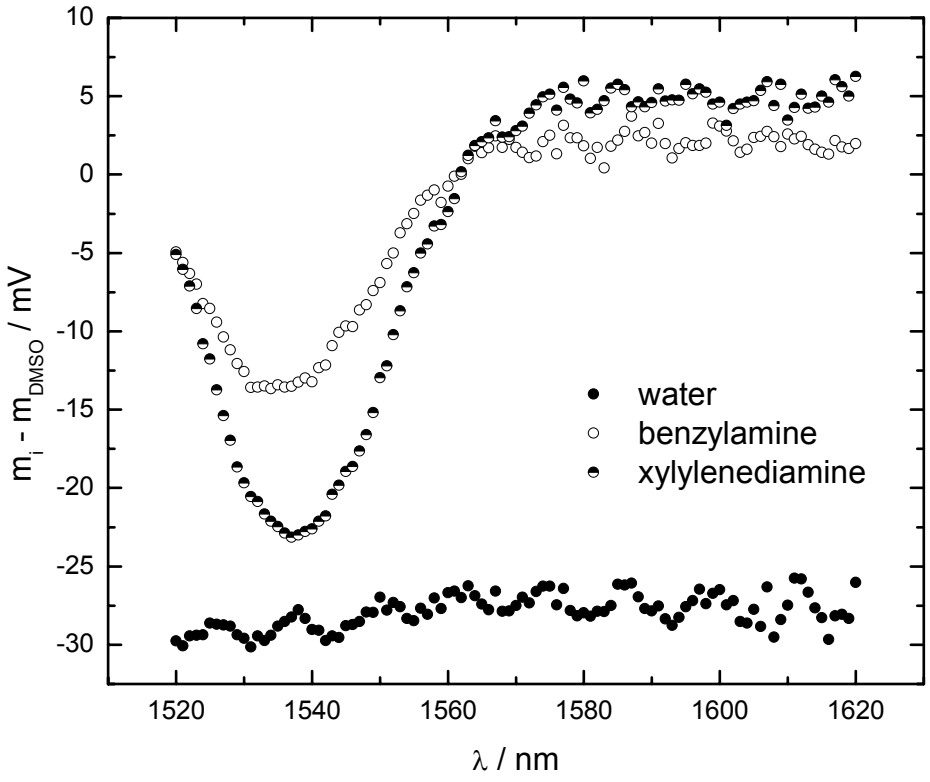

Figure 5.3: Modulation spectra with DMSO baseline subtracted.

The spectra in Figure 5.3 can still be interpreted in terms of the modulation depth *m* being directly proportional to the transmitted intensity, rather than being dependent on the ringdown time. At long wavelength *m* for both amine is greater than *m* for DMSO since they have higher refractive index, resulting in greater transmission. Water has a low RI and small absorption coefficient but high concentration and consequently the value of *m* is smaller compared to DMSO. The cause of oscillations in the spectra is unknown (for

water the period is ~ 11 nm). Additivity of absorption due to the N-H stretching overtone, once weighted for the concentration, can be noted. The weighted ratio of the peak heights is 2.04:1 for xylylenediamine relative to benzylamine. The detection limits (at 2σ of the baseline noise for comparison to the result of Lehmann et al.) for the amines were determined to be εC_{DL} = 371 cm^{-1} for the monoamine and εC_{DL} = 395 cm^{-1} for the diamine, or 670 and 360 mM, respectively. For water, the detection limit is εC_{DL} = 456 cm^{-1}, corresponding to 6500 mM or 13 % by volume in DMSO. These results are summarized in Table 5.1.

Table 5.1: Detection limits determined from the modulation spectra.

	C / M	ε / M cm^{-1}	εC / cm^{-1}	DL / mM	εC_{DL} / cm^{-1}
DMSO	14.08	0	0	n/a	n/a
H_2O	55.5	70	3885	6500	456
$BzNH_2$	9.16	550	5038	670	371
$Xy(NH_2)_2$	7.58	1100	8414	360	395

5.2.2 Phase shift spectra

Phase spectra were also recorded, and Figure 5.4 shows the spectra for the two amines after subtraction of the DMSO spectrum and smoothing with a 5 point moving average.

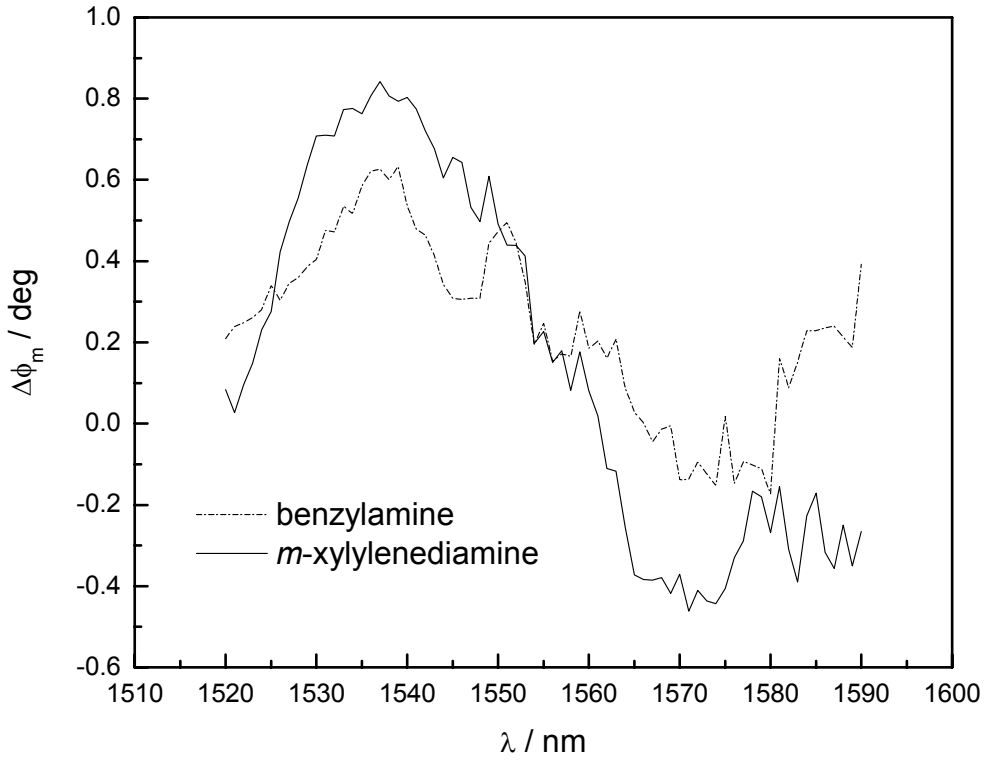

Figure 5.4: Phase spectra for the two amines.

The noise in both spectra after smoothing is still quite large, however a peak in both is discernible near 1535 nm. Again the peak height for the diamine is greater than that for the monoamine in accordance with their ε values. The cladding modes are expected to contribute a small but constant angle to the overall phase, while any variation in ϕ_m in the spectra above is expected to be from the changing ringdown time of the core mode with absorption. Both ϕ_m and $\Delta\phi_m$ are small since the cladding modes make the largest contribution to the light intensity striking the detector. Comparison of the phase and modulation spectra highlights that while the modulation may be dependent on the stability of the light source and detector, it can be easily amplified.

The values of εC_{DL} obtained here are larger than the one reported by Lehmann et al. owing to the long sample gap used. With a lensed fibre and an optimized gap length to improve performance our values can likely be reduced beyond theirs. It should be noted that we obtained the standard error for the amines from the baseline noise of the spectra in Figure 5.3 away from the absorption feature whereas Lehmann et al. use the standard error on the ringdown time for 16 decays. For proper comparison we should use the standard error on the modulation depth for 16 measurements. Unfortunately the design of the data acquisition and processing program is such that the values of the individual measurements are discarded, the standard error is not calculated, and only the 50-measurement average is retained.

5.3 Conclusion

We demonstrated for the first time a fibre-loop ringdown spectrometer for direct probing of small liquid volumes by near infrared light (1520 to 1620 nm), though we did quite the botch job of it. The modulation depth followed the opposite trend than the one expected. This was likely due to light travelling directly from the laser to the detector in the form of cladding modes excited at the sample gap and coupled with high efficiency out to the detector. The cause of this complication was the inappropriately long separation distance at the sample interface, which was chosen in an attempt to provide a low detection limit without paying heed to the consequential redistribution of light among the core and cladding. The detection limits are unsurprisingly comparable to those

achieved using an FBG cavity (see Chapter 4) where the majority of light also passed straight from the laser to the detector but in that case under the guise of ASE. These results emphasize the need to confine the light to the core mode as much as possible – something that can be achieved with the use of confocal lenses described in Chapter 3. As an alternative, one could use a longer loop to attenuate the cladding modes before they reach the output coupler, however this would lead to a higher loss per pass than the use of microlenses.

In the future the use of an appropriately configured sample interface will likely afford much improved detection limits for model absorbers such as the amines used. The additivity of absorption with the number of amine groups bodes well for the extension of NIR-FLRDS to the detection of biomolecules containing many N-H bonds. Single cell detection via scattering as well as absorption is also a possible extension, especially for large cells (of diameter 10 μm or greater) which can completely occlude the light path when passing through the sample interface.[5]

5.4 References

1. Tarsa, P. B.; Rabinowitz, P.; Lehmann, K. K., Evanescent field absorption in a passive optical fiber resonator using continuous-wave cavity ring-down spectroscopy. *Chemical Physics Letters* **2004,** 383, (3-4), 297-303.

2. Tarsa, P. B.; Wist, A. D.; Rabinowitz, P.; Lehmann, K. K., Single-cell detection by cavity ring-down spectroscopy. *Applied Physics Letters* **2004,** 85, (19), 4523-4525.

3. Li, R. K.; Loock, H. P.; Oleschuk, R. D., Capillary Electrophoresis Absorption Detection Using Fiber-Loop Ringdown Spectroscopy. *Analytical Chemistry* **2006**.

4. Buback, M.; Vögele, H. P., *FT-NIR Atlas*. VCH Publishers: Weinheim, 1993.

5. Li, R. Fiber-loop ring-down spectroscopy - a novel online detection method. Queen's University, Kingston, 2007.

Chapter 6 Fibre loop ringdown spectroscopy at 800 nm

A number of reports from our laboratory have demonstrated the ability of FD-FLRDS to attain higher time resolution and lower detection limits than a similar time domain implementation.[1, 2] All these apparatus were quite similar, using a multimode fibre and an excitation wavelength of ~ 800 nm. Now equipped with an FD model for biexponential decays (see Chapter 2) we seek to more fully characterize such a system.

6.1 Frequency domain fibre loop ringdown spectroscopy system

A 110 m – long multimode optical fibre (AS100/140 IRPI, Fibretech Optica Inc.) was used to make a fibre loop. The two fibre ends were placed in a capillary-fibre interface. The receiving end was flat cut and the transmitted end was melted into a hemispherical microlens with a radius of curvature of ~ 76 μm.[2] The distance between the microlens and the flat cut end was measured to be 33μm using a microscope (built from commercial components: 700x optical zoom, Digital Color CCD 1V-CCAM2, Edmund Optics). A syringe pump (Havard Apparatus pump II) was used to pump the dye through the capillary-fibre interface at a flow rate of 110 μL / min.

To record time domain ringdown transients, 100 ns square pulses at a repetition rate of 1 kHz from a LeCroy 9100 function generator were applied to a laser diode driver to generate ~ 200 ns pulses from a laser diode (JDS Uniphase SDL-2372-P1, 810 ± 3 nm, maximum 2W). The pulses were coupled into the loop as described below.

For frequency domain experiments, the output of the intensity-modulated *cw* diode laser was coupled into the loop. Two sine waves with identical frequency and phase were produced using the function generator. One was used as the reference for the lock-in amplifier (Stanford Research Systems SRS 844), while the other one was applied as current modulation for the laser diode. The modulation current of the input is kept above the threshold of the emission and below the permissible maximum current to reduce signal distortion (1.5 to 3.5 V applied to the driver). A 2x2 fused fibre evanescent field (FFEF) coupler (Lightel Technologies Inc., Kent, WA) with a splitting ratio of 99:1 was spliced into the 110 m fibre loop to allow for coupling of the laser light into the loop (total length 112 m). The loss associated with the two fusion splices (0.09 dB = 2.1 %) was estimated from previous measurements[1], while the splice quality determination provided by the fusion splicer (Furukawa Electric Co. Ltd) served as a rough guide. The insertion loss of the 2x2 coupler was not specified by the manufacturer but is likely near 2.3 % per pass (0.1 dB). A photomultiplier tube (PMT; Hamamatsu 950) was placed against the fibre loop few meters away from the 2x2 coupler and monitored the light scattered from the fibre. The PMT signal was then fed into the lock-in amplifier and referenced to the driving current of the laser diode. To reduce electromagnetic interference, all cables were shielded. Phase data was digitized using a DAQ card (DAQ PCI-6024E National Instruments) and stored on the computer. Time domain data was collected on the oscilloscope (Tektronix TDS 3032), averaging 512 acquisitions and transferred to PC via GPIB.

The laser output spectrum was recorded using an optical spectrum analyzer (OSA, Agilent 86140B) and is shown in Figure 6.1.

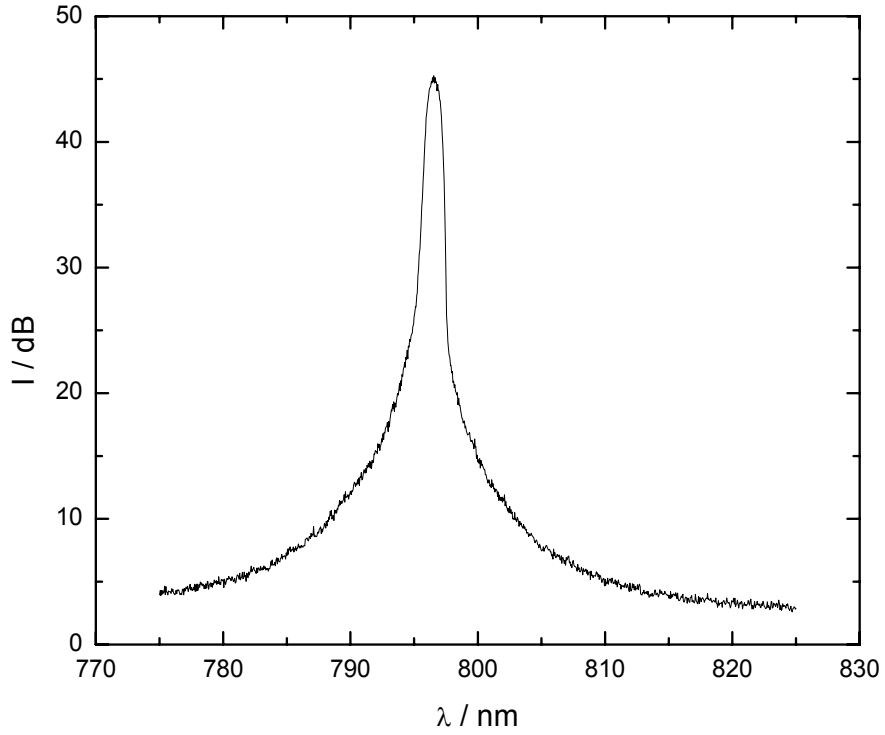

Figure 6.1: Diode laser emission spectrum.

The FWHM was found to be 1.1 nm and the peak centre to be 796.6 nm. There is a very small contribution from broadband amplified spontaneous emission (ASE) but it is > 10^4 less intense than the laser line so may be considered negligible. (The peak power corresponds to 730 μW.)

The dye 2-[2-[2-chloro-3-[(1,3-dihydro-3,3-dimethyl-1-(4-sulfobutyl)-2*H*-indol-2-ylidene)ethylidene]-1-cyclopenten-1-yl]ethenyl]-3,3-dimethyl-1-(4-sulfobutyl)-3*H*-indolium (ADS805WS) was purchased from American Dye Source, Inc (Baie D'Urfe, PQ, Canada) and used without any further purification. The dye's absorption coefficient

is given by the manufacturer as ε' = 1.6 x 10^5 L mol^{-1} cm^{-1} so that $\varepsilon = \ln(10)\varepsilon'$ = 3.7 x 10^5 L mol^{-1} cm^{-1}.

Solutions of the dye ADS805WS were made in distilled water following a roughly logarithmically increasing trend in concentration. For each dye concentration the modulation frequency of the laser was stepped from 50 to 500 kHz in 50 kHz steps. At each frequency the phase angle was averaged over 5.5 s at a sample rate of 10 Hz – each data point in Figure 6.3 represents a 55-point average.

6.2 Results and Discussion

Time domain short-pulse excitation of the loop was used to obtain the cavity length from the round-trip time and to determine the ringdown time(s) for the system. Figure 6.2 shows the ringdown transient with water in the sample interface. The envelope of the decay is constructed from the peaks in the transient. The average round-trip time (t_r) was found to be 547 ns corresponding to a length of 112 ± 3 m (20-point average, 1σ error). A fit to the envelope with a biexponential model yields ringdown times of 1.12 ± 0.06 μs and 210 ± 20 ns with α_1 = 0.394 (R^2 = 0.99988).

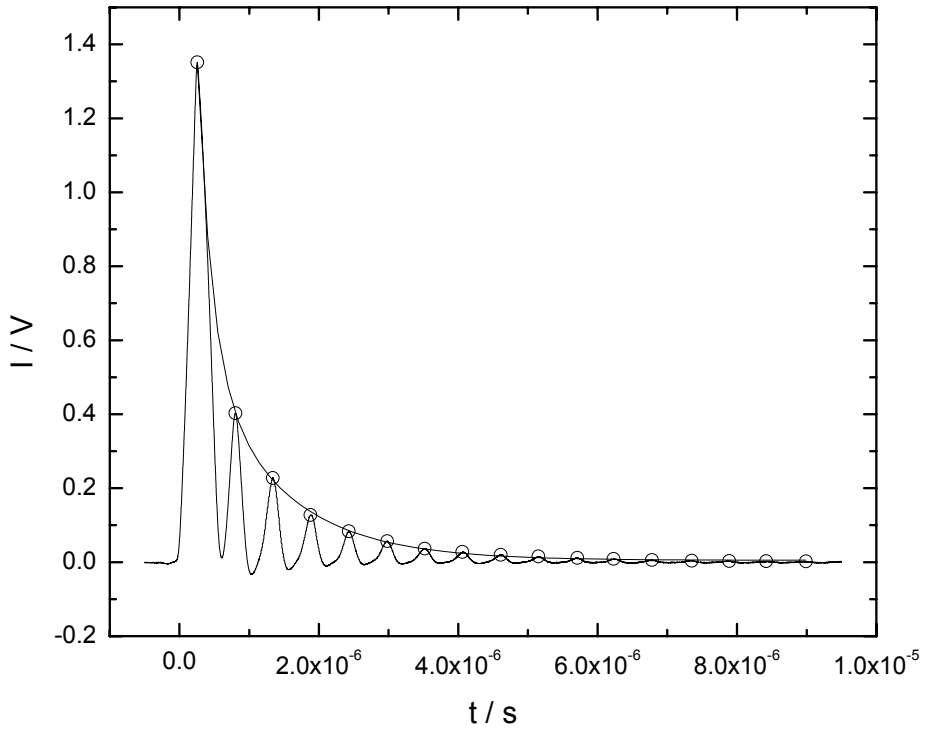

Figure 6.2: Fibre loop output under short pulse excitation. A biexponential function is fit (curved line) to the envelope (open circles) of the data (solid line).

Prior results using a multimode fibre loop also showed a biexponential decay due to light in core and cladding modes.[3, 4] The ratio of τ_{core} to τ_{clad} was reported as 7:1 and 4:1 in the previous publications. These values are consistent with the ratio of 5:1 found in the present work.

In the first demonstration of phase shift FLRDS the authors performed a fit to the measured phase vs. concentration with a single exponential model, using the phase offset, transmission, and gap size a fitting parameters.[1] We follow the same example, and apply a biexponential model in correspondence with the time domain fitting results. To model the two concurrent decays we use the equation

$$\phi_m = \phi_o - \arctan\left(\frac{\frac{\omega\alpha_1\tau_1}{1+\omega^2\tau_1^2} + \frac{\omega(1-\alpha_1)\tau_2}{1+\omega^2\tau_2^2}}{\frac{\alpha_1}{1+\omega^2\tau_1^2} + \frac{(1-\alpha_1)}{1+\omega^2\tau_2^2}}\right) \tag{6.1}$$

where the ringdown time for the core modes is given by

$$\tau_1 = \frac{n_1 L}{c_o\left(-\ln(T_1) + \varepsilon_1^{coupler} + \varepsilon_1 L + \varepsilon dC\right)} = \frac{t_{r1}}{\Gamma_1 + \varepsilon dC} \tag{6.2}$$

and for the cladding modes

$$\tau_2 = \frac{n_2 L}{c_o\left(-\ln(T_2) + \varepsilon_2^{coupler} + \varepsilon_2 L + \varepsilon dC\right)} = \frac{t_{r2}}{\Gamma_2 + \varepsilon dC} \tag{6.3}$$

The round-trip times t_{ri} and absorption coefficient ε are held constant, while the loss parameters Γ_i, the gap size d, the steady-state intensity α_1, and the phase offset ϕ_o are allowed to vary as fitting parameters. The loss terms for the transmission across the gap, the insertion loss of the coupler, and the fibre material loss are grouped together as

$$\Gamma_i = -\ln(T_i) + \varepsilon_i^{coupler} + \varepsilon_i L \tag{6.4}$$

since the material loss and coupler insertion loss for the cladding modes is not known. The experimental data together with the result of the fit are displayed in Figure 6.3 and the parameter values are listed in Table 6.1.

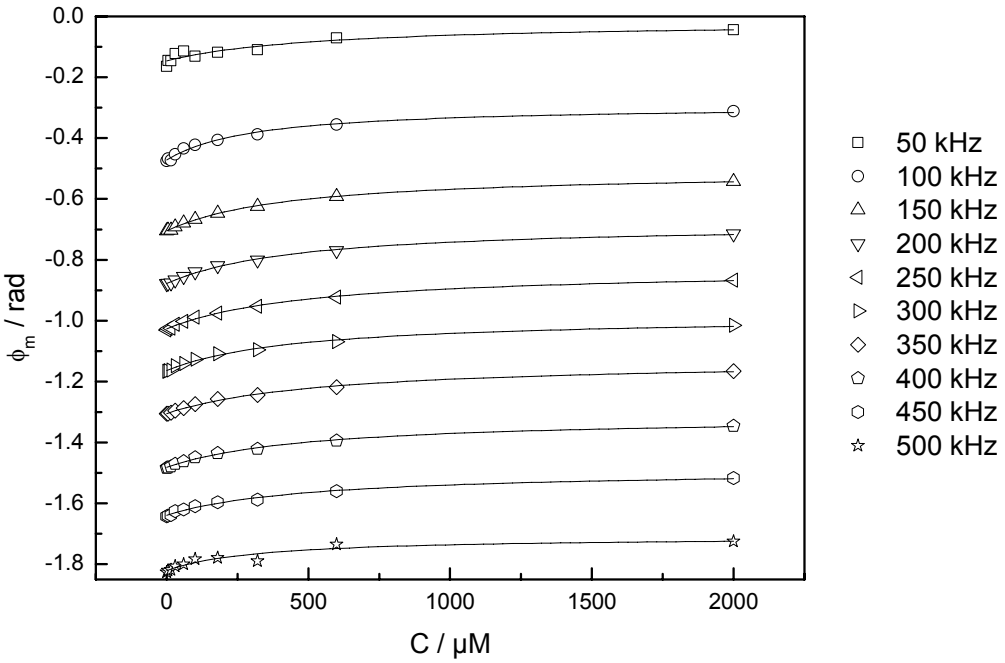

Figure 6.3: Fit of the FD data to a biexponential model.

The symbols plot the data while the solid lines show the fit for each frequency.

Table 6.1: Parameter values obtained from a biexponential fit to the FD data.

f / kHz	ϕ_o / rad	d / μm	α_1	Γ_1	Γ_2	R^2
50	-0.013	54	0.106	0.436	1.585	0.892
100	-0.286	127	0.221	0.671	2.941	0.991
150	-0.502	127	0.251	1.100	3.837	0.999
200	-0.673	158	0.247	1.390	5.155	0.998
250	-0.822	183	0.277	1.988	6.327	0.996
300	-0.980	261	0.217	2.150	8.496	0.993
350	-1.122	250	0.207	2.551	9.632	0.996
400	-1.307	328	0.198	2.983	11.502	0.996
450	-1.483	410	0.162	3.362	14.023	0.991
500	-1.706	989	0.085	3.202	19.714	0.915

Though the quality of the fits is quite good (i.e. R^2 is close to 1) the error on the parameters (not shown) is quite large, in some cases larger than the value itself.

Next, as a comparison to the previously published method, a fit of the data to a single exponential model was performed. This fit utilized the equation

$$\phi_m = \phi_o - \arctan\left(\frac{\omega t_r}{\Gamma + \varepsilon d C}\right) \tag{6.5}$$

where the round-trip time was that for the core modes. The resultant parameter values are tabulated in Table 6.2.

Table 6.2: Parameter values obtained from a single exponential fit to the FD data.

f / kHz	ϕ_o / rad	d / μm	Γ	R^2
50	-0.016	64	1.31	0.891
100	-0.291	168	1.87	0.989
150	-0.508	163	2.57	0.999
200	-0.680	204	3.40	0.997
250	-0.828	228	4.25	0.996
300	-0.986	342	5.70	0.992
350	-1.129	330	6.73	0.996
400	-1.314	433	8.07	0.995
450	-1.489	547	10.21	0.989
500	-1.709	1265	15.16	0.911

The phase offsets determined using the two models differ from each other only by as much as 6.8 x 10^{-3} rad, or 0.39 degrees. A worrying feature in the fitting results for both models is that d and Γ_i increase with frequency. These parameters are frequency independent, and so should be identical for all frequencies. The obvious question to ask is why does this seeming dependence arise. Examination of the data in Figure 6.3 reveals that at each frequency the shape of the curve and the span of the data ($span = \phi_m(C = 2mM) - \phi_m(C = 0mM)$) is very similar. In other words the curves are nearly identical other than their positions along the y-axis. The vertical positions of the

curves are determined solely by their phase offsets. For the shape and span of the curves to remain the same as the frequency increases, the loss parameter and the gap size must increase. Thus the invariance in shape and span gives rise to the seeming dependence of d and Γ_i on ω. Attempting to fit the data with the gap fixed at 33 μm gave very large errors on the parameters and Γ_i still varied with frequency.

To understand the source of this complication we used equation (6.1) to simulate phase angles at different modulation frequencies and absorber concentrations. The simulation of ϕ_m using the ringdown times determined in the time domain (above) and the phase offsets obtained from the fit to a biexponential model (Table 6.1) clearly shows that the span increases with frequency. The simulation parameters Γ_1 and Γ_2 were obtained from the TD ringdown times for $C = 0$ and were set to 0.485 and 2.58, respectively. The steady-state intensities are also known from the time domain (above). The gap size (d = 33 μm) was determined from a micrograph using the fibre's diameter (140 μm) as reference. Using these constant values, the simulation shown in Figure 6.4 was generated.

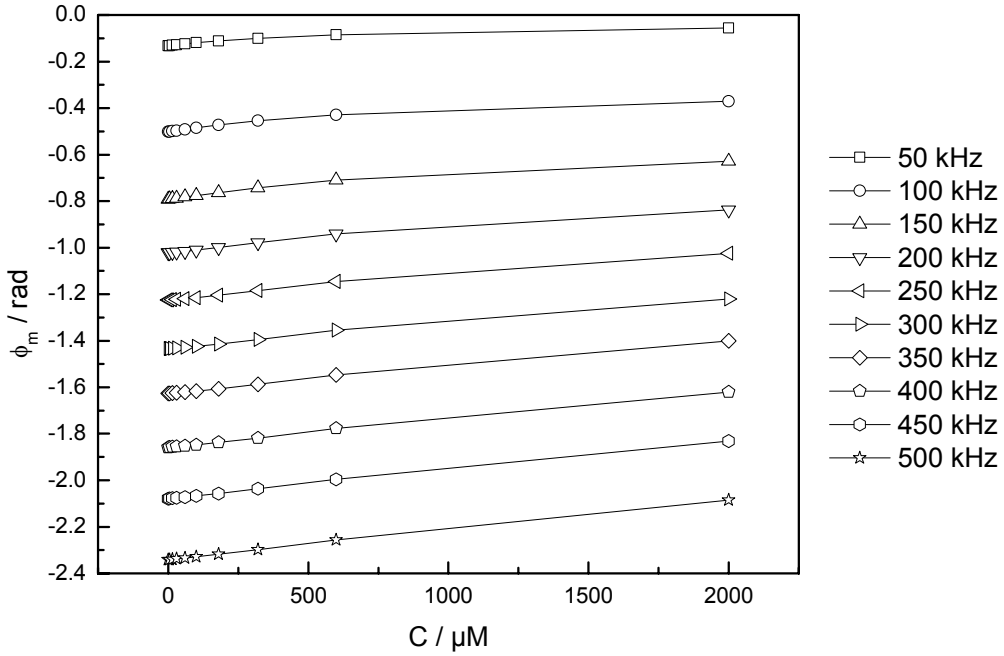

Figure 6.4: Simulation of the measured phase angle.

This simulation uses values of α_1, Γ_1 and Γ_2 from the TD and ϕ_o from the biexponential fit.

Comparison between Figure 6.3 and Figure 6.4 reveals that the discrepancy between the data and simulation becomes larger with increasing frequency.

An even more illustrative comparison is that between plots of $\tan(\phi_m - \phi_o)$ vs. ω generated from the FD data and fitting results, and simulated from the TD fitting results. For the simulation, the true phase angle can be calculated directly without making any assumptions about the phase offset. These plots are shown on the same scale in Figure 6.5 to emphasize their differences.

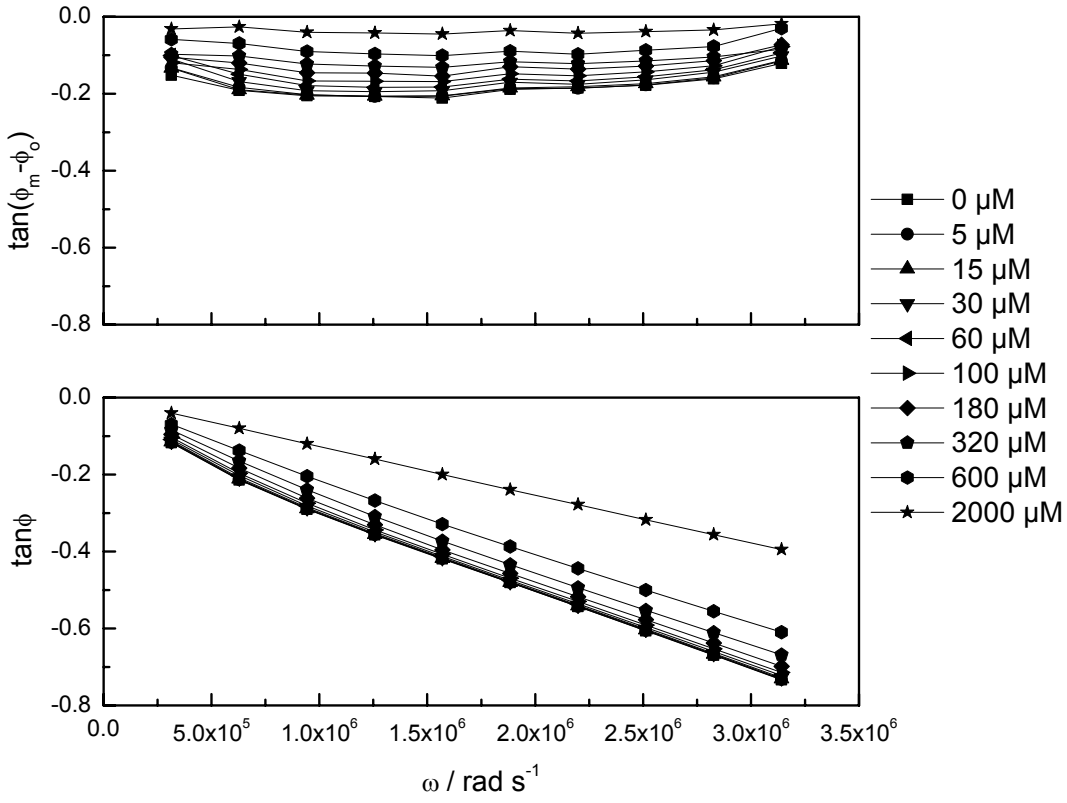

Figure 6.5: Comparison of the FD results and simulation.

The upper plot (a) shows the tangent of the experimental FD data corrected by the phase offset obtained from fitting. The lower plot (b) shows tanϕ calculated from the τ's and α's obtained in the time domain experiment.

The shape of the curves in the upper plot of Figure 6.5 suggests the presence of another decay process with a very fast ringdown time. Since the core and cladding mode decays have been accounted for and ASE is not a complicating factor in a broadband resonator, there must be some other source of this decay. The most plausible cause is electrical interference from the diode laser affecting the signal from the PMT. The diode laser had earlier been noted to produce a large amount of electrical interference. Before the above experiments were conducted all cabling was covered with extra shielding, the PMT was housed in a shielded box, and the PMT itself was covered in an additional layer of

shielding. Nevertheless the results above suggest some interference was still occurring. Interference would result in a small, constant phase contribution that would shift ϕ_m to smaller angles than expected.

There are two other potential sources of error, but they are not believed to be the cause of the curve shapes in Figure 6.5a. One is slight saturation of the PMT. The PMT was operated at the highest gain possible without noticeable saturation, but with variation in the high voltage power supply by ± 7 V, it is possible some saturation occurred. However in another experiment where slight saturation was occurring, the measured phase was observed to be much larger than expected – i.e. saturation shifts ϕ_m in the opposite direction of the curves in Figure 6.5a. Another complication could be the presence of harmonic frequencies in the laser output waveform. In recent work, Fourier transform of the output waveform reveals that harmonics contribute ~ 10 % of the total intensity.[†] However, any high frequency content was expected to be successfully filtered out by the narrow bandpass filter (24 dB / octave) of the lock-in amplifier. Thus interference seems to be the only likely source of the observed behaviour.

Since we have surmised the presence of an additional "decay", the data in Figure 6.5a was fit to a triexponential model, keeping τ_1 and τ_2 constant and allowing α_1, α_2, and τ_3 to vary. The model is given by the equation

[†] Performed by Klaus Bescherer.

$$\tan\left(\phi_m - \phi_o\right) = \frac{\dfrac{\omega\alpha_1\tau_1}{1+\omega^2\tau_1^2} + \dfrac{\omega\alpha_2\tau_2}{1+\omega^2\tau_2^2} + \dfrac{\omega\left(1-\alpha_1-\alpha_2\right)\tau_3}{1+\omega^2\tau_3^2}}{\dfrac{\alpha_1}{1+\omega^2\tau_1^2} + \dfrac{\alpha_2}{1+\omega^2\tau_2^2} + \dfrac{\left(1-\alpha_1-\alpha_2\right)}{1+\omega^2\tau_3^2}} \tag{6.6}$$

The results of this fit are given in Figure 6.6 and Table 6.3.

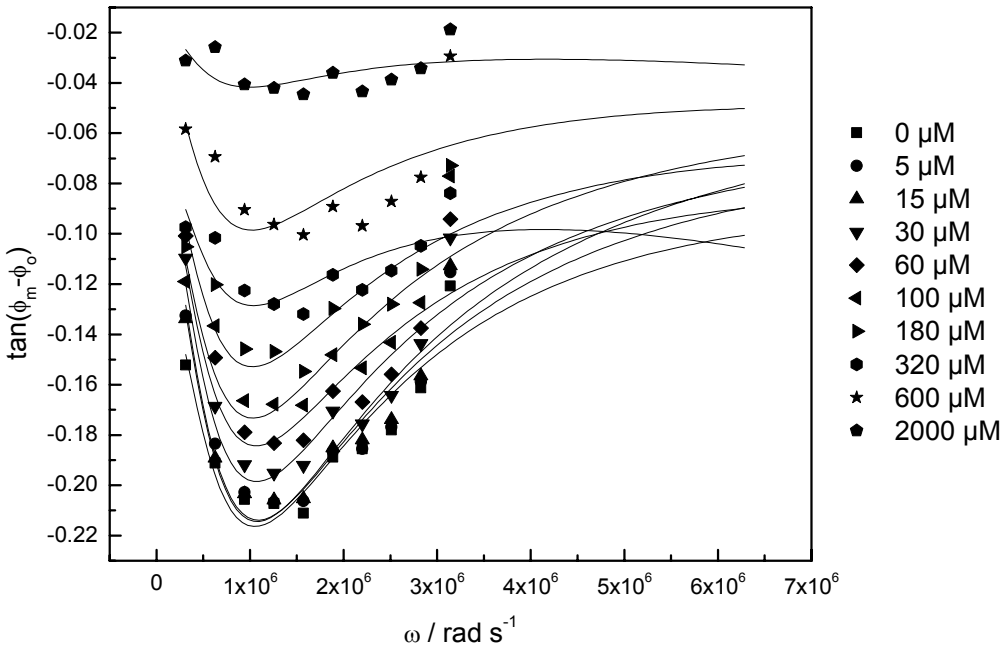

Figure 6.6: Triexponential fit after subtraction of the phase offset.

The steady-state amplitude of the decay thought to be caused by interference increases with concentration. Also the quality of the fit decreases with increasing dye concentration (as evidenced by R^2). This indicates that as the light intensity reaching the detector decreases and interference becomes dominant our model no longer describes the process occurring. This is not surprising since interference should not be bound by our model.

Table 6.3: Parameter values for triexponential fit.

C / μM	α_1	α_2	α_3 †	τ_3 / ns	R^2
0	0.258	0.215	0.527	4.86	0.843
5	0.302	0.109	0.590	2.88	0.857
15	0.298	0.123	0.579	1.26	0.875
30	0.287	0.100	0.613	2.57	0.850
60	0.266	0.100	0.634	4.97	0.792
100	0.251	0.111	0.638	2.14	0.680
180	0.227	0.094	0.678	4.07	0.649
320	0.170	0.140	0.689	11.19	0.536
600	0.174	0.000	0.826	3.36	0.443
2000	0.071	0.020	0.909	3.49	0.220

† Calculated from $\alpha_3 = 1 - \alpha_1 - \alpha_2$.

The postulated interference does not seem to have a large effect on ϕ_m at the low frequencies used in previous experiments,[1, 2] thus if it was present then it would not have been evident from the data. Also shown in the single- and bi-exponential fits, allowing the gap size and loss to vary ensures that a good fit is obtained, however these values may not reflect the true values obtained by other means (i.e. TD determination and microscopy). In the previous experiments where the gap size could not be measured due to the design of the sample interface, the fit result may not be accurate.

Finally, even with the likely presence of interference, we can make an estimate of the detection limit for the apparatus. Determined from 3σ of the baseline noise (55 data points) for distilled water, the detection limit is 0.76 μM (εC_{DL} = 0.28 cm^{-1}) at f = 250 kHz, an improvement by a factor of ~ 10 over previous results.[2]

6.3 Conclusion

To fully characterize a multimode fibre loop excited with 800 nm radiation, the phase angle was measured for ten frequencies at ten dye concentrations. Single- and bi-exponential models were fit to the data to extract the phase offset at each frequency. The loss parameter(s) and gap size which should be constant with frequency were found to vary. This pointed towards the presence of another "decay" process besides core and cladding decays observed in the time domain. The cause of this decay was hypothesized to be electrical interference from the diode laser affecting the PMT, resulting in a smaller value of ϕ_m than predicted. The data corrected for the phase offset were fit using a triexponential model to try to capture the effect of the interference. At high dye concentrations, when the proportion of light to interference is low, our model no longer adequately describes the signal arriving at the lock-in amplifier.

In the future, experiments could be preformed to verify that interference is the culprit, and if it is every effort should be made to eliminate it. An advantage of using optical fibre is that the diode laser need not be positioned close to the rest of the apparatus, and could be easily moved to a location where it poses no problems. Once the cause of the observed behaviour is resolved (be it interference or otherwise) the above experiment could be repeated in order to achieve our goal of fully characterizing the system.

6.4 References

1. Tong, Z. G.; Wright, A.; McCormick, T.; Li, R. K.; Oleschuk, R. D.; Loock, H. P., Phase-shift fiber-loop ring-down spectroscopy. *Analytical Chemistry* **2004,** 76, (22), 6594-6599.

2. Li, R. K.; Loock, H. P.; Oleschuk, R. D., Capillary Electrophoresis Absorption Detection Using Fiber-Loop Ringdown Spectroscopy. *Analytical Chemistry* **2006**.

3. Brown, R. S.; Kozin, I.; Tong, Z.; Oleschuk, R. D.; Loock, H. P., Fiber-loop ring-down spectroscopy. *Journal of Chemical Physics* **2002,** 117, (23), 10444-10447.

4. Tong, Z. G.; Jakubinek, M.; Wright, A.; Gillies, A.; Loock, H. P., Fiber-loop ring-down spectroscopy: A sensitive absorption technique for small liquid samples. *Review of Scientific Instruments* **2003,** 74, (11), 4818-4826.

Chapter 7 FLRDS at 405 nm

Many molecules have a large absorption coefficient ($\varepsilon > 10^4$ L mol^{-1} cm^{-1}) in the ultraviolet and visible portion of the spectrum. For example DNA and RNA have strong absorption features near 250 nm, while many proteins show optical absorption at about 280 nm and extending into the 400 nm region.[1] Performing fibre-loop ringdown sensing of analytes in this region may therefore provide lower detection limits than other spectral regions, especially the near infrared (NIR) where absorption coefficients are much smaller ($\varepsilon < 300$ L mol^{-1} cm^{-1} per bond[2]). A label-free detection limit comparable to that obtained at 800 nm is expected (Chapter 6). However, the best fibre optics for the UV-Vis range have large material losses compared to NIR fibres. A typical value for multi-mode fibre is 70 dB / km at 400 nm, whereas in the NIR fibre may have losses as low as 0.22 dB / km at 1550 nm. Therefore, UV-Vis-FLRDS is only feasible if one uses a short loop that minimizes the scattering losses.

An FLRDS apparatus was combined with a 405 nm laser light source to test the viability of these measurements using currently available technology. An operating wavelength of 405 nm was chosen since there exist comparably high power (60mW) and lost cost ($2000) *cw* diode lasers. Shorter wavelength diode lasers (375 nm) have lower power and shorter operating lifetimes and presently do not offer advantages over diodes operating at slightly longer wavelengths. Numerous molecules show strong absorption features at 405 nm, especially ones containing heme-like groups and porphyrin rings. The absorption coefficient can be as high as 10^5 to 10^7 L mol^{-1} cm^{-1} for these species.

Large core multimode fibre (100μm diameter) was chosen and consequently a large volume is probed (compared to using SMF). Multimode fibre allows for easier detection, since alignment is not as critical, and angle-coupling into the loop can be used. The coupling of (1) the laser to a delivery fibre, (2) the delivery fibre to the loop fibre, and (3) the coupling across the sample gap was optimized. The apparatus was then tested using myoglobin as an analyte.

7.1 Instrumentation

A 405 nm 60mW Nichia NDHV310APC laser diode (LD) was kept at a constant temperature using a Thorlabs LDM21 thermoelectric cooler (TEC). A Thorlabs IP250-BV LD controller controls both the laser and TEC. A microscope objective (Carl Zeiss, 10x, NA = 0.22) mounted on a translation stage (ThorLabs MBT616) and placed in front of the laser is used to focus the light and couple it into the delivery fibre. The fibre used for the delivery and loop is 100/110 μm MMF with NA = 0.22, which is matched to that of the objective to ensure good coupling (Newport F-MCB-T). Two detectors were used: a PMT (Hamamatsu 950, maximum response at ~ 400 nm) and a silicon photodiode (ThorLabs DET210). The LeCroy 9100 arbitrary function generator supplied the waveforms to the controller and lock-in amplifier (SR844), while the Tektronix TDS 3032 oscilloscope was used to measure intensities in optimizing the coupling.

7.2 Optimization of coupling and lensing of fibre

The optimization of coupling was begun with the coupling from the laser diode to the delivery fibre via the microscope objective. The objective was used in the opposite

sense than it would be in a microscope – it was used to collect the light from the laser and focus it down to a ~ 1mm diameter spot on the fibre facet. The fibre facet was cleaved flat and both the objective and fibre well cleaned to achieve the highest coupling. The end of the delivery fibre opposite the objective was also flat cleaved and was aligned with a detector (DET210) using a translation stage. Tuning the alignment on both ends until the maximum signal was reached, the intensity distribution was checked on a card and was observed to be a ring. Inspection of the microscope objective revealed a burn spot at its centre (due to previous experiments) that may be the cause of the ring intensity distribution. Changing the position of the fibre in the focus can yield a Gaussian intensity distribution but with lower signal amplitude.

A number of schemes for coupling from the delivery fibre to the loop fibre were investigated since commercial couplers for this fibre are not available. First, evanescent coupling between the fibres was tested using a ring intensity distribution in the delivery fibre (cf. CMI coupler, Chapter 3). The delivery and loop fibres were stripped over 6 cm and placed parallel and in contact over that length inside a 250 μm wide channel in an aluminum plate. A third fibre (diameter 100 μm) along with a PDMS coated Al top-plate were used to ensure contact (Figure 7.1). A drop of DMSO was added to the channel for index matching. This provided coupling of 0.35 %, determined from the ratio of the signal amplitude measured at the output of the loop and delivery fibres.

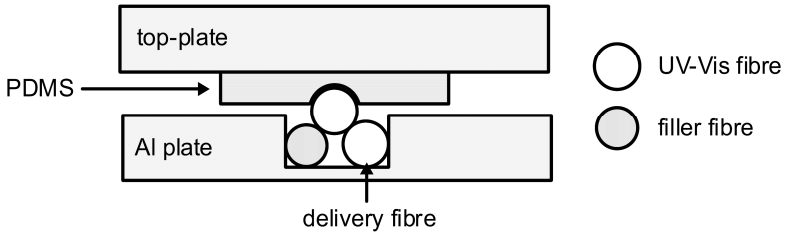

Figure 7.1: Evanescent coupling scheme for UV-Vis fibre.

The channel dimensions of the Al plate are 250 x 125 µm (W x H). The PDMS coated top plate and filler fibre ensure the delivery and loop fibres are in contact along their length.

Second, "angle-coupling" was tested using a Gaussian intensity distribution in the delivery fibre. The long axis of the delivery fibre was held at an angle of about 30^{o} to the axis of the loop fibre, with the two fibres coplanar (Figure 7.2). Light emitted from the delivery fibre is incident on the side of the stripped loop fibre and, with the help of DMSO for index matching, is coupled into the loop fibre. Coupling of 4.1 % was achieved.

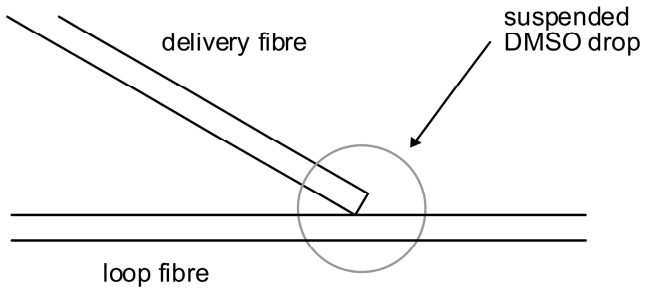

Figure 7.2: Illustration of angle-coupling method.

Light is coupled from a radiative mode of the delivery fibre to guided modes in the loop fibre, with the intervening space index-matched by DMSO.

Lastly, maximum coupling (25 %) was attained with the loop fibre stripped of its coating at the coupling point and curved with a bending radius of ~ 7 cm. The delivery and loop

fibres were aligned using a 2D translation stage, with a suspended drop of DMSO providing index matching (Figure 7.3).

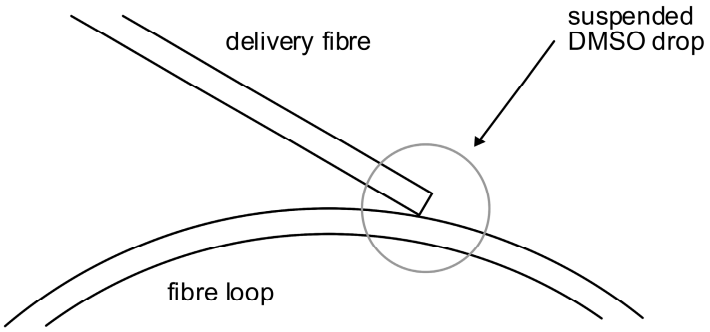

Figure 7.3: Illustration of bent-angle-coupling method.

The loop fibre is curved with a bending radius of ~7 cm to permit more light to enter from the delivery fibre. The DMSO drop provides index matching to assist coupling of light between the two fibres.

Although the delivery fibre output followed a Gaussian distribution for both angle-coupling methods, the mode field distribution at the loop fibre output was found to be a ring. This suggests the angle-coupling results in excitation of high-order core modes or cladding modes. A ring distribution, with the majority of the intensity near the outer edge of the fibre, will obviously lead to very poor coupling across a gap in the loop. The divergent ring would likely miss the receiving fibre end entirely. To solve this serious problem a fibre lens was fabricated on the transmitting end of the fibre loop. As previously (Chapter 3), the fibre lens was made using an electric arc to melt the end face into a hemisphere. The intensity distribution was checked on a card after each arc until a satisfactory distribution was reached. The loop fibre now showed an approximate Gaussian mode profile at all distances, suggesting that the lens does not focus the ring

mode but mixes the modes to a new distribution. The maximum output intensity measured with the lens was lower than without, implying the lens causes additional scattering or reflection losses. Figure 7.4 shows the approximate intensity distributions with and without lensing. With an appropriate mode field distribution to ensure reasonable coupling across the sample gap, the performance of the Vis-FLRDS system can be tested.

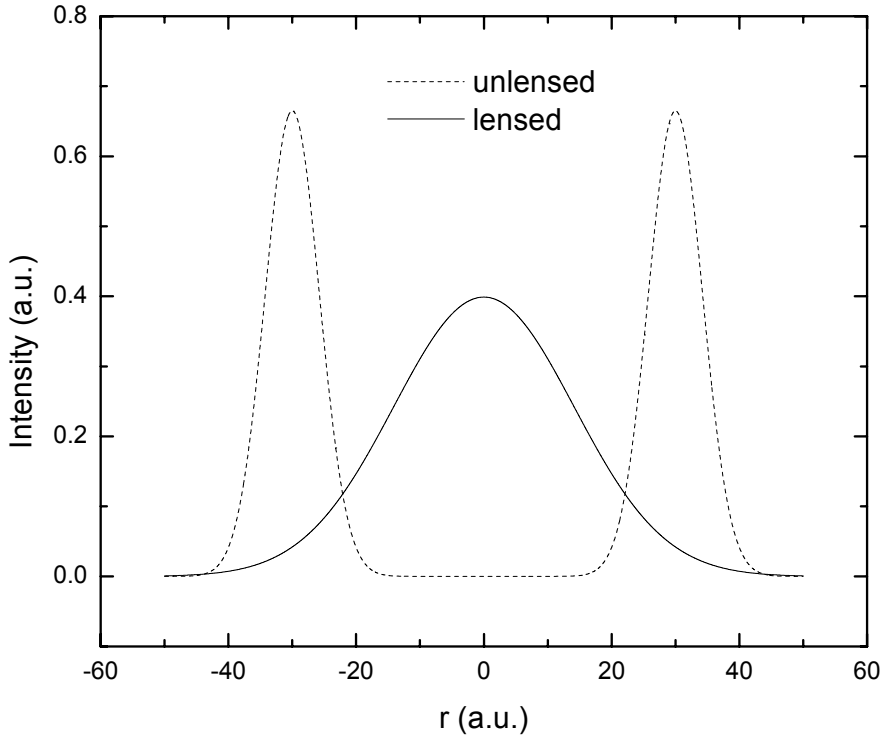

Figure 7.4: Approximate intensity distribution of the loop output with and without a lens.

A ring-shaped output distribution for the flat-cut fibre indicates high-order core modes or cladding modes are excited. Once lensed, the distribution changes to one that is roughly Gaussian.

7.3 Detection of myoglobin

Myoglobin, the primary oxygen carrier in muscle tissue, was chosen as the analyte to demonstrate the feasibility of Vis-FLRDS. It contains a heme-like group and has an

absorption coefficient of 1.16 x 10^5 L mol^{-1} cm^{-1} at 405 nm.[3] A schematic of the fibre loop sensor is given in Figure 7.5.

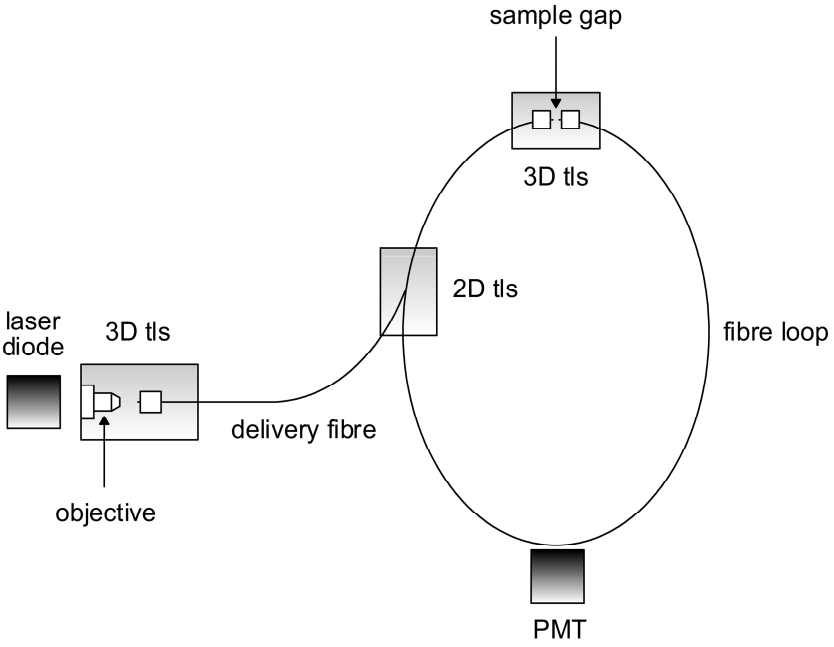

Figure 7.5: Illustration of the Vis-FLRDS apparatus.

Alignment at the coupling points (laser to delivery fibre, delivery fibre to loop, across sample gap) is performed using xyz (3D) or xy (2D) translation stages (tls). Index-matching at the coupling point is provided by a suspended drop of DMSO. A drop of sample is also suspended from a pipette and introduced in the sample gap.

The coating was stripped from the fibre where it was bent past the PMT to increase the intensity of light scattered. The length of the loop is approximately 2 m.

With the optimized system (i.e. bent-angle-coupling and a fibre lens (R ~ 115 μm) at the sample gap of ~ 70 μm) and the laser modulated at 80 kHz, a drop of water was suspended from a pipette in the sample gap and the phase angle measured at 10 Hz for ~18 s. Then a drop of aqueous myoglobin (Mb) solution (approximately 200 μM) was suspended in the sample gap and the phase angle again recorded for 1800 points. A histogram showing the distribution of phase angles measured is shown in Figure 7.6.

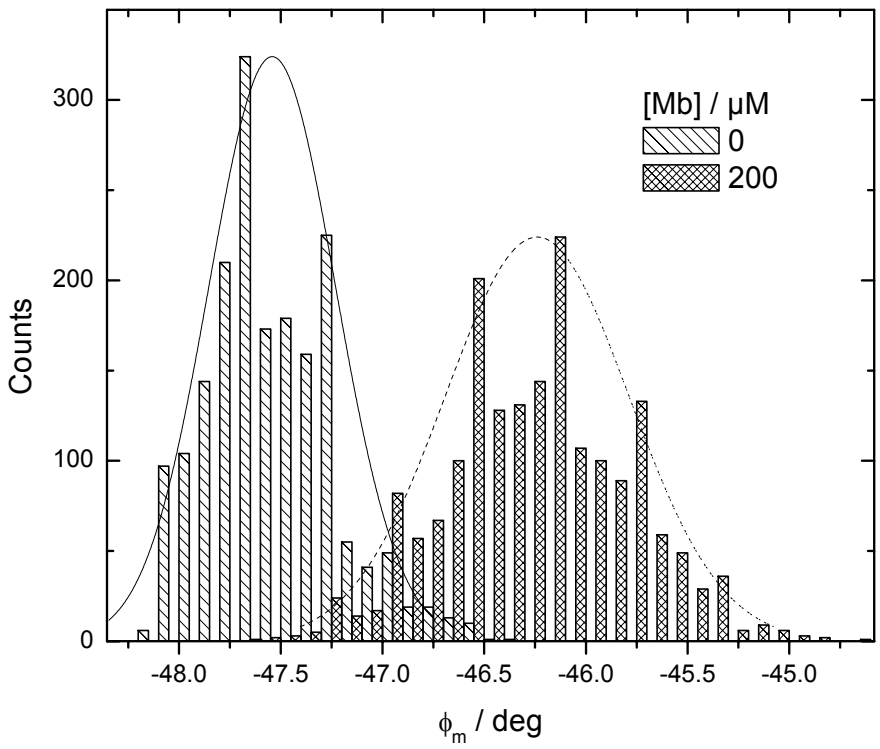

Figure 7.6: Distribution of phase angles for 200 μM and 0 μM aqueous myoglobin solution.

Phase angles are binned into 0.1° ranges to generate the histograms. The normal distributions (solid and dashed lines) are also shown.

The solid and dashed lines are normal distributions for 0 and 200 μM Mb respectively. A normal distribution (i.e. Gaussian distribution) is given by

$$f(\phi_m) = \frac{1}{\sqrt{2\pi\sigma^2}} e^{-\frac{(\phi_m - \mu)^2}{2\sigma^2}} \tag{7.1}$$

where σ is the standard deviation and μ is the mean of the phase angle. μ_{Mb} is beyond $\mu_{H_2O} + 3\sigma_{H_2O}$ indicating the samples differ and Mb has indeed been detected. Using $\mu_{H_2O} + 3\sigma_{H_2O}$ and assuming a linear dependence of ϕ_m on concentration at low C gives a detection limit of ~ 140 μM Mb. This corresponds to εC_{DL} = 16 cm^{-1}, roughly a factor of 60 times greater that the best εC_{DL} reported for the 800 nm experiment (Chapter 6).

This preliminary result could be improved by performing the measurements at the optimal frequency of the system, ω_{opt}. Also, monitoring the modulation depth m may provide a better detection limit, albeit one that is not independent of the laser intensity. (Recall from Chapter 2 m must be normalized by $m(\omega \to 0)$. If the laser intensity changes then the normalization factor must again be determined.) Other aspects of the experiment that could be improved include: using a sample flow cell rather than a suspended drop to improve system stability; using a different means of input coupling that also does not involve a suspended drop again to improve system stability, and; using polymer clad fibre so that the cladding can be removed, allowing direct access to the fibre core and providing a more suitable intensity distribution.

7.4 Conclusion

The preliminary result presented above shows promise for label-free detection of biomolecules using 405 nm laser radiation in conjunction with the multi-pass technique of fibre loop sensing. A minimum detectable absorption loss (MDAL) of 16 cm^{-1} for aqueous myoglobin solution was found. Numerous means of improving this result have been listed above, suggesting that the MDAL could likely be reduced by an order of magnitude without great effort. The advancing development of UV laser diodes and low-loss UV fibre could yield a highly sensitive, low-cost sensor in the near future.

7.5 References

1. Cavaluzzi, M. J.; Borer, P. N., Revised UV extinction coefficients for nucleoside-5'-monophosphates and unpaired DNA and RNA. *Nucleic Acids Research* **2004,** 32, (1), 13.

2. Buback, M.; Vögele, H. P., *FT-NIR Atlas*. VCH Publishers: Weinheim, 1993.

3. Li, Q. C.; Mabrouk, P. A., Spectroscopic and electrochemical studies of horse myoglobin in dimethyl sulfoxide. *Journal of Biological Inorganic Chemistry* **2003,** 8, (1-2), 83-94.

Chapter 8 Decreasing acquisition time

This chapter presents two experiments focused on making frequency domain ringdown spectroscopy (FD-RDS) measurements as fast as possible. The first experiment seeks to determine the best time resolution that can be achieved in measuring the phase angle ϕ_m, and hence τ, given our present equipment. Working in the frequency domain (FD) already has an advantage over the time domain (TD) in this regard. The second experiment looks at two methods to quickly characterize a loop/cavity. Characterization yields the exponential order of the system, the decay times, the optimal working frequency (see Chapter 2), and the phase angle offset ϕ_o. This should be done before a cavity/loop is put into use as a sensor or spectroscopic instrument. Here FD-RDS is at a definite disadvantage to TD-RDS.

Frequency domain methods for determining cavity/loop loss have been previously shown to have better time resolution compared to time domain (TD) methods.[1] In the FD the phase angle was read from the lock-in at 10 Hz and would provide sufficient resolution for lab-on-a-chip applications. In the TD decay traces are averaged on an oscilloscope, transferred to a PC and fit to obtain the ringdown time. This process is time consuming and cannot be performed at as high a repetition rate. The first experiment presented in this chapter seeks to find the limit of the time resolution of phase measurements in the FD. To achieve this, a novel optical microphone (OM) was built that is based on an FBG cavity (see Chapter 4).

Full characterization in the frequency domain of a cavity/loop which exhibits a multiexponential decay can be quite time consuming. The phase angle must be measured at many modulation frequencies for many analyte concentrations and the resulting curves fit to obtain the ringdown times, steady-state intensities, and ϕ_o for each frequency. The time domain in contrast provides all the desired values with very little effort. Just as described above, the averaged waveform is fit and the necessary values (besides ϕ_o) found. The fluorescence spectroscopy literature provides some examples of how to improve characterization time in the frequency domain using Fourier transform methods. The procedure for this and its application to a model system is presented below.

8.1 Optical microphone

An acoustic transducer that is based on the spectral response of an FBG cavity was developed to determine the maximum time resolution of phase shift measurements. The principle of operation is as follows. A cavity was made out of two nearly identical FBGs with overlapping reflection bands. Acoustic waves that interact with the fibre that contains one of the FBGs cause the FBG to stretch, strain or bend, and thereby result in a wavelength-shifted reflection band. If the second FBG has been isolated from that acoustic wave and has an unchanged reflection spectrum, the cavity loss in this narrow wavelength window will change and the phase angle will change. The spectral response is expected to be very fast and will oscillate with the same frequency as the driving

acoustic modulation. As one FBG is bent in response to the acoustic force the pitch, Λ, of the grating is altered. Recall that the Bragg resonance occurs at[2]

$$\lambda_B = 2n_{eff}\Lambda \tag{8.1}$$

If the pitch of the grating is modulated sinusoidally, so too will the Bragg wavelength. The experimental case is not quite so simple. The degeneracy of the two polarization modes denoted by LP_{01} is broken by passing it through the bent grating since it lacks cylindrical symmetry. A detailed treatment of these effects, though possible is beyond the scope of this thesis. Here it suffices to say that the Bragg wavelength is red-shifted as the grating is bent.

A working wavelength for the device is chosen such that it lies on either the blue or red edge of the cavity attenuation band. As one FBG's resonance wavelength shifts periodically (***Figure 8.1***) and the other's remains fixed, their attenuation bands overlap to a greater or lesser extent. Less overlap leads to higher transmission and a shorter ringdown time, hence a smaller phase shift. Choosing a working wavelength on the blue edge of the cavity attenuation band results in in-phase reproduction of the acoustic wave by the cavity transmission or the phase angle. Conversely, a working wavelength on the red edge of the cavity results in waveform reproduction that is 180° out of phase with the driving acoustic signal.

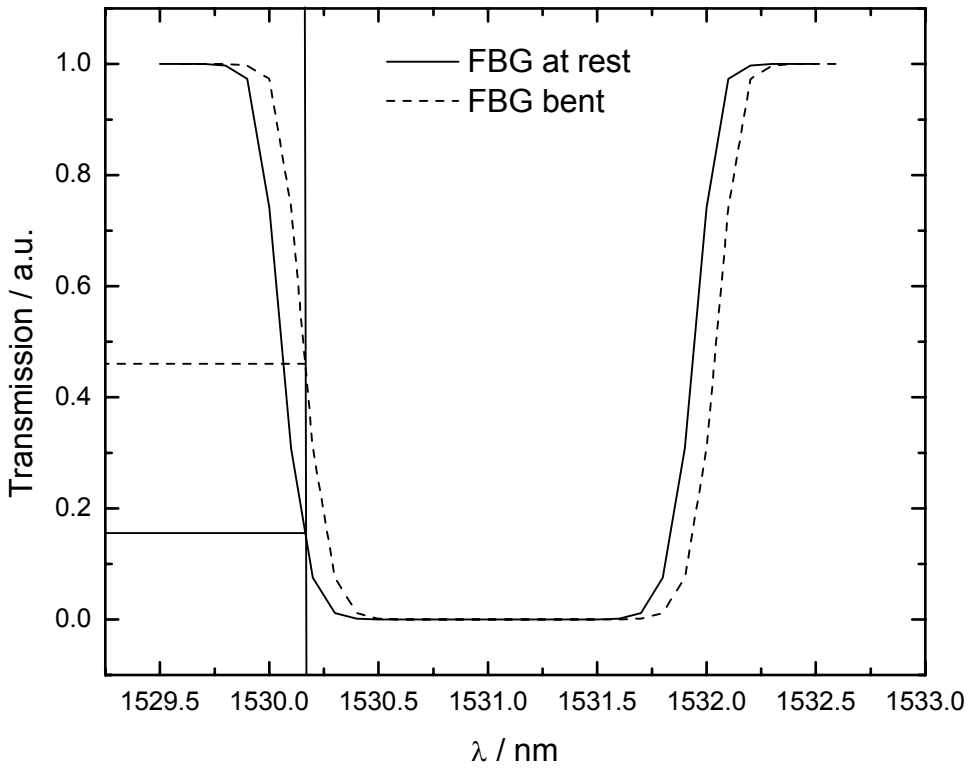

Figure 8.1: Simulated transmission spectra for an FBG at rest and bent.

The solid vertical line denotes the laser wavelength. The solid horizontal line marks the transmission for the FBG at rest, and the dashed horizontal line marks the transmission for the FBG when it is bent.

8.1.1 Apparatus and experiment

For these experiments an FBG cavity ~30 cm in length was constructed consisting of two FBGs with attenuation bands centred at 1531 nm. A 99:1 tap was used as an optical isolator to limit back-reflection to the laser. One FBG was mounted on an audio speaker with the fiber was taped onto the speaker shell and the center of the speaker cone (7 cm diameter) above and below the FBG position. The speaker may be driven with a sine wave generated on a PC. At the rest position of the speaker, there is some bending of the FBG region. As the speaker cone moves up the fiber straightens, and as it moves

down the fiber bends more relative to the rest position. No effort was made to prevent out-of-plane motion. The other FBG was held fixed on a piece of card to prevent bending.

The laser (Ando AQ4320D) was tuned to 1530.200nm with a power of 3.98mW (narrow line width) and intensity modulated at 270 kHz to give a phase shift (ϕ_m) of –45° when the system was at rest. The phase shift was measured using a lock-in amplifier (SR844). Lock-in settings varied but for low audio frequencies, a 24 dB / octave filter seemed to effectively filter out the contributions of higher harmonics whereas for high frequencies 6 dB / octave was sufficient. The phase shift signal and audio reference signal were recorded on an oscilloscope with 16 acquisitions being averaged (Tektronix TDS 3032). See ***Figure 8.2***.

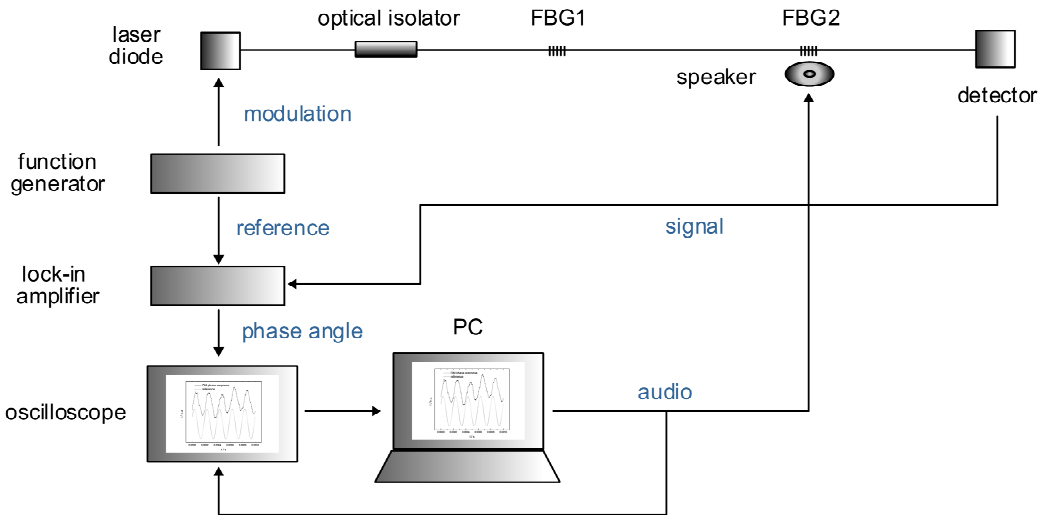

Figure 8.2: Experimental apparatus of the optical microphone.

The optical microphone response was tested from 40 to 5000 Hz. As the audio frequency was increased over that range, the lock-in time constant was decreased so proper sampling was ensured. The tested frequency range was limited by the speaker (with a low frequency cut-off at ~35 Hz) and by the lock-in (with the shortest time constant being 100μs or 10 kHz). With the time constant being regarded as an effective sample rate, 5 kHz represents the Nyquist limit for adequate reproduction of an input waveform via the phase angle. The phase output of the lock-in is refreshed at 12 – 24 kHz, so does not impose a limit on the sample rate.

Sine waves were generated on a PC in steps of 10 Hz between 40 and 100Hz, 100 Hz between 100 and 1000 Hz, and 1 kHz between 1 and 5 kHz. The audio volume was not kept constant since the speaker response is not linear with frequency. The volume was adjusted until a clean phase response was observed.

8.1.2 Results and discussion

The phase spectrum of the cavity in place and stationary shows a band from 1530.1 to 1531.8 nm, as shown in the figure below (***Figure 8.3***). The filled circle denotes the working wavelength for these experiments (1530.200nm).

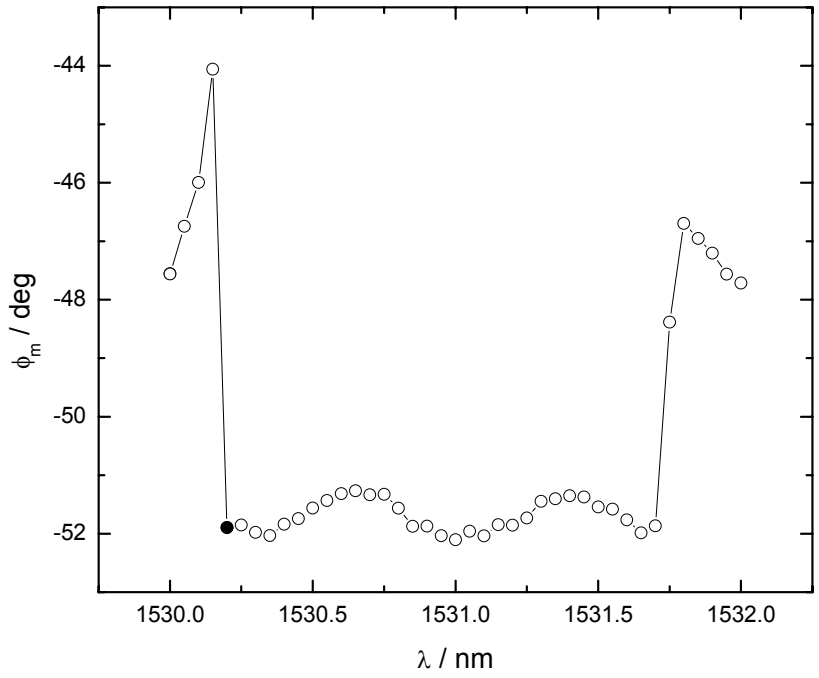

Figure 8.3: Transmission spectrum of the optical microphone FBG cavity.

The OM showed a response across the entire frequency range tested – from 40 to 5000 Hz. ***Figure 8.4*** shows the modulation in phase angle resulting from changing cavity loss as one FBG is bent using a 5000 Hz sine wave.

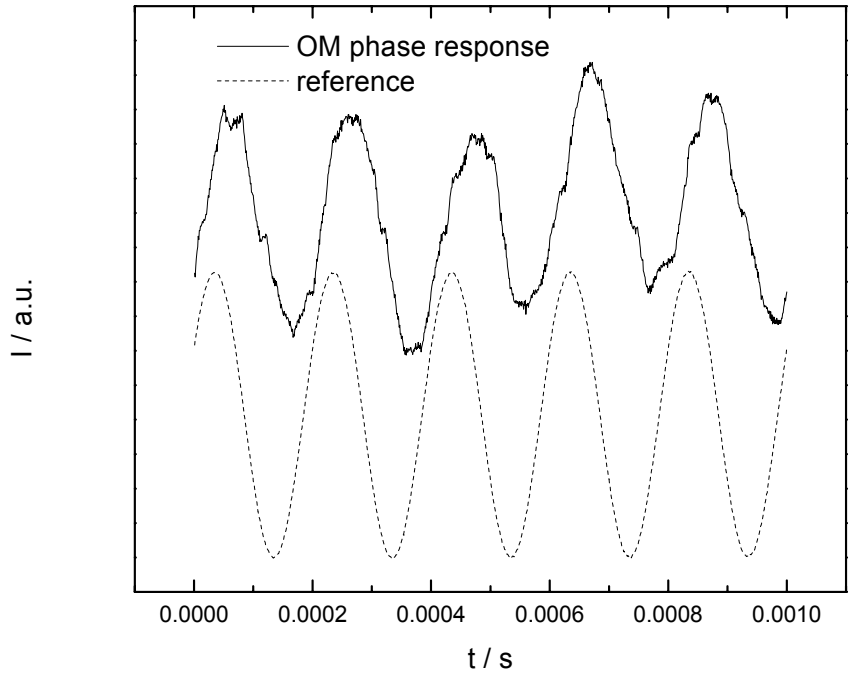

Figure 8.4: Phase angle response of the OM due to a 5000 Hz sine wave applied to the transducer.

Fourier transform of the audio reference signal shows the fundamental at 5004.88 Hz. FT of the phase angle OM response shows a strong peak also at 5004.88 Hz, indicating that accurate frequency reproduction is possible (***Figure 8.5***). The peaks above the fundamental do not match harmonic frequencies and are of unknown origin. The phase angle is updated at a rate somewhere between 12 and 24 kHz. This could be the origin of the peak at 21.4 kHz.

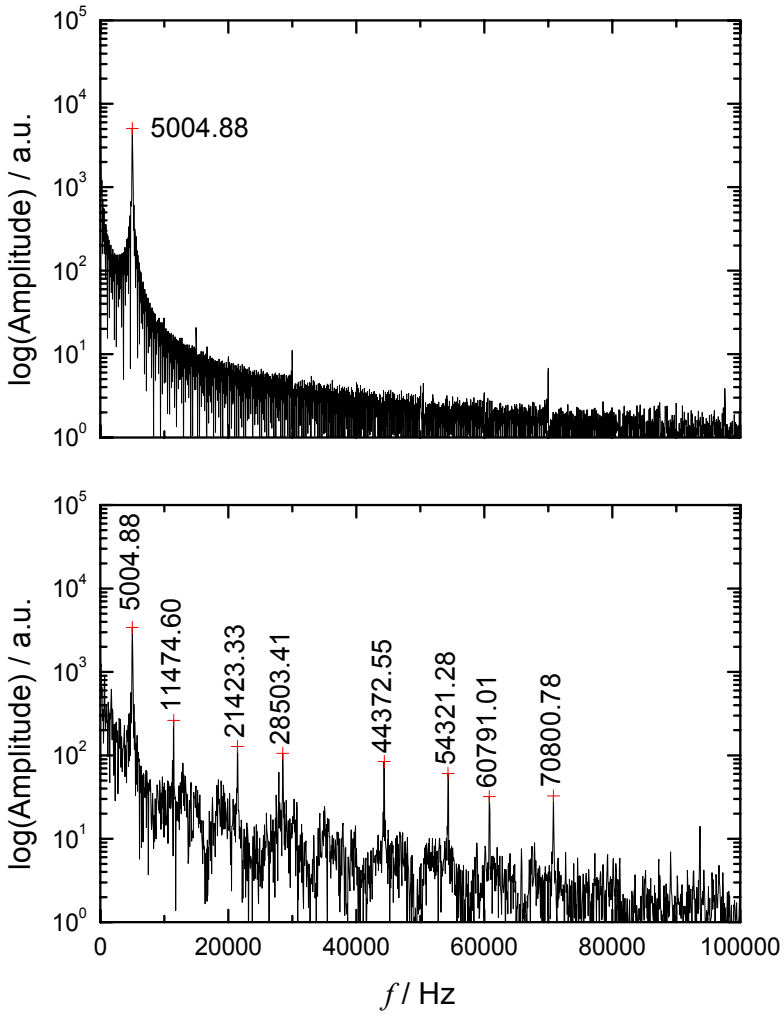

Figure 8.5: Fourier transform of the reference (top) and OM response (bottom) showing their frequency content.

Qualitatively the OM response is better at low frequency as it took less volume here to produce a clean sinusoidal response. The laser was tuned outside of the attenuation range of the FBGs to verify that the signal in fact is from the OM and not from interference being picked up in the cables. Below 1529.5 and above 1532.5 nm there was no modulation in the phase angle observed.

At the time the experiment was conducted it had not been realized that tuning the laser away from the cavity attenuation band and measuring the phase shift was the best

way to obtain ϕ_o. Instead a 1 m length of standard SMF-28 was used. The resulting "true" phase angle was ~-5°. Thus a larger response may have been achievable using a higher modulation frequency where the absolute value of $\frac{d\phi}{d\omega}$ is larger. Procedural inadequacies aside, the experiment did show that the time resolution of a phase measurement is at least 500 μs, more than enough to meet the time resolution requirements for a ringdown apparatus serving as a detector for electrophoretic separations. In our lab it was later shown that, in the time domain, a single FBG can serve as a suitable microphone for all audible frequencies (i.e. 20 Hz to 20 kHz) and for photoacoustic spectroscopy, with a maximum response of ~ 40 MHz.[3]

8.2 Fast characterization methods

While measuring the phase angle "on the fly" as in the above experiment allows for a better time resolution compared to fitting an exponential decay trace to determine the ringdown time, initial characterization of the loop at multiple frequencies can be a slow process. In the frequency domain, multiexponential decays lead to the necessary process of measuring the phase shift and modulation depth at many modulation frequencies and for many concentrations of analyte in order to calibrate the instrument. To speed up this process, one could envision a system of multiple phase comparators, each detecting the phase of a harmonic of the fundamental of a square wave. However this would be expensive and a frequency scan would still be required. Here we outline a

method is derived from a Fourier analysis of the cavity output that could permit more efficient characterization of the frequency response of an optical cavity.

8.2.1 Fourier transform method

As alluded to in Chapter 2, the impulse response function of the system can be recovered by deconvolution of the cavity input and output signals. Convolution in the time domain is equivalent to multiplication in the frequency domain, and similarly division in the FD is equivalent to deconvolution in the TD. The cavity input, $S_{input}(t)$, and output, $S_{output}(t)$, recorded in the time domain are converted to the frequency domain using the Fourier transform. The ratio of the FD modulation depths is taken and the result is inverse Fourier transformed back into the TD to yield the deconvoluted impulse response function.[4] Most interesting for our application is to forgo the IFT step and calculate the phase angle and modulation depth from the real and imaginary parts of the Fourier transformed waveforms. Mathematically this procedure is

$$\begin{aligned} S_i(\omega) &= \int_0^\infty S_i(t) e^{-i\omega t} dt \\ \phi_i(\omega) &= \arctan\left(\frac{\mathrm{Im}(S_i(\omega))}{\mathrm{Re}(S_i(\omega))}\right) \\ m_i(\omega) &= \sqrt{\mathrm{Im}(S_i(\omega))^2 + \mathrm{Re}(S_i(\omega))^2} \end{aligned} \tag{8.2}$$

The phase angle is given by

$$\phi(\omega) = \phi_{input}(\omega) - \phi_{output}(\omega) \tag{8.3}$$

and the modulation by

$$m(\omega) = \frac{m_{input}(\omega)}{m_{output}(\omega)} \tag{8.4}$$

The utility of this method depends on the frequency content of the input waveform used. For example, Fernicola et al. used a square wave to excite a fluorophore. The phase and modulation can then be determined for all the frequencies contained in the original square wave, i.e. the fundamental and all odd harmonics.[5] Gratton et al. used a high harmonic content pulse that provides better results.[6] Iwata et al. have demonstrated a method that is superior to the earlier approaches. These workers have used a chirped sine wave in which all frequencies are equally represented from DC to the upper frequency limit used.[4] This allows the phase and modulation to be determined at all frequencies (in practice limited by the frequency resolution of the FT) up to the Nyquist limit, i.e. half the highest frequency in the chirp. For any of these methods to be useful, the sample frequency and the number of samples must both be as high as possible. Iwata et al. outline lower limits for these values. Also necessary is a high signal-to-noise ratio with little signal distortion. The former was accomplished by Iwata by averaging 10000 acquisitions on an oscilloscope. Unfortunately our laboratory does not possess the means to perform such extensive averaging. The use of FT for analysis of ringdown transients in CRDS is not without precedent.[7] Mazurenka et al. make use of a modified form of the second expression in (8.2). However, their scheme can only be used to determine τ for single exponential decays.

8.2.2 Test of the FT method with a model system

A chirped sine wave from a function generator (Tenma 72-5010) was used to drive an electrical circuit simulating a ringdown system. A resistor-capacitor (RC) circuit (***Figure 8.6***) has an identical impulse response function to a single exponential cavity or loop, with the product of the resistance (220 kΩ) and the capacitance (117 pF) defining the "ringdown" time (RC = 25.7 μs). The reference and circuit output waveforms were averaged on an oscilloscope. The data analysis was carried out using Matlab.

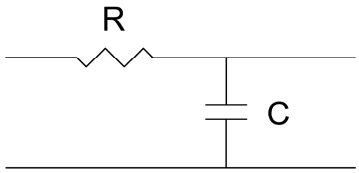

Figure 8.6: RC-circuit used with a chirped sine wave to test recovery of the impulse response function.

Time domain determination of the RC circuit decay time gives a result of 26.96 ± 0.01 μs. This differs from the predicted value based on the manufacturer's values of R and C, though this is not unexpected since these values commonly differ by a small amount from the specified ones. The chirped sine input and output of the RC circuit are shown in ***Figure 8.7***.

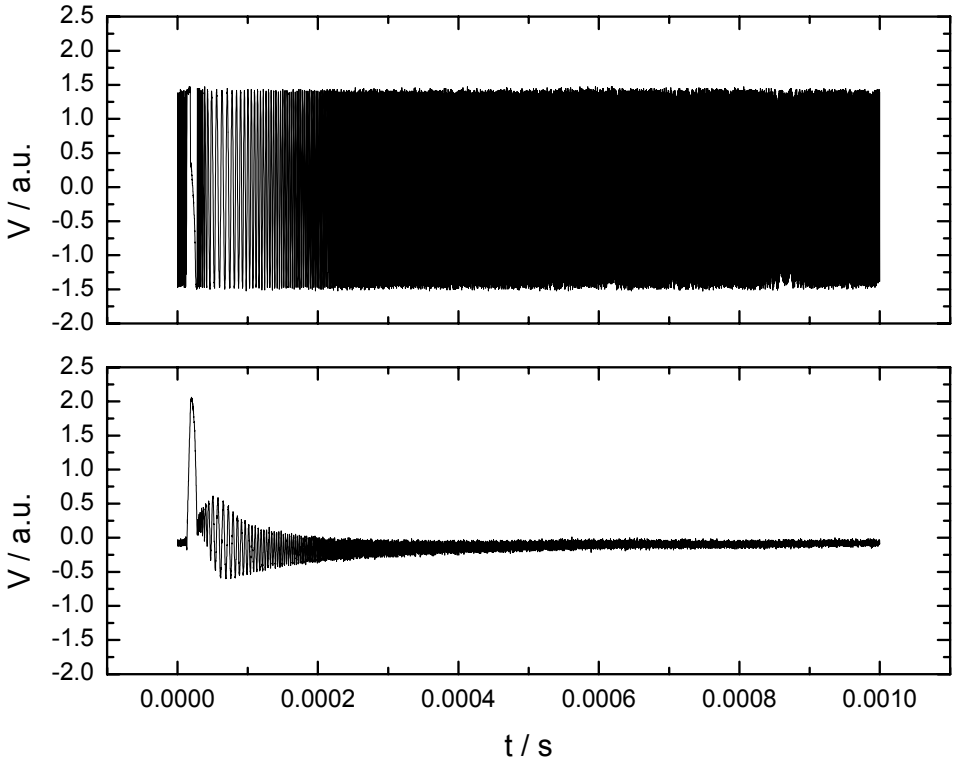

Figure 8.7: Chirped sine wave input (upper) and output (lower) for the RC circuit.

IFT of $m(\omega)$ from equation (8.4) produces the plot shown in the upper panel of ***Figure 8.8***. The data are then smoothed by a 16-point moving average to reduce noise (lower panel). A single exponential fit to the smoothed data gives a decay time of 27.34 ± 0.07 μs. Good agreement, though not within error, between the TD and FD decay times is noted.

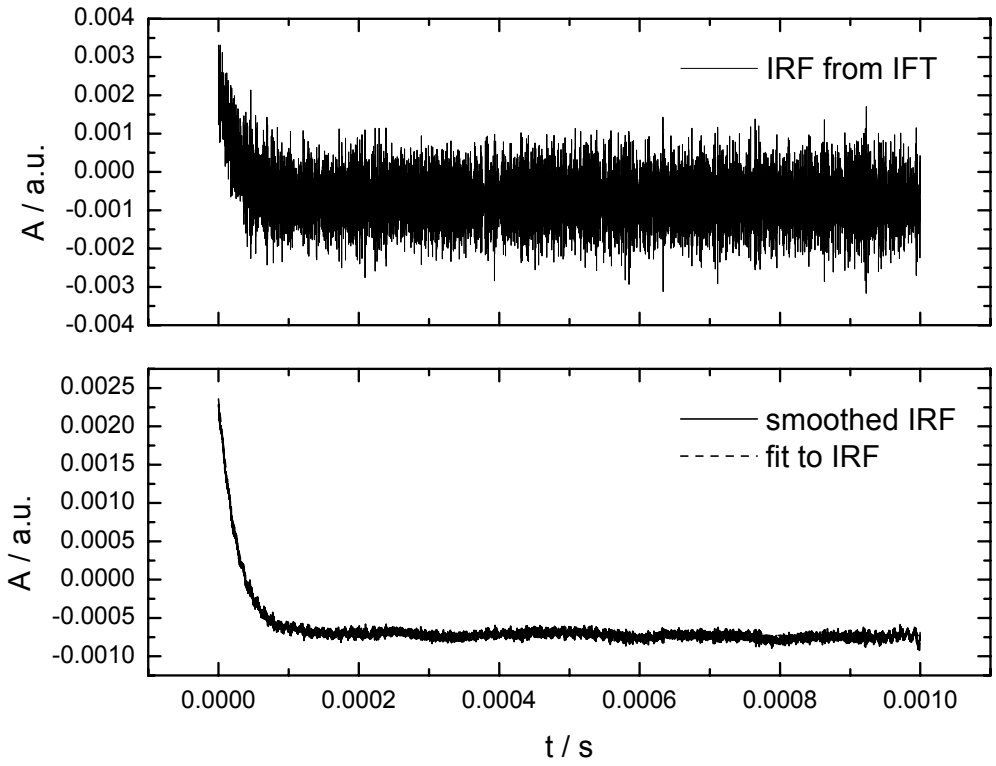

Figure 8.8: Impulse response function of the RC circuit determined from the frequency domain.

The bottom panel shows the IRF smoothed by a 16-point moving average and fit to a single exponential decay.

The phase angle obtained from equation (8.3) is shown in ***Figure 8.9***. It shows behaviour completely unlike what is expected. The very strong dependence on the modulation frequency is attributed to the fact that ϕ_o was not accounted for.

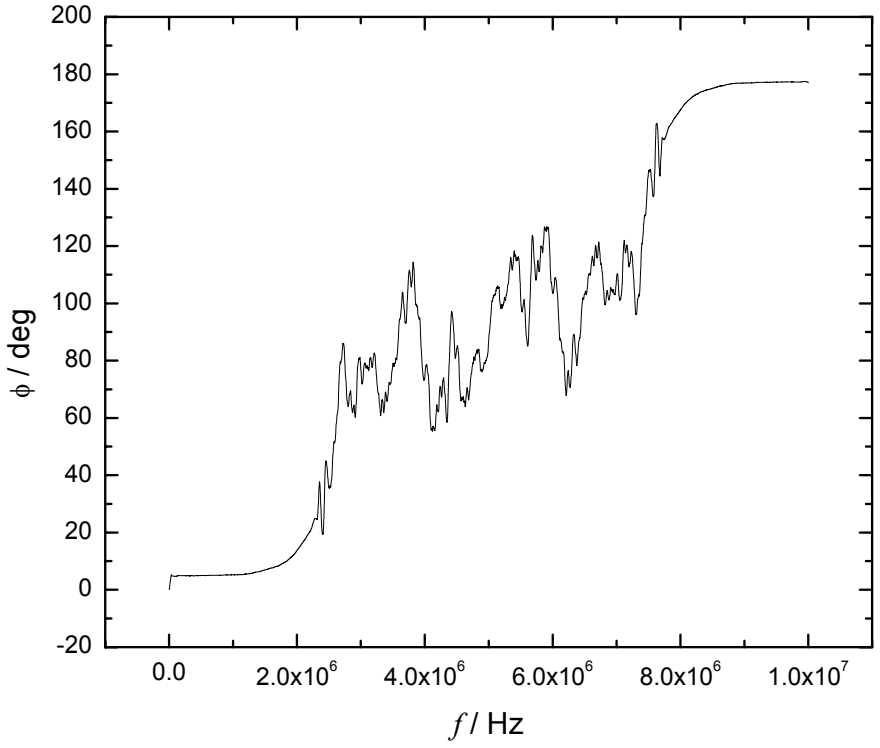

Figure 8.9: Phase angle for the RC circuit determined from the Fourier transform.

In Chapter 4 it was shown that the phase offset could be obtained for a linear cavity by tuning the laser outside of the resonant wavelengths of the FBGs, in effect bypassing the cavity. Bypassing the RC circuit but keeping as much of the signal path identical as possible should provide a chirped signal that when Fourier transformed gives the phase offset at all frequencies below the Nyquist limit. Thus in the context of an FBG cavity or an RC circuit, recording the input, output, and bypass signals upon excitation with a chirped sine wave should yield ϕ_m, ϕ_o, and ϕ in very little time.

Overall the chirped sine method shows promise for application to cavity/loop characterization. The preliminary results presented were limited by the frequency maximum and chirp rate of the function generator and the time resolution and averaging

capabilities of the oscilloscope. With suitable equipment this method could easily be applied to a fibre loop or cavity.

8.3 Conclusion

We have demonstrated that a time resolution of 500 μs in measuring the phase angle is achievable, made possible by the construction of a novel acoustic transducer based on an optical cavity consisting of two nearly identical FBGs. This time resolution should easily accommodate the needs of microfluidic separations for a number of years.

In the pursuit of fast cavity characterization, we investigated the highly parallel acquisition method of Iwata et al. which makes use of a chirped sine wave. For an RC circuit, time domain measurements and application of Iwata et al.'s method yielded very similar results. Due to limitations of our present equipment, we could not extend this method to resonators exhibiting short ringdown times. However it shows good promise.

Future work could be directed towards verifying whether a chirped signal bypassing a cavity or circuit is a fast method of determining the phase offset of the system. Finding this offset remains the slowest step in characterizing a cavity/loop before it can be put to practical use.

8.4 References

1. Tong, Z. G.; Wright, A.; McCormick, T.; Li, R. K.; Oleschuk, R. D.; Loock, H. P., Phase-shift fiber-loop ring-down spectroscopy. *Analytical Chemistry* **2004,** 76, (22), 6594-6599.

2. Schroeder, K.; Ecke, W.; Mueller, R.; Willsch, R.; Andreev, A., A fibre Bragg grating refractometer. *Measurement Science & Technology* **2001,** 12, (7), 757-764.

3. Yang, Q.; Barnes, J.; Loock, H. P.; Pedersen, D., Time-resolved photoacoustic spectroscopy using fiber Bragg grating acoustic transducers. *Applied Optics* **2007**, in print.

4. Iwata, T.; Shibata, H.; Araki, T., Construction of a Fourier-transform phase-modulation fluorometer. *Meas. Sci. Technol.* **2005,** 16, 2351-2356.

5. Rosso, L.; Fernicola, V. C., Time- and frequency-domain analyses of fluorescence lifetime for temperature sensing. *Review of Scientific Instruments* **2006,** 77, (3, Pt. 1), 034901/1-034901/6.

6. Feddersen, B. A.; Piston, D. W.; Gratton, E., Digital Parallel Acquisition in Frequency-Domain Fluorimetry. *Review of Scientific Instruments* **1989,** 60, (9), 2929-2936.

7. Mazurenka, M.; Wada, R.; Shillings, A. J. L.; Butler, T. J. A.; Beames, J. M.; Orr-Ewing, A. J., Fast Fourier transform analysis in cavity ringdown spectroscopy: application to an optical detector for atmospheric NO_2. *Applied Physics B-Lasers and Optics* **2005,** 81, 135-141.

Chapter 9 Future Work

This chapter includes an overview of possible future directions for the experiments described in this thesis and the proposal of novel experiments based on the ringdown technique.

9.1 Minimizing optical loss

An obvious direction for the experiments presented above is to refine the design to achieve a lower detection limit. This may be accomplished by a number of routes but likely only by using them in combination one can hope to gain a large improvement in performance. The major issue to be faced revolves around reducing the optical loss in the system to a minimum. The two major contributors to loss are the coupling method used to introduce and extract light, and the design of the sample interface. As mentioned in Chapter 3 an evanescent coupler based on field access blocks exhibits lower excess loss than conventional couplers. A multicoupler design is also a possibility, where multiple input fibres surround the cavity/loop fibre - each introducing a small intensity of light. Such couplers have been used to side-pump fibre lasers.[1] Inline detectors are available for SMF and MMF which feature very low insertion loss and utilize a small PIN photodiode in contact with the fibre cladding. Optimizing transmission through the sample interface could be facilitated by precise control over lens shape (e.g. by VUV laser machining) and submicron alignment.

9.2 Applications

Biomolecule detection in electrophoretic separations is one of the envisioned applications that spurred the development of CRDS in optical waveguides. Detection of HSA and DNA via non-covalent labeling with an NIR absorber (at 795 nm) has recently been demonstrated.[2] The true potential of FCRDS however lies in unlabeled detection of such species via absorption. Promising target absorption features are the first N-H and C-H vibrational overtones. These both occur at wavelengths in the telecom range where optical fibre exhibits its lowest loss. Both also offer a very general means of detection since all biomolecules contain N-H and/or C-H bonds.

Single cell detection is another avenue that deserves investigation. This would most easily be achieved using single mode fibre with a core diameter of 10 μm or less. Cells generally have diameters in the range of ~1 to 10 μm. A cell passing through the sample interface would occlude a fair portion of the fibre core and would be detectable via scattering and absorption.

9.3 Other wavelength ranges and resonator types

Three wavelength ranges were investigated during the course of this work, but others may merit exploration as well. The wavelengths chosen were selected for low material loss of the fibre medium (1550 nm), inexpensive high power *cw* sources (795 nm), and high absorption cross section of a wider range of molecules (405 nm). Unfortunately, all these desirable features seem to be mutually exclusive and no one

wavelength exists that satisfies all three. However with the help of an optical parametric oscillator (OPO) laser system, high power pulses are available over a wide range of wavelengths through second harmonic and difference frequency generation. With wavelength restrictions lifted it may be feasible to investigate the IR range of the spectrum where fundamental vibrational transitions indicative of specific functional groups may be excited. Fibre materials manufacturing at 3 to 4 μm is still in its early stages and manufacturers cannot yet provide a low-loss and mechanically robust material. It can be expected that with the recent developments in producing "low" loss chalcogenide fibres and ZBLAN fibres, FLRDS experiments at about 3 μm may be possible within a few years. Presently, the loss in these materials is about 200 dB / km compared to < 1 dB / km for telecom fibres at 1.55 μm.

Reducing the size of the optical cavity is the best means to circumvent high material loss and a perfect candidate for this is a micro-resonator – such as a micro-sphere resonator or a micro-toroidal resonator. Research on such resonators has been taking place for a number of years in association with the telecom industry where they find use as add/drop filters.[3] A micro-sphere can be fabricated from fibre material using a relatively simple process. A flat-cleaved fibre end exposed to repeated electrical arcs will result in the melted glass being pulled into a sphere due to surface tension. Laser light of the correct wavelength can excite a whispering gallery mode (WGM) which travels around the equator of the sphere just below the surface. The evanescent wave of the WGM extends out into the external medium, allowing a surrounding liquid to be probed.

The micro-sphere can be used to measure either refractive index or optical absorption of some sample. Limitations of the micro-sphere approach include its cross-sensitivity to temperature and the requirement of accurate and stable positioning of the sphere over the coupler (such as an FAB or tapered fibre). Accounting for these limitations, IR spectroscopy with this scheme appears promising. A recent review reports that ringdown times of 43 ns are possible with a 40 μm microsphere.[4] Work at NIR wavelengths with μ-spheres has already begun in our laboratory.[5] Visible and UV wavelengths, where fibre material loss is also quite high, would likewise benefit from miniaturization of the optical resonator.

Micro-toroidal resonators and variations thereof also show promise for integration with microfluidic systems. Micro-toroidal resonators can be fabricated in a planar substrate. Machining a hole through the centre of the ring to accommodate the flow of a separated mixture may prove a useful configuration. Alternatively, a WGM excited in a capillary wall via a tapered fibre may be able to probe the liquid inside. An improvement on this would be to perform the electrophoretic separation inside a hollow core waveguide instead of a capillary and excite a WGM perpendicular to the fibre axis. The hollow core waveguide should exhibit much lower loss compared to a standard capillary.

9.4 Photonic crystal fibres

Photonic crystal fibres offer a number of advantages over conventional fibre. They (a) can be designed to be endlessly single mode (i.e. single mode at all wavelengths) for

scanning over very broad wavelength ranges; (b) can have a larger mode area (up to 10 times that of standard SMF, i.e. mode field diameter of 60μm) in order to probe a large sample volume comparable to that of multimode fibre whilst maintaining the advantages of single mode operation;[6] (c) can be lensed in such a way to collapse the air holes near the facet end and thus protect the fibre interior from contamination while affording a long beam expanding region to make possible longer working distances between two lensed ends;[7] and, (d) being constructed of one glass with one refractive index, the lenses will not be subject to aberrations due to mixing of core and cladding glasses. One can thus envision a PCF fibre loop or cavity analogous to the ones presented above with a number of new desirable features.

Opportunities also exist to use the interior of the PCF as a sample cell. The empty volume in the PCF can be filled easily with a gas sample to provide an analog to mirror based CRDS for atmospheric sensing or breath analysis. PCF has already been used in a single-pass arrangement for gas sensing/spectroscopy.[8] The apparatus could be designed either as a linear cavity or a loop. Constructing a linear cavity has been made feasible by recent research conducted on writing FBGs into PCF.[9] Introduction of liquid into PCF is also possible but may be hampered by the high refractive index needed to ensure guiding (n = 1.8).[10] Due to the physically long path length inherent in the use of the interior of PCF, this will not be a technique with high time resolution for integration with separation methods but lends itself more to trace detection.

9.5 Increasing sensitivity

A fibre cavity/loop exhibiting a single exponential decay can be described, borrowing concepts from electronics, as a single-pole low-pass filter[11] with a 3 dB cutoff frequency of $1/\tau$ and a roll-off of 2.6 dB / octave. Passing light through multiple micro-ring resonators has been shown to substantially increase the roll-off at optical frequencies.[3] A larger, bulk-fibre-based version of these resonators would act as a sharp roll-off low pass filter at typical modulation frequencies. The output after N loops is given by the convolution of the impulse response functions for the loops,

$$I(t) = I_1(t) \otimes I_2(t) \otimes I_3(t) ... \otimes I_N(t) \tag{9.1}$$

One finds that the overall modulation is the product of the modulations of the individual loops,

$$m = \prod_{i=1}^{N} m_i = \prod_{i=1}^{N} \frac{\alpha_i}{\sqrt{1+\omega^2\tau_i^2}} \tag{9.2}$$

This relationship gives the result that the same $\Delta\tau$ will lead to a greater Δm for larger N, hence the sensitivity is better for larger N. No expression of comparable simplicity to (9.2) can be written for the overall phase. For $N = 1$ to 4

$$\begin{aligned}
\tan\phi(N=1) &= -\omega\tau \\
\tan\phi(N=2) &= \frac{2\omega\tau}{\omega^2\tau^2-1} \\
\tan\phi(N=3) &= \frac{\omega\tau(\omega^2\tau^2-3)}{3\omega^2\tau^2-1} \\
\tan\phi(N=4) &= \frac{4\omega\tau(\omega^2\tau^2-1)}{\omega^4\tau^4-6\omega^2\tau^2+1}
\end{aligned} \tag{9.3}$$

For N = 1 the phase angle goes to -90^o as $\omega \to \infty$. For N = 2, now $\phi \to -180°$ as $\omega \to \infty$. The limiting phase angle continues to increase with N by multiples of 90^o and the sensitivity again will be greater for larger N. However, this is only the case if τ changes for all loops. In practice, this could be accomplished for two loops of equal length both interfaced with the same sample at, or very near to, the same point.

9.6 Birefringence measurements

One potential area of future investigation, which is of particular interest to the field of chiral synthesis, is the measuring of the circular birefringence (non-resonant polarization rotation) of picolitre liquid samples with ringdown methods. A chiral molecule exhibits circular birefringence (CB) or optical rotary dispersion (ORD).[12] Incident linearly polarized light will be altered to give rise to elliptically polarized light upon passing through a chiral sample.[13] One enantiomer will rotate the polarization in the opposite sense of the other enantiomer, allowing one to distinguish between enantiomers. For a mixture of enantiomers, the polarization will be rotated to a smaller degree in the direction of whichever enantiomer is in the highest concentration, allowing the enantiomeric excess to be determined.

Von Lerber et al. have developed a method to measure the intrinsic linear birefringence of SMF and the circular birefringence induced by twisting the fibre.[13] The two modes which form the LP_{01} are orthogonally linearly polarized. When injected into

an optical cavity, birefringence causes one mode to experience a slightly different refractive index than the other and thus will experience a different roundtrip pathlength. This gives rise to a time dependent phase shift between the two modes (i.e. a phase shift between the two electromagnetic fields). Interaction of the two cavity modes generates a homodyne beat signal. The beat frequency can be related to the refractive index difference between the two polarizations. A fit to the build-up and ring-down transient recorded after the cavity output has been passed through a polarization controller and a polarizing beam splitter can yield the direction of polarization as an angle relative to the effective axis of linear birefringence. Twisting the fibre (i.e. inducing CB) results in a change in this angle. Thus adaptation to CB measurements on chiral liquids would simply require the inclusion of a sample cell in the cavity.

9.7 Increasing intracavity intensity

Increasing the intracavity intensity is important for improving the performance of a ringdown spectrometer. A higher intracavity intensity generally results in a better signal-to-noise (S/N) ratio, which leads to a lower detection limit and better sensitivity. This can be achieved by coupling a laser's output to a single longitudinal cavity mode. Such resonant techniques are in fact at the forefront of detection limit in gas phase mirror-based CRD spectrometers.[11] However, inevitable fluctuations in laser wavelength and cavity length that can move the system away from resonance mean that this approach is not well suited for FD-CRDS (a large decrease in the modulation depth is accompanied by random

oscillations in the phase angle). Another means of achieving high intracavity intensity was exploited in the first demonstration of FLRDS by Stewart et al.[14] Due to the high insertion loss of their micro-optic gas cell, they incorporated an erbium-doped fibre amplifier (EDFA) in the loop. This resulted in very long ringdown times, but with the consequence that they were dependent on the gain stability of the amplifier. Later work by Stewart et al. showed that some gain-stabilization of the EDFA is possible,[15, 16] and in the future suitable performance may be achieved. This approach is amenable to FD-CRDS and could be applied in loops or linear cavities.

In such an apparatus the EDFA forms but a small part of the total resonator length. It is also possible to envision micro-resonators where the entire resonator is composed of the gain medium. Due to the intrinsically small volume probed by the evanescent field of a micro-resonator it should be beneficial to introduce a gain source, not to compensate for loss but to increase the cavity enhancement. The pump and seed could be delivered via the same fibre. Pumping above the lasing threshold would simply be a variation of intracavity laser absorption spectroscopy.

9.8 References

1. Polynkin, P.; Temyanko, V.; Mansuripur, M.; Peyghambarian, N., Efficient and scalable side pumping scheme for short high-power optical fiber lasers and amplifiers. *Ieee Photonics Technology Letters* **2004,** 16, (9), 2024-2026.

2. Li, R. K.; Loock, H. P.; Oleschuk, R. D., Capillary Electrophoresis Absorption Detection Using Fiber-Loop Ringdown Spectroscopy. *Analytical Chemistry* **2006**.

3. Little, B. E.; Chu, S. T.; Absil, P. P.; Hryniewicz, J. V.; Johnson, F. G.; Seiferth, E.; Gill, D.; Van, V.; King, O.; Trakalo, M., Very high-order microring resonator filters for WDM applications. *Ieee Photonics Technology Letters* **2004,** 16, (10), 2263-2265.

4. Vahala, K. J., Optical microcavities. *Nature* **2003,** 424, (6950), 839-846.

5. Fraser, J. M.; Yam, S.; Loock, H. P.; Barnes, J.; Yastrubchak, O.; Chiu, O.; Oleschuk, R. D.; Wilson, M.; Qian, C. In *Biochemical Signal Detection in Miniaturized Fluidic Systems by Integrated Microresonator*, 28th IEEE EMBS Annual International Conference, New York City, New York, USA, Aug 30-Sept. 3, 2006; New York City, New York, USA, 2006; p WeD01.3.

6. Knight, J. C., Photonic crystal fibres. *Nature* **2003,** 424, (6950), 847-851.

7. Kong, G. J.; Kim, L.; Choi, H. Y.; Im, L. E.; Park, B. H.; Paek, U. C.; Lee, B. H., Lensed photonic crystal fiber obtained by use of an arc discharge. *Optics Letters* **2006,** 31, (7), 894-896.

8. Ritari, T.; Tuominen, J.; Ludvigsen, H.; Petersen, J. C.; Sorensen, T.; Hansen, T. P.; Simonsen, H. R., Gas sensing using air-guiding photonic bandgap fibers. *Optics Express* **2004,** 12, (17), 4080-4087.

9. Martelli, C.; Canning, J.; Groothoff, N.; Lyytikainen, K., Strain and temperature characterization of photonic crystal fiber Bragg gratings. *Optics Letters* **2005,** 30, (14), 1785-1787.

10. Jasapara, J.; Bise, R.; Windeler, R., Chromatic dispersion measurements in a photonic bandgap fibre. *OFC 2002* **2002**, 519-521.

11. Paldus, B. A.; Kachanov, A. A., An historical overview of cavity-enhanced methods. *Canadian Journal of Physics* **2005,** 83, (10), 975-999.

12. Muller, T.; Wiberg, K. B.; Vaccaro, P. H.; Cheeseman, J. R.; Frisch, M. J., Cavity ring-down polarimetry (CRDP): theoretical and experimental characterization. *Journal of the Optical Society of America B-Optical Physics* **2002,** 19, (1), 125-141.

13. von Lerber, T.; Ludvigsen, H.; Romann, A., Resonator based measurement technique for quantification of minute birefringence. *Optics Express* **2004,** 12, (7), 1363-1371.

14. Stewart, G.; Atherton, K.; Yu, H. B.; Culshaw, B., An investigation of an optical fibre amplifier loop for intra-cavity and ring-down cavity loss measurements. *Measurement Science & Technology* **2001,** 12, (7), 843-849.

15. Stewart, G.; Atherton, K.; Culshaw, B., Cavity-enhanced spectroscopy in fiber cavities. *Optics Letters* **2004,** 29, (5), 442-444.

16. Stewart, G.; Shields, P.; Culshaw, B., Development of fibre laser systems for ring-down and intracavity gas spectroscopy in the near-IR. *Measurement Science & Technology* **2004,** 15, (8), 1621-1628.

Chapter 10 Conclusion

Ringdown spectroscopy (RDS) in optical waveguides provides a means for performing absorption spectroscopy on very small liquid volumes. This opens avenues for using fibre cavity or fibre loop RDS as an absorption sensor for capillary electrophoresis, high performance liquid chromatography, or any other microfluidic application. Using optical fibre for this type of application has several advantages over mirror-based resonators: the optical mode diameter is matched to typical flow channel sizes; an interface can be constructed with relative ease, the light can be made to resonate in a single transverse mode simply by using a single mode fibre and using an appropriate sample interface configuration; long cavities can be used meaning requirements are eased for input pulse lengths and detection bandwidth; and optical fibre components are inexpensive and readily available.

We have presented a model which can describe multiexponential decay processes in optical cavities using the frequency dependent metrics of phase shift and modulation depth. This allows us to determine the ringdown time and steady-state intensity of each decay component. We applied this frequency domain (FD) measurement scheme to linear and circular waveguide resonators at telecom wavelengths (1520 – 1620 nm), in the near infrared (800 nm) and in the visible (405 nm). FD measurements are fast (time resolution 500 μs), easy to perform, and do not require much expensive equipment, however they are not without drawbacks. The two major ones are the inability to use

time-filtering to eliminate the effect of amplified spontaneous emission (ASE), and the difficulty in determining the frequency dependent phase offset in order to recover ringdown times. The former applies only to linear cavities, and the latter only to circular cavities.

In Chapter 4 we characterized a linear fibre Bragg grating (FBG) cavity. The FD data exhibited biexponential behaviour which we attributed to ASE outside the bandwidth of the FBGs. We recorded a ringdown time of 3.76 μs for resonant light at 1531.600 nm. After including a sample interface we recorded the absorption spectra of two simple amines to test the feasibility of biomolecule detection via the first N-H vibrational overtone. We determined a minimal detectable absorption loss of $\alpha_{min} = 360$ cm^{-1} for *m*-xylylenediamine in dimethylsulfoxide. The poor MDAL was ascribed to the instrument behaving as a single-pass absorption spectrometer due to the high relative intensity of ASE to resonant light in the wavelength range covered. A combination of side-pumping, spectral filtering using the FBGs, and index-matching at the fibre facets to reduce Fresnel reflections was shown to greatly reduce the ASE intensity reaching the detector. Biomolecule detection should be feasible using these measures.

To record broadband spectra (1520 – 1620 nm) of the same model amines we constructed a fibre-loop ringdown spectrometer. With this instrument we achieved an MDAL of $\alpha_{min} = 395$ cm^{-1} for *m*-xylylenediamine in dimethylsulfoxide at 1536 nm. This similar MDAL is thought to be poor because of cladding modes introduced at the sample gap and coupled out to the detector with high efficiency via the output coupler. Better

design of the sample gap and positioning of the output coupler far away from the interface should provide better results.

Next, the characterization of a fibre loop operating at 800 nm at ten modulation frequencies and ten dye concentrations was presented. The phase offset was obtained from a fit to the data. The corrected data however showed a trend quite unlike what was expected given the decay times determined in the time domain. We hypothesized that this discrepancy was due to interference from the diode laser present in the cavity output signal used to determine the phase angle. Despite this problem, an MDAL of $\alpha_{min} = 0.28$ cm^{-1} could be estimated for the dye ADS805WS, which is an improvement by a factor of ~ 10 over previous results. This gain lies entirely in the choice of modulation frequency.

The preliminary results for a fibre loop sensor for unlabeled detection of biomolecules at 405 nm were promising. An MDAL of $\alpha_{min} = 16$ cm^{-1} for myoglobin in water was achieved. With further optimization of the apparatus and a better choice of modulation frequency, an improvement in performance should be realized.

A novel optical microphone was used to show that the time resolution of a phase angle measurement can be at least 500 μs, and was limited from attaining better resolution by the sampling rate of the lock-in amplifier. We also performed a preliminary test of a Fourier transform method that promises parallel acquisition of the phase angle, modulation depth, and the phase offset at many modulation frequencies. Using an RC circuit as a model system, it was shown that recovery of the impulse response function from a chirped sine wave input is possible, and the characteristic time was very similar to

that obtained in the time domain. With the appropriate equipment, parallel acquisition could be easily applied to optical fibre cavities.

A number of methods to reduce optical loss in the waveguide resonators used were investigated in Chapter 3. The first looked to reduce the optical loss associated with input and output couplers. A grating-assisted coupler (GAC) utilizing two long period gratings (LPGs) provided a variable fibre-fibre coupling ratio of 0 to 0.64 % with an insertion loss of 13 dB. However a GAC is limited to the wavelength range of the rejection band of the LPGs. Next a broadband cladding mode injection (CMI) coupler was investigated. This coupler design also features variable coupling (0 to 0.05 %) with an insertion loss of < 0.0005 %. The CMI design depends on cladding modes for transfer of power between fibres, the presence of which leads to more complicated analysis of FD data. Neither the GAC nor the CMI coupler was deemed an appropriate replacement for the expensive but suitable field access block coupler. The second method looked to reduce the optical loss that occurs at the sample interface due to the divergent beam exiting the fibre facet. Microlenses were created from flat-cleaved facet of the fibre by melting in an electrical arc. Fabricating lenses on both fibre facets generated a convergent beam exiting the fibre (into air) and assisted in coupling into the receiving fibre. Transmission efficiency of 0.98 and 0.97 was achieved for lenses created from single mode and multimode fibre at 4 and 65 μm separation, respectively. The lenses are easily made, provide a large reduction in optical loss, and should be included in the apparatus whenever possible.

There are many promising directions for future research on optical waveguide-based ringdown spectrometers to take. The obvious first step to take would be to optimize the experiments presented here to obtain better performance. Unlabeled biomolecule and single cell detection have already been shown to be feasible. Miniaturizing the optical resonator to reduce material loss opens up the possibility to work at wavelengths from the UV to the IR. Exciting a whispering gallery mode in a hollow core waveguide perpendicular to liquid flow inside the core may be the easiest miniature resonator with a sample interface to implement. Photonic crystal fibre (PCF) offers a number of advantages over conventional fibre such as a large mode field diameter and endlessly single mode operation. It is also possible to introduce a gas or liquid sample into the voids in the PCF to create a trace detector similar to a conventional mirrored ringdown cavity but with a much smaller sample volume. The sensitivity of FD-FLRDS might be improved by utilizing two loops in series to increase the range of possible phase angles from 0 to -90^{o} to 0 to -180^{o}. Another avenue is to take advantage of the etalon-like behaviour of a ringdown cavity and work at a modulation frequency that is at a resonance in the longitudinal mode spectrum of the cavity. FCRDS can be adapted to measure the circular birefringence (CB) of the cavity medium. This implies it should be possible to measure the CB of a liquid introduced in the cavity and may make possible the determination of enantiomeric excess. Finally, the intracavity intensity can be increased by introducing a gain medium into the cavity, which should lead to a lower detection limit and better sensitivity.

In conclusion, we have shown that analysis of multiexponential decay processes in the frequency domain is possible. We successfully applied this to linear and circular resonators at various wavelengths and in different fibre types. We also suggested ways to reduce data acquisition time and to reduce optical loss. It is fair to say that we can expect many interesting future developments in the field of ringdown spectroscopy in optical waveguides. Many of these developments will likely be driven by the desire the perform absorption spectroscopy on minute liquid volumes in a variety of contexts. Improvements in laser and waveguide technology should assist in opening this field to ever broader application.